Ultracold Polar KRb Molecules in Optical Lattices

by

Brian Neyenhuis

B.S., Brigham Young University, 2006

A thesis submitted to the

Faculty of the Graduate School of the

University of Colorado in partial fulfillment

of the requirements for the degree of

Doctor of Philosophy

Department of Physics

2012

This thesis entitled:
Ultracold Polar KRb Molecules in Optical Lattices
written by Brian Neyenhuis
has been approved for the Department of Physics

Deborah Jin

Prof. Jun Ye

Date

The final copy of this thesis has been examined by the signatories, and we find that both the content and the form meet acceptable presentation standards of scholarly work in the above mentioned discipline.

Neyenhuis, Brian (Ph.D., Physics)

Ultracold Polar KRb Molecules in Optical Lattices

Thesis directed by Prof. Deborah Jin

The creation of a gas of ultracold polar molecules with a high phase space density brings new possibilities beyond experiments with ultracold atomic gases. In particular, long-range, anisotropic, and tunable dipole-dipole interactions open the way for novel quantum gases, with applications including strongly correlated many-body systems, and ultracold chemistry. This thesis will present the final steps to complete control over both internal and external degrees of freedom of the molecule which allows us to control, and even completely suppress, the chemical reactions between molecules. First, the control over internal states has been achieved through coherent state transfer to the ro-vibronic ground state and coherent manipulations of the hyperfine and rotational states with microwave radiation. Second, external degrees of freedom are controlled by loading the gas into an optical lattice. With the molecules loaded into a one-dimensional lattice, the orientation of the molecular collisions is controlled by manipulating both internal (hyperfine states) and external (motional states in the direction of tight confinement) degrees of freedom. Most striking is that by preparing the molecules all in the lowest band of the lattice in the same internal state, the molecular collisions can only occur in a "side-by-side" orientation, where the chemical reaction rate is suppressed by the repulsive dipole-dipole interactions. The chemical reaction can be suppressed completely by further constraining the motion in the trap in a strong 3D lattice. Here we see lifetimes longer than 20 s, limited by off-resonant light scattering. Finally, the ac polarizability of the molecules is explored and controlled. The different rotational states of the molecule have different polarizabilities and will experience a different trapping force in both the optical dipole trap or lattice. We show that there is a "magic angle" between the quantization axis and the polarization of the trapping laser at which the polarizabilities of two different rotational states can be matched, eliminating dephasing and allowing for coherent manipulations between rotational

states.

Dedication

To my family. I started this adventure with my wife Marisa and we are finishing it with three beautiful children: Cameron, Liesel, and Ivy. Thank you for all your understanding and support.

Acknowledgements

One of the many fantastic things about working at JILA is that you get to associate with a lot of great people. I used to tell people that we had a small army working on the KRb project, and now that I look back on the list of all the people on the project, I realize that this is not too far from the truth. I had the great pleasure of working with (listing only the experimentalists who worked directly on KRb) Josh Zirbel, Kang-Kuen Ni, Silke Ospelkaus, Avi Pe'er, Dajun Wang, Marcio de Miranda, Amodsen Chotia, Steven Moses, Bo Yan, and Jacob Covey.

An experiment as complicated as the KRb machine wasn't built in the space of a single graduate career. Josh and Kang-Kuen started the KRb project in an empty lab and by the time Josh graduated they had created ultracold Feshbach molecules. We were able to continue to build onto an already complex experiment because of Josh's attention to detail in designing the experiment. Even though Josh was close to graduation when I joined the experiment, he took the time to patiently explain the experiment to me. Avi also had a gift for explaining complex ideas in a very simple way and was never too busy to stop and answer my questions or listen to my dumb ideas. I learned a lot from working with Kang-Kuen and Silke. They showed me the ropes and then taught me how to diagnose problems, troubleshoot the experiment, and made me dive into every subsystem of the experiment in great detail. They expected a lot from me when I was a young graduate student, and as a result I learned a lot.

There was about six months when we had enough man power that we ran the experiment in shifts. Dajun and I ran the early shift, and then handed the experiment off to Silke, Kang-Kuen and Marcio in the afternoon. Dajun is one of the hardest working people I have ever met and I learned

a great deal from him as we worked together on the direct imaging of KRb. Marcio taught me the mystical ways of the octave spanning frequency comb. We were the two graduate students who "inherited" the experiment after Silke and Kang-Kuen left, and together with Dajun and Amodsen we were able to bring the experiment beyond just creating and observing ground state molecules, and onto manipulating them. On one of the papers we published together there is a star next to each one of our names denoting that we "contributed equally." That is an accurate description of all the work that went on in the lab at that time. We all worked together and contributed equally on all parts of the experiment and were able to see fantastic results. Working with Amodsen, Marcio, and Dajun was a real pleasure. They put up with my odd sense of humor and made working in the lab very enjoyable.

Now the experiment is being passed on to Steven, Jake, and Bo and I see a very bright future. They are about to move the experiment into a new lab and make some major changes to the apparatus, and having worked with them for the last few years, I have complete confidence in their ability to succeed. I can't imagine what it would be like to work on an experiment all by myself and I feel very privileged to have worked with such great people.

In addition to those who worked directly on the experiment with me I had a lot of help from theorists. Among them John Bohn and Goulven Quéméner stand out and warrant special mention. John and Goulven have helped guide the KRb experiment theoretically for the majority of my graduate school career. Goulven has always been willing to take time out of his day to answer my questions and explain the finer points of scattering theory. I have also had the great pleasure of working with Michael Foss-Feig, Kaden Hazzard, Salvatore Manmana, Jose D'Incao, Chris Greene, Paul Julienne, and Svetlana Kotochigova. Their theoretical guidance allowed us to always be moving forward.

I would like to acknowledge all the members of the bi-group especially Eric Cornell. Our weekly meetings showed me a much broader view of atomic physics and provided great advice. Jun's group also provided countless solutions to technical problems. I of course need to thank the JILA staff in both the electronics and instrument shop as well as Krista Beck. I am also grateful

to my running partner Ryan Thalmann for getting me up at 6am every weekday to run and talk physics, chemistry, and politics.

Lastly, I need to acknowledge Debbie and Jun. I could not have asked for better advisors. I was not technically Jun's student, it was Debbie who hired me my first year before the project had fully merged into a joint venture. But he always took time to guide me and teach me. Jun's expertise in precision measurement has helped me learn how to do things right (as opposed to my normal mode of operation which is "do it fast"), and more importantly taught me how to know when it matters. I was always impressed that after all the amazing discoveries that Jun has been apart of he would still get so excited about about our progress both big and small. He is always driving the experiment along, thinking about the next steps and pushing forward.

I have never met anyone with as much physical intuition for cold atom gasses as Debbie has, and I hope some of that has rubbed off on me. Debbie takes great pleasure in solving problems. It doesn't seem to matter how big or small they are, and she isn't afraid to dive in and get right into the details. She has a gift for looking past all the noise and getting right to the very essence of a problem. I have learned to trust and appreciate her advice and I consider her a true friend.

Contents

Chapter

Tables

Table

Figures

Figure

Chapter 1

Introduction

1.1 Why should I care about polar molecules at all, let alone this thesis?

In August 2006 when I arrived at the University of Colorado, the quest for ultracold polar molecules was already well on its way. I walked onto a working experiment that had been built with the express purpose of creating and studying ultracold polar $^{40}K^{87}Rb$ molecules. In many senses, ultracold polar molecules are a natural extension of work done with ultracold atomic gas systems, which have been a real workhorse in atomic physics. I will define ultracold (as opposed to just cold) as being sufficiently cold such that atoms interact via a single partial wave. The actual energy scale or temperature at which this ultracold regime starts depends upon the atom or molecule of choice, but is usually in the range of a few microKelvin [6]. (I should point out here that this definition falls apart for polar molecules because the dipole-dipole interaction mixes partial waves together, but this is a subtlety best left for later in this thesis.) Here in the ultracold regime, atom gases become incredibly versatile and controllable quantum laboratories with diverse applications including quantum information, atomic clocks, precision tests of fundamental physics, and quantum simulation. The high degree of control over both internal (hyperfine, rotation, and electronic states) as well as external (motion in the trap) states makes them ideal for studying quantum many-body phenomena. Ultracold polar molecules build on the success of ultracold atoms but with two important additions: they have a richer internal structure and, perhaps most importantly, they have long-range interactions.

Atoms in an ultracold gas (with the notable exception of a few atoms with large magnetic

dipole moments) have short-range interactions. They act much like billiard balls in that they only interact when they come in direct contact with each other. This contact interaction can be written with a Dirac delta function. Even near a Fano-Feshbach resonance where the strength of these interactions can be tuned arbitrarily large, it is only the prefactor that sits in front of the delta function that changes, and one still has short-range, contact interactions. Molecules, on the other hand, have long-range, anisotropic interactions arising from the dipole-dipole interaction. In the case of two identical electric dipoles aligned to an external electric field, the dipole-dipole interaction is $\frac{d^2}{4\pi\epsilon_0 r^3}(1-3\cos^2(\theta))$ where d is the dipole moment, ϵ_0 is the electric permittivity of free space, r is the distance between dipoles, and θ is the angle between the external electric field and the line between the two molecules. The anisotropy that comes from the $1-3\cos^2(\theta)$, which means that two dipoles lined up "head-to-tail" attract, while two dipoles lined up "side-by-side" repel each other. This anisotropy can be a nuisance as it ruins the symmetry of our system, but I will show later that we can escape the anisotropy by moving to an optical lattice that confines the gas to two dimensions, and even exploit the anisotropy of the dipole-dipole interaction to explore quantum stereodynamics of ultracold chemical reactions.

The $1/r^3$ dependence gives rise to an interaction that is long range for sufficiently large dipole moments. When talking about the range, it is convenient to define the dipole length, which is the distance at which the dipole-dipole interaction becomes stronger than the van der Waals interaction. The dipole length is defined as $d_l = \frac{d^2\mu}{4\pi\hbar^2\epsilon_0}$ where μ is the reduced mass of the two molecules and $\hbar$ is Planck's constant divided by 2π. The dipole length of KRb when it is fully polarized ($d = 0.566$ D) is 5740 a_0 (where $a_0 = 5.29\times10^{-10}$ m is the Bohr radius). Due to experimental constraints on the maximum electric field we can apply, the dipole length of KRb in an experiment ($d = 0.2$ D) is currently limited to 720 a_0. For comparison, a much more polar molecule such as OH ($d = 4$ D) has a dipole length of 4×10^4 a_0, and LiCs (the most polar of the bialkali molecules with $d = 5.2$ D) has a dipole length of 5.4×10^5 a_0. I should also mention that there are several atoms with large magnetic dipole moments that have been cooled to the ultracold regime: among them are Cr, Dy, and Er with magnetic moments of 6, 10, and 8 Bohr magnetons, respectively, which corresponds

to dipole lengths of 23, 195, and 130 a_0.

For a gas of ultracold polar molecules, these dipole lengths are already on the order of the interparticle spacing, which opens the possibility of strongly correlated many-body systems. In the limit that the dipole length becomes much larger than the interparticle spacing, the molecules can self assemble into a crystal [7]. The dipole length is also on the same order as the spacing between lattice sites in a 1064 lattice (1000 a_0), which allows us to build on the success of cold atom systems in realizing Bose and Fermi Hubbard Hamiltonians, but now with the ability to have nearest neighbor and next-nearest neighbor interactions. This opens the possibility of realizing many interesting spin systems where massive entanglement can occur and quantum magnetism can be explored.

Although perhaps not quite as exciting as strong long-range interactions, the extra complexity of a molecule is certainly a feature worth mentioning. The rotation states of the molecule are quite useful because of their long lifetime and convenient transitions in the microwave. The long lifetime allows transitions between rotation levels to be used as a sensitive spectral probe, allowing us to measure small energy shifts with great accuracy. This could be used to measure small energy shifts resulting from interactions. It has also been proposed that polar molecules can be used for precision measurements of fundamental constants, including the permanent electron electric dipole moment [8], time variation of the fine-structure constant [9], and the electron-to-proton mass ratio [10]. We could use microwaves to couple the ground and rotationally excited states to tailor the adiabatic collision potential and potentially even prevent short-range collisions altogether [11].

I should mention that although I have grown quite fond of KRb over the last six years, the specific molecule is not too important at this point in the story. K and Rb were used simply because they were convenient to cool down to quantum degeneracy. Although the details of KRb and our choice of isotopes will play a very important role later in this thesis when I discuss ultracold chemistry, the two main driving reasons to create ultracold polar molecules (long-range interactions and complex internal structure) are general to any heteronuclear molecule.

At this point I could say something about how we could use polar molecules to simulate

complex condensed matter systems such as high-temperature super conductivity in cuprates [12]. I could say that although these systems don't necessarily interact through dipole-dipole interactions, the physics of strongly correlated systems with long-range interactions should have some general features that our highly controllable and tunable polar molecule system should be able to explore, and perhaps shed light on how to understand these even more complicated condensed matter systems. But to be perfectly honest, although I've certainly used these arguments before, they don't really resonate with me. I think that a strongly interacting gas of polar molecules in the quantum regime with tunable long-range interactions is interesting all by itself. In the right situations, or with the proper manipulation, these systems may indeed have a Hamiltonian that looks a lot like one of your favorite quantum magnetism spin models [13], or a Hubbard Hamiltonian that might support anyonic excitations [14]. But studying strongly correlated many-body systems is interesting simply because, despite the fact that we can control these systems with amazing precision, we still don't have a good way of predicting what should happen in the limit of a strongly interacting many-body system. They are both amazingly simple (just a handful of interacting dipoles, how hard could that be? I can write down that Hamiltonian, no problem.) and complex all at the same time. We are taking the power of cold atom gas physics and adding long-range interactions and the novel quantum gasses that arise are fascinating.

1.2 So what did you do that is such a big deal?

In this section, I provide a brief overview of the JILA KRb work that I contributed to, and describe the focus of this thesis. I was fortunate to start graduate school right as things in the JILA KRb experiment were getting really interesting. When I arrived at JILA, Feshbach molecules had just been created, but had not yet been studied. A difficulty in the experiment was a short lifetime of the Feshbach molecules because our multi-mode optical dipole trap laser happened to be on resonance with a molecular bound-bound transition and was driving the Feshbach molecules into an electrically excited state within a few microseconds of their creation. It took quite a bit of time to figure out this problem, and before we did, we were very worried that the molecules

were too collisionally unstable to be studied, let alone transferred to the absolute ground state of the molecular potential. At this time, we were also joined by Silke Ospelkaus who, in her Ph.D. work, had studied KRb Feshbach molecules in an optical lattice [15]. They did not see the same loss, because they managed to avoid the bound-bound transition that our laser was driving, but, in any case, an optical lattice also shields the molecules from collisions. Although a quick calculation of density and collision rate should have convinced us that the problem was unlikely caused by collisions, we were still worried, and for this reason, my first project in the lab was to get a laser for an optical lattice and investigate how we should go about implementing it. This laser was used to replace our multi-mode laser for the optical trap instead and an optical lattice was not implemented in our experiment for another three years, but it did end up being the main focus of my Ph.D. work when I became the senior graduate student and finally got "the keys to the car".

After a brief detour to study the collisional properties of KRb Feshbach molecules, the lab turned its attention to the main goal of creating ground-state molecules. Surprisingly, there was quite a bit of information already known about the KRb molecular potential [16] and with the theoretical guidance of Svetlana Kotochigova and Paul Julienne, we were able to pin down the location of the relevant states for transferring the molecules to deeper bound states. There was quite a bit of feedback back and forth from theory to experiment, and every state we measured helped pin down the molecular potential and the predictions got better and better. Because of this feedback process, our understanding of the molecular potential came gradually and our path to the absolute ground state took several steps. First, to show that a coherent transfer via STIRAP (STimulated Raman Adiabatic Passage) [17] was possible, we transferred our Feshbach molecules to a molecular state in the singlet potential bound by 10GHz [18]. We then transferred Feshbach molecules to the lowest energy state of the ground triplet potential ($^3\Sigma$). And then in 2008, we finally transferred our molecules to the absolute ro-vibronic ground state (in the singlet potential) [19]. With the molecules in the ground state, we applied an electric field to demonstrate the polar nature of the molecules by measuring the Stark shift. We found that with with electric plates outside of the vacuum chamber, we could only partially polarize our molecules to an effective

dipole moment in the lab frame of 0.2 Debye. We also mapped out the hyperfine structure of the ro-vibronic ground state and demonstrated the ability to transfer our molecules to any desired hyperfine state [20].

With complete control over the internal state of the molecule, we turned our attention to the collisional properties of the ground-state molecules, and studied both atom-molecule and molecule-molecule collisions. We observed density-dependent loss for for K + KRb, which we attribute to chemical reactions. We also observed density-dependent loss for Rb + KRb when either Rb or KRb was in an excited hyperfine state, which we attribute to hyperfine-state-changing collisions [1]. Most importantly for the work that will be discussed in this thesis, we found evidence of chemical reactions between two KRb molecules at ultralow temperatures. This is both a feature and a challenge. Energetically, the bimolecular atom-exchange reaction KRb + KRb $\rightarrow$ K_2 + Rb_2 is exothermic. Moreover, as is generally true for chemical reactions between alkali atoms [21], this chemical reaction has no potential barrier and therefore requires no activation energy.

However, even without a chemical reaction barrier, for ultracold, spin-polarized, fermionic molecules, such as KRb, there is a centrifugal p-wave barrier that appears due to the requirement that the wavefunction of two indistinguishable fermions be antisymmetric with respect to exchange of the particles. With only a centrifugal barrier to prevent the molecules from chemically reacting, the chemical reaction rate is set by the rate at which molecules tunnel through the p-wave barrier. Once inside the p-wave barrier, the molecules chemically react with near unit probability. We verified this simple model by varying the temperature and observe that the chemical reaction rate scales linear with temperature as predicted by the Wigner threshold laws [22].

Although the p-wave barrier is spatially symmetric, the dipole-dipole interaction is not, and so turning on an external electric field to polarize the molecules results in anisotropic collisions, which drastically change the chemical reaction rate. In simple terms, two dipoles colliding "side-by-side" have a repulsive interaction so the p-wave barrier is enhanced and the chemical reactions are suppressed, but two dipoles colliding "head-to-tail" have an attractive interaction that decreases the p-wave barrier and enhances the chemical reaction loss rate. In a three-dimensional optical

dipole trap, both processes will occur and the chemical reaction rate is determined by the faster of the two rates. As a result, we see a dramatic increase in the chemical reaction rate as an external electric field is applied to polarize the molecules [1].

We decided to exploit the spatial anisotropy of the dipole-dipole interaction to create a collisionally stable gas in 2D. We can turn off the "head-to-tail" collisions by loading the molecules into a one-dimensional optical lattice. In this two-dimensional trap geometry, we demonstrate that with an electric field applied along the lattice beam direction, "head-to-tail" collisions can be suppressed and strong dipolar interactions and collisional stability can be enjoyed simultaneously. Even further suppression of the chemical reactions was achieved by loading the gas into a three-dimensional optical lattice. In the limit of a deep lattice where the tunneling was suppressed and the molecules never touched, we found that the molecules essentially didn't chemically react at all [3].

Although I have been fortunate enough to be involved in the spectroscopy, transfer to both the triplet and singlet ground state, as well as all the studies on the ground state molecules, the experiments focused on controlling the molecules' internal degrees of freedom (electronic, vibration, rotation, and hyperfine) are already described well in the thesis of Kang-Kuen Ni [23], and I will not focus on them in this thesis. Instead, this thesis will focus on the studies done to control the molecules' external degrees of freedom (motion in the trap). This includes our studies of the polarizability, progress towards evaporation, and the work done in an optical lattice, where I will discuss the role reduced dimensionality plays in controlling the molecular interactions. But to paint a complete picture of the physics involved I will necessarily include some overlap with the information in the theses of Kang-Kuen Ni [23] and Marcio de Miranda [24].

1.3 Outline of this thesis

Chapter 2 will introduce the optical lattice. I will give an overview of optical lattices, relevant to the discussion of our experiments in subsequent chapters. I will introduce the band structure and corresponding Bloch wavefunctions, which are useful in describing weak lattices, as well as

the Wannier functions which describe deep lattices. The second half Chapter 2 will be focused on describing the experimental techniques we use to load, probe, and characterize the lattice. In Chapter 3 I will present a brief overview of our experimental observations regarding the chemical reactions between two KRb molecules. I will show that the chemical reaction rates are strongly influenced by the dipole-dipole interactions. Chapter 4 will present the exploration of quantum stereodynamics in a one-dimensional lattice. I will show how we can control the chemical reaction rate between KRb molecules by controlling both the internal and external quantum states of the molecules in a 1D lattice. Chapter 5 will present our studies of both the ground-state molecules and the Feshbach molecules in a 3D lattice. In Chapter 6 I will present our measurements of the ac polarizability and discuss its effects on the coherence between different rotational states of the molecule. Finally, Chapter 7 will give conclusions and outlook.

The work described in this thesis has been published in several papers [18, 19, 25, 2, 1, 20, 3, 4, 26]. In particular, Chapter 3 closely follows Ref. [1] and [2], Chapter 4 closely follows Ref. [3], Chapter 5 follows Ref. [4], and Chapter 6 follows Ref. [5].

Chapter 2

Optical Lattice

Optical lattices have been an incredibly useful tool in atomic physics both because they allow for very precise control over the trapping potential, and they provide a periodic potential similar to those found in crystalline condensed matter systems [27]. But unlike the periodic potentials in a crystal, the potentials in an optical lattice are almost entirely defect free. Moreover, the strength of the lattice (a parameter which cannot be tuned continuously in a solid state crystal) can be easily adjusted in real time by controlling the intensity of the lattice. This control gives the ability to change the tunneling rate in the lattice.

In 1998 it was pointed out by D. Jaksch and coworkers that ultracold atoms loaded into an optical lattice could realize the Bose-Hubbard Hamiltonian [28]. This proposal was realized by M. Greiner and coworkers in 2002 with the observation of the superfluid to Mott-Insulator quantum phase transition in a BEC loaded into an optical lattice [29]. Since this initial observation, there have been many exciting experiments both with bosonic and fermionic atoms in an optical lattice (for a review see [30]). Additionally the ability to independently control the scattering length with Feshbach resonances adds the ability to control the onsite interaction, including changing from attractive to repulsive interactions [31, 32, 33].

Although the ability to simulate condensed matter physics in a lattice is extremely interesting, especially with the addition of the long-range interactions between polar molecules, for most of the experiments discussed in this thesis the optical lattice is just a well controlled potential with tight confinement. We can combine multiple lattices in orthogonal directions to change the dimensionality

of the system. A single lattice beam (a 1D lattice) gives an array of two-dimensional pancake shaped traps. Two lattice beams (a 2D lattice) provides an array of 1D tubes. Three lattice beams (a 3D lattice) gives an array of 0D, point-like traps. We exploit these geometries to control the stereodynamics of chemical reactions in 2D [3], or to suppress them entirely in a 3D lattice by holding each molecule in its own trap, unable to chemically react with molecules in adjacent sites [4].

To obtain these reduced geometries we need to load all the molecules into a single band, which requires that the spacing between energy levels in the direction of tight confinement be much larger than the energy of the gas. This requires tight confinement and cold temperatures. The steep potential gradients in an optical lattice allows these criteria to be met with reasonable experimental parameters. To give an illustration, if we focused a 1064 nm laser down to a beam waist of 5 μm (a small but reasonable beam waist) by 250 μm (to match our lattice geometry) it would take 1.7 kW to get a trapping frequency equivalent to our lattice with 1 W of power.

In this chapter I will give a quick theoretical background to understand the origin of the lattice potential, and how molecules interact with it. This will introduce the band structure and corresponding Bloch wavefunctions, which are useful in describing weak lattices, as well as the Wannier functions that describe deep lattices. The second half of this chapter will be focused on the experimental techniques we use to load, probe, and characterize the lattice.

2.1 Optical dipole force

Atoms or molecules in a laser field will experience a shift in energy due to the AC stark shift. Here the oscillating electric field of the laser light induces an AC electric dipole moment in the atom or molecule. Just as with a classical oscillator, if the laser light drives the atom or molecule at a frequency below its resonance frequency (the laser is red-detuned) the atom/molecule will respond in phase, such that the dipole is always aligned opposite of the oscillating electric field and will be attracted to the most intense part of the laser beam. Conversely, if the laser field drives the atom/molecule at a frequency higher than its resonance frequency (a blue-detuned laser), the

atom/molecule responds out of phase and will be repelled from the most intense part of the laser beam.

For atoms, the potential from a far detuned optical trap is easy to derive and can be calculated quite accurately using only the closest atomic resonances [34]. For molecules, the large number of energy states, and the lack of closed cycling transitions makes calculating the potential more difficult [35]. But all the interactions with all the excited states can be included into a single parameter, the polarizability, which is defined by:

$$U(\omega, \vec{r}) = \alpha(\omega) I(\vec{r}), \tag{2.1}$$

where $\omega = \frac{2\pi c}{\lambda}$ is the frequency of the light, c is the speed of light, λ is the wavelength of the light, $U(\omega, \vec{r})$ is the potential energy, $I(\vec{r})$ is the spatially dependent intensity of the laser, and $\alpha(\omega)$ is the frequency dependent polarizability. Although $\alpha(\omega)$ can be quite complicated, in practice we only care about the polarizability at the frequency of our optical trap. To avoid off-resonant light scattering we use an optical trap at $\lambda = 1064$ nm, which for the absolute ground state of KRb is detuned by more than 30 nm from the lowest excited state potential.

2.2 Optical lattice

In our experiment we form our optical lattice with a single retro-reflected gaussian laser beam. The interference between the incoming and retroreflected laser beams forms a standing wave with a periodicity of $\lambda/2$. The optical potential is given by:

$$U(r, z) = -\alpha 4 I_0 \exp\left(\frac{-2r^2}{w^2(z)}\right) \cos^2(kz) \tag{2.2}$$

where $I_0 = \frac{2P}{\pi w^2(z)}$, P is the laser power of the incoming beam, $w(z) = w_0\sqrt{1 + (z/z_R)^2}$ is the beam waist at z, w_0 is the beam waist at the focus, $z_R = \pi w_0^2/\lambda$ is the Rayleigh length, and $k = 2\pi/\lambda$ is the wave number. Notice that the potential at $z = r = 0$ has a depth four times that of a single dipole beam with the same intensity I_0 ($U = \alpha I_0$) due to the constructive interference of the two beams.

Although the sinusoidal shape of the lattice potential is important to understand the motion of particles as they move from site to site in the lattice, for deep lattices it is often useful to think of an optical lattice as an array of traps each approximated with a harmonic potential. Here we can define trapping frequencies

$$\omega_r = \sqrt{\frac{1}{m}\left(-\frac{\partial^2 U(r,z)}{\partial r^2}\right)_{r=z=0}} = \sqrt{\frac{16\alpha I_0}{m w_0^2}}, \tag{2.3}$$

$$\omega_z = \sqrt{\frac{1}{m}\left(-\frac{\partial^2 U(r,z)}{\partial z^2}\right)_{r=z=0}} = \sqrt{\frac{8\alpha I_0 k^2}{m}}. \tag{2.4}$$

These equations are only valid at the center of the lattice beam. At the edges of gaussian profile of the lattice beam, the intensity will be lower, resulting in a lower trapping frequency. In our experiment, the beams are large ($w_0 = 250$ μm) compared to the average cloud size (30 μm) so this inhomogeneity can generally be ignored.

Higher dimensional lattices can be obtained by adding additional laser beams. Although there are many different possible ways to arrange the lasers resulting in many different lattice geometries [36], in the experiments described in this thesis we have up to three orthogonal retroreflected laser beams resulting in a square lattice geometry. To avoid interference between orthogonal beams the frequency of each beam is shifted by tens of MHz relative to the other beams. The interference between beams has a resultant potential that moves at tens of MHz, which is fast enough that the molecules only see the time-averaged potential.

2.3 Band structure

The solutions to a particle moving through a periodic potential were introduced by Felix Bloch in the 1920s to describe the motion of electrons in crystalline solids [37]. For clarity we will look at these solutions in the simplest case of a particle moving in one dimension through a homogeneous potential given by $V = V_0 \cos^2(kx)$. Although we will restrict ourselves to 1D, the potential for a three-dimensional square lattice is completely separable and can be treated in the same way with no additional complications. The motion of the particles in a lattice potential is

given by Schrodinger's equation in one dimension:

$$\left(-\frac{\hbar^2}{2m}\frac{\partial^2}{\partial x} + V_0\cos^2(kx)\right)\Psi(x) = E\Psi(x). \tag{2.5}$$

$\Psi(x)$ is the Bloch wavefunction, which must follow Bloch's theorem:

$$\Psi(x+\lambda/2) = \exp\left(\frac{iq\lambda}{2\hbar}\right)\Psi(x). \tag{2.6}$$

Here we introduce the quasimomentum q, which gives the phase difference between adjacent lattice sites. To satisfy Bloch's theorem, $\Psi(x)$ is given by the product of a plane wave with quasimomentum q multiplied by a function with the same periodicity as the potential:

$$\Psi_{n,q}(x) = \exp\left(iqx/\hbar\right)u_{n,q}(x), \tag{2.7}$$

where $u_{n,q}(x)$ is the periodic envelope function. Because of the periodicity of $u_{n,q}(x)$, the Bloch wavefunction is delocalized over the entire lattice. The quasimomentum, q, is only unique up to the reciprocal lattice vector, so we restrict ourselves to the first Brillouin zone and work with $-\hbar k < q < \hbar k$. For each value of q there is an infinite set of eigenstates, which we label with a band index n. The solutions to equation 2.5 are well known and are easily obtained in Mathematica with the "MathieuC" and "MathieuCharacteristicA" functions. In figure 2.1 we show the band structure for increasing lattice depth, where the lattice depth is given in units of $E_{\text{rec}} = \frac{\hbar^2k^2}{2m}$. With no lattice the band structure is just the energy for a free particle mapped onto the first Brillouin zone. As the lattice depth increases the bands separate and become flatter. For deep lattices the spacing between bands approaches $\hbar\omega$, where ω is the trap frequency of a single lattice site given in equation 2.4.

Although the delocalized Bloch wavefunctions are the eigenstates of the lattice potential for all lattice depths, in the limit of deep lattices, tunneling is strongly suppressed and atoms/molecules are effectively localized on the timescales of the experiments. Here it is useful to switch to a localized basis set given by the Wannier functions [38], which are defined through the following Fourier transform:

$$w_n(x-x_i) = \frac{1}{\sqrt{M}}\sum_q \exp\left(-iqx_i\right)\Psi_{n,q}(x), \tag{2.8}$$

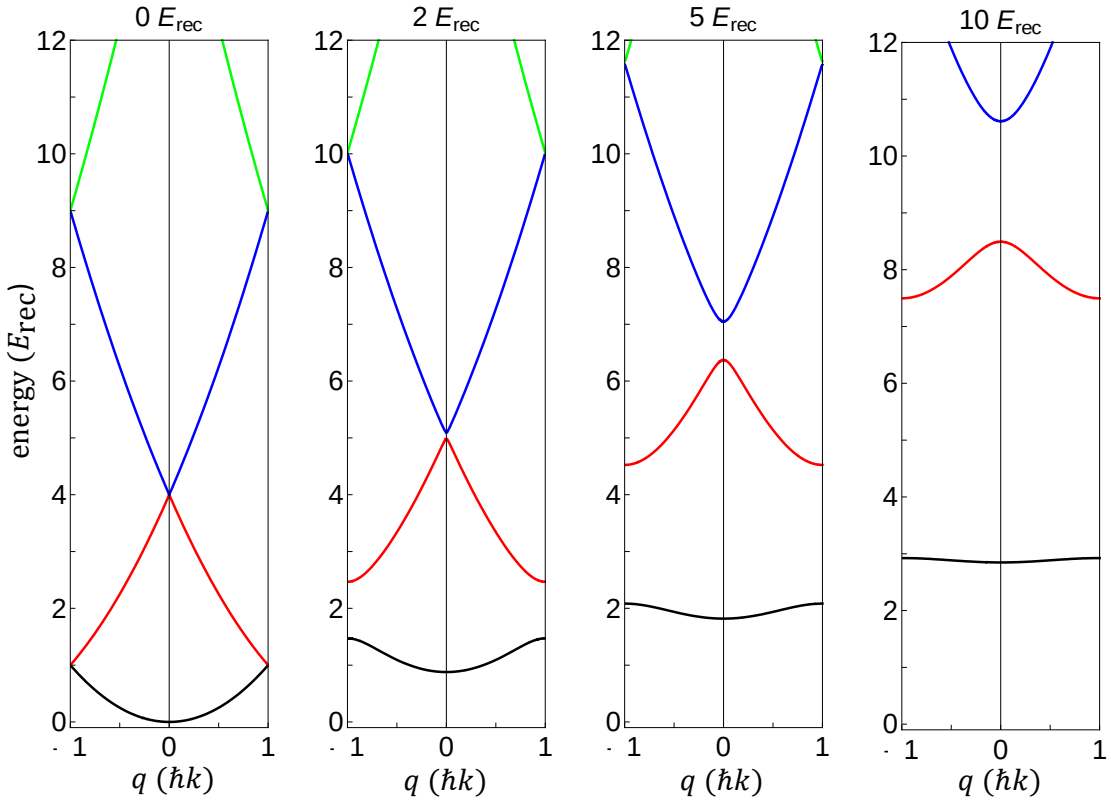

Figure 2.1: Band structure of an optical lattice. Energy of the different bands in the lattice is plotted vs. quasimomentum q for 0, 2, 5, and 10 E_{rec}. Only the first Brillouin zone is shown.

where M is the total number of lattice sites, and the sum is over all quasimomentum in the first Brillouin zone. The Wannier functions and the corresponding probability density are shown in figure 2.2 for 2 E_{rec} (top panels) and 10 E_{rec} (bottom panels). For 2 E_{rec}, the wavefunction has a large oscillation in the tail extending into the adjacent lattice sites, and as a result overlaps well with the Wannier functions on adjacent lattice sites. For 10 E_{rec}, the oscillations in the tail is just barely visible and the wavefunction overlap between adjacent sites is much smaller.

We can use these localized Wannier functions to look at the probability for an atom/molecule to hop from one site to an adjacent site. We calculate the tunneling matrix element, J, by finding the wavefunction overlap with:

$$J = \int w_1(x - x_i) \left(-\frac{\hbar}{2m} \frac{\partial^2}{\partial x^2} + V_0 \cos^2(kx) \right) w_1(x - x_j) dx, \tag{2.9}$$

which relates directly to the band width of the first band [39]:

$$J = \frac{E_{q=0,n=0} - E_{q=\hbar k,n=0}}{4}. \tag{2.10}$$

J has units of energy and is related to the tunneling time, $t = \hbar/J$

In the limit of deep lattices, the Wannier function for the ground band can be approximated with a gaussian. This seems perfectly reasonable because the deep lattice potential is well approximated by a harmonic potential (and the ground state wavefunction of the harmonic oscillator is a gaussian). A gaussian wavefunction is often used when looking at the momentum distribution, or when calculating the onsite interaction, but it fails when trying to calculate the tunneling rate. Even though the small oscillations in the tail of the Wannier function are barely visible at high lattice depths, they correspond to a small probability of the molecule being in the adjacent site, which is exactly what gives the tunneling probability. So, although a gaussian is a very good approximation for the wavefunction, it underestimates the tunneling probability by an order of magnitude [39].

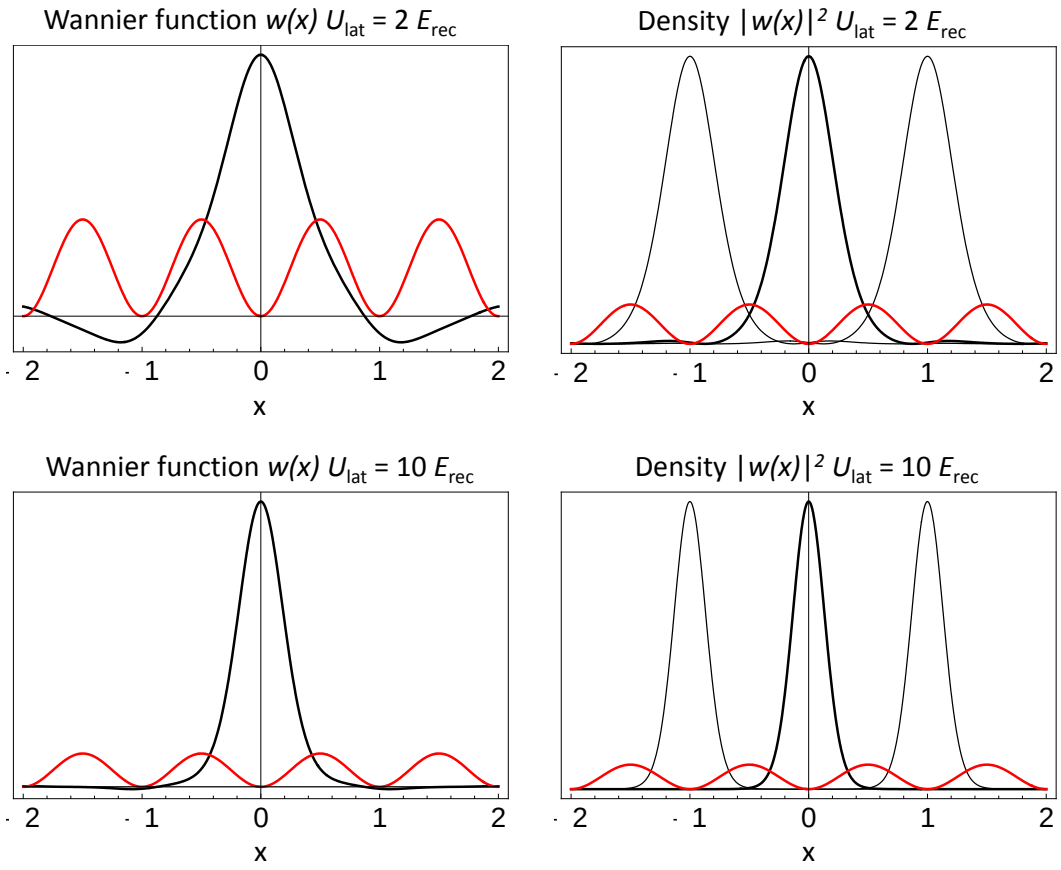

Figure 2.2: The Wannier functions and their corresponding probability density for a 3 E_{rec} (top panels) and a 10 E_{rec} (bottom panels) lattice. The lattice potential is shown in red to indicate the location of the sites. The probability density for three adjacent sites is shown to illustrate the wavefunction overlap which determines the tunnelling rate.

2.4 Experimental realization and charaterization of the lattice

The experimental realization of our 1D lattice is illustrated in figure 2.3. We have a single gaussian beam with a beam waist $w_0 = 250$ μm that is retroreflected to interfere with the incoming beam to form the lattice. This large beam waist has a Rayleigh range of 18 cm, which makes focusing of the lattice beam onto the atoms quite easy. Additionally, we use a 2f-2f imaging system (see figure 2.3) to retroreflect the beam, making the alignment of the retroreflected beam insensitive to both the mirror position and angle. We tilt the lattice with a slight angle of 2.5 degrees relative to the normal of both the glass cell and electric field plates to avoid optical interference with unwanted reflections.

To load the 1D lattice, we start with atoms in a crossed optical dipole trap. The earlier stages of the experiment (MOT, forced RF evaporation in the IP trap, evaporation in the crossed beam optical dipole trap, ect.) are described well in the theses of Josh Zirbel [40] and Kang-Kuen Ni [23]. The intensity of the lattice beam is ramped up over 150 ms. This ramp time is chosen to ensure adiabaticity between bands and minimize heating. The experiments described in chapter 4 are preformed in a combined 1D lattice + crossed optical dipole trap. The combination of the two traps is used to provide tighter radial confinement than would be obtained in the 1D lattice alone.

Because of our limited optical access, we currently have a single set of beams that act both as a crossed dipole trap and as the two horizontal lattice beams in our 3D lattice. Just like the vertical optical lattice beam, each optical dipole trap beam is retro-reflected using a 2f-2f imaging system, but the retro-reflection mirror is placed behind a shutter, which allows us to switch between using the beam as an optical dipole trap or an optical lattice. To load the 3D lattice, we first load our atoms into the 1D lattice as described above and then ramp down the intensity of the two optical dipole trap beams. With the atoms confined entirely in the vertical lattice and the dipole trap beams fully off, we open the shutter such that the optical dipole trap beam is now retroreflected to form a lattice. The intensity of the two horizontal lattice beams is then ramped up over 150 ms to ensure adiabaticity and avoid heating the cloud.

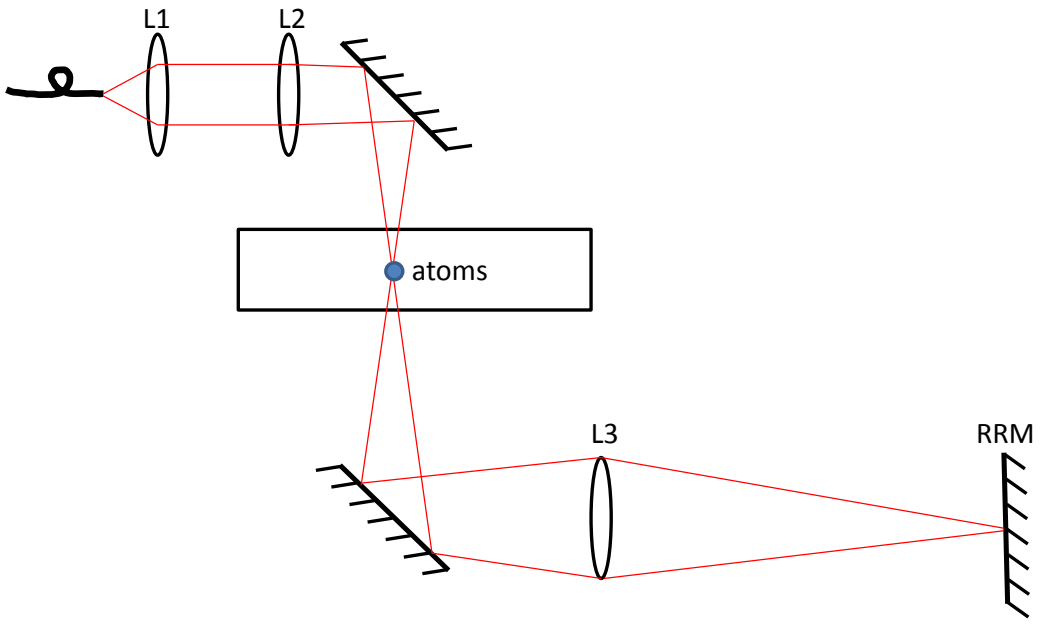

Figure 2.3: A schematic of the vertical lattice. The lattice light comes out of the fiber is columnated by lens L1. Lens L2 focuses the beam onto the atoms/molecules in the center of the cell. L3 is 2f away from the atoms and 2f away from the retroreflection mirror RRM. This 2f-2f imaging system refocuses the lattice onto the atoms while minimizing the sensitivity to small drifts in both the angle and position of RRM.

We align all three lattice beams to the position of the atoms in the magnetic trap (see the thesis of Josh Zirbel [40] for details on the atom preparation in the magnetic trap). For the two horizontal beams that make the crossed dipole trap, this is done by maximizing the load from the magnetic trap into a single dipole trap beam. The alignment of the incoming vertical lattice beam is adjusted one axis at a time by scanning the vertical lattice beam through a cloud of atoms held in just one of the two crossed dipole trap beams. When the vertical lattice beam intersects the dipole trap, the lattice beam provides trapping along the direction of the beam's propagation. We simply minimize the in-trap size in this direction to get the best alignment and then repeat the process using the other dipole trap beam. The retroreflection of all three beams is aligned by pulsing the lattice on for a few μs and maximizing the diffraction of a BEC.

2.5 Diffraction of a BEC

A convenient way to characterize the strength of our lattice is to see the diffraction of a BEC in the lattice [41]. The lattice is a standing wave with periodicity $\lambda/2$, so we can think of this simply as diffraction off of a grating. Physically the atoms in the BEC absorb and then reemit photons from the lattice beam and receive a momentum kick of $2m\hbar k$, where m is an integer. We work in the Raman-Nath regieme where the time in the lattice is much shorter than the trap frequency, so the atoms are stationary during the interaction. When the lattice is suddenly pulsed on the BEC, which has zero momentum, is projected into the even bands of the lattice. Each of these bands has a different energy and will evolve in time according to $\Psi(t) = \exp(-iE_n(q)t/\hbar)\Psi(0)$. After some hold time in the lattice, the lattice is suddenly tuned off and the atoms are projected back into momentum states. The phases acquired by the different Bloch bands during the lattice hold leads to interference in the momentum projections. These interferences produce oscillations in the populations of the momentum components as a function of the hold time as seen in figure 2.4.

To find the lattice depth, we solve the time dependent Schrodinger equation numerically using the first 5 momentum components. Here all the parameters are known except for the lattice depth. We vary the lattice depth and compare to the measured oscillations to minimize χ^2. The

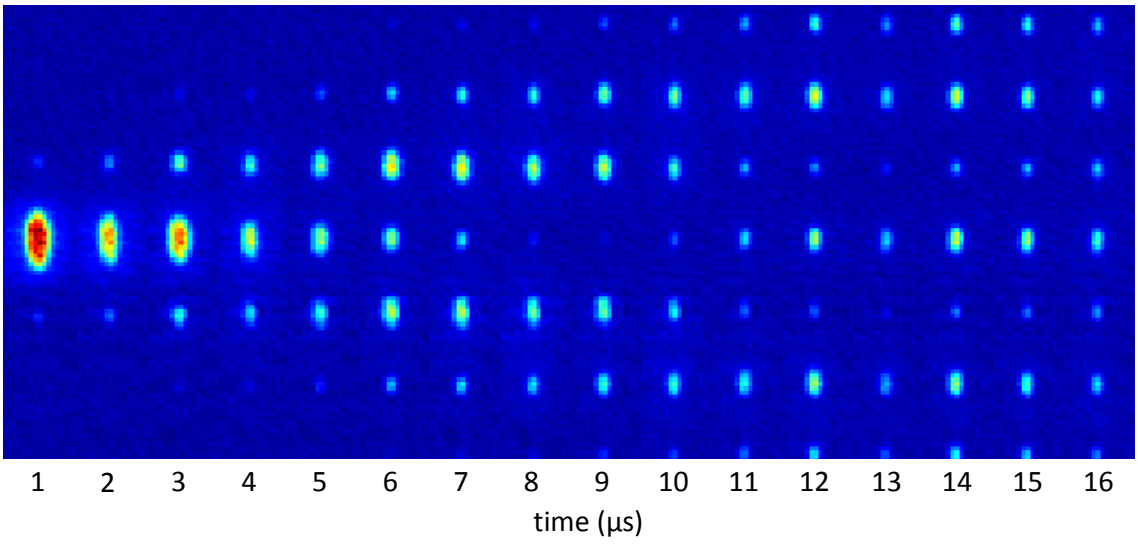

Figure 2.4: The diffraction of a BEC in a vertical optical lattice. Momentum components $p = 0, \pm 2\hbar k, \pm 4\hbar k, \pm 6\hbar k$ are shown after a diabatic release from the trap. The populations oscillate as a function of hold time in the lattice.

fit is shown in figure 2.5.

2.6 Parametric heating

Although Kapitza-Dirac scattering (diffraction of a BEC) allows us to align and calibrate our lattice, it relies on the coherence of a BEC. We would like to have another measure of the trap frequency and trap depth that may be used with fermions or thermal clouds. For this, we can probe the band structure of the lattice directly with parametric heating. Here we modulate the intensity of the lattice, and when the modulation frequency is equal to the energy gap between the ground and second excited band of the lattice, the atoms or molecules will be transferred to the higher band. The added energy from the atoms/molecules in the second excited band heats the cloud, allowing us to identify the parametric heating resonance by looking at the momentum distribution of the cloud. After the modulation, the cloud is released from the trap and the size is measured after time of flight expansion. A typical parametric heating resonance for KRb is shown in figure 2.6.

If the potential was perfectly harmonic, we would only be able to excite transitions from the ground state to other even states ($n = 2, 4, 6...$) because of the even parity of the drive. But due to the anharmonicity of the sinusoidal potential of the lattice it is possible to drive transitions from the ground state to odd excited states, but the coupling is much smaller [42]. By knowing the polarizability, beam waist, intensity, and the attenuation of the light as it passes through the glass cell and electric field plates, we can predict the trapping frequency to within 10%, which prevents us from misidentifying the parametric heating resonance. A small amplitude (a peak-to-peak modulation $< 15\%$ of the total lattice intensity) should be used for the drive. If the transition is driven too hard, the molecules will be excited to $n = 2$ and then again up to $n = 4$, which due to the anharmonicity of the potential is slightly lower in frequency. If the transition is overdriven, the observed resonance will be broadened and systematically shifted towards lower frequency.

It is common to say that the parametric heating measures the trap frequency. In the deep lattice limit, where the potential can be approximated by a harmonic potential, the transition from

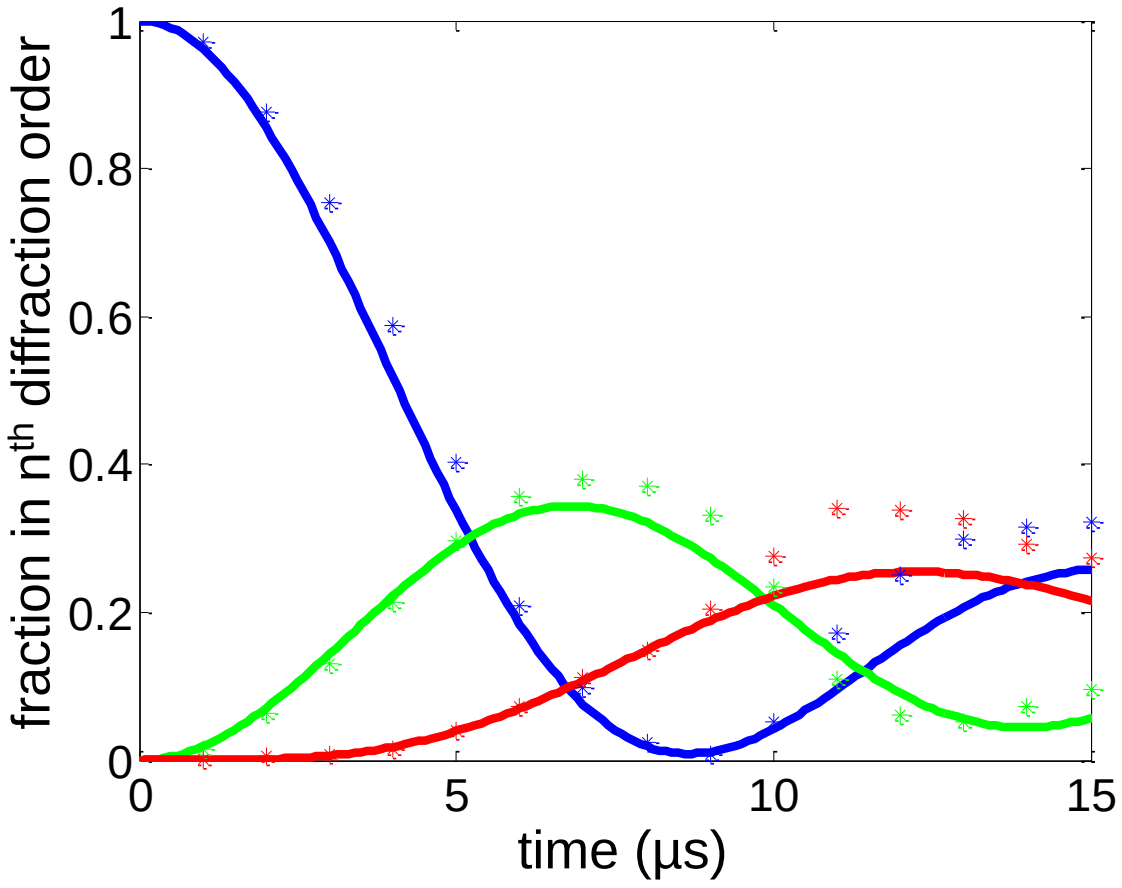

Figure 2.5: The relative populations in the $p = 0$ (blue), $p = \pm 2\hbar k$ (green), and $p = \pm 4\hbar k$ (red) diffraction orders. The solid lines are a fit to the data using a numerical solution to the time dependent Schrodinger equation to extract the lattice depth $V_0 = 43(4)\ E_{\mathrm{rec}}^{Rb}$.

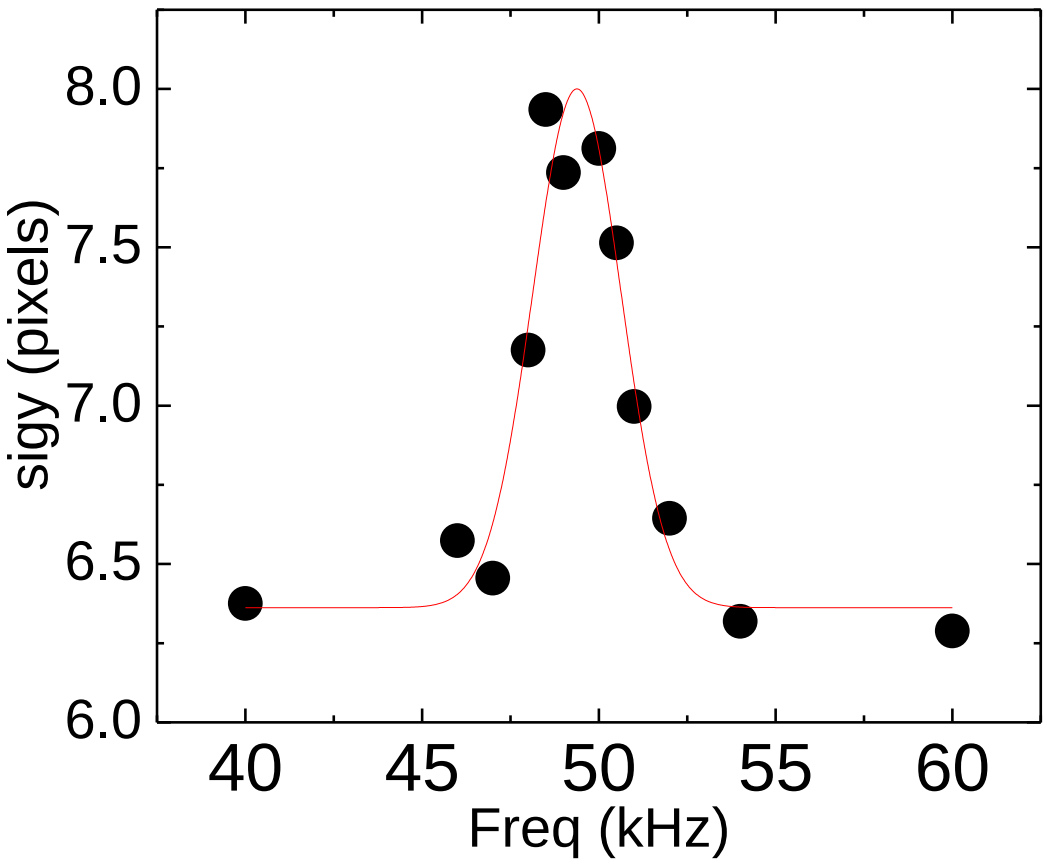

Figure 2.6: A parametric heating resonance for KRb in a 94.3(3) $E_{\mathrm{rec}}^{\mathrm{KRb}}$ lattice. The amplitude of the lattice is modulated sinusoidally for 4 ms with a peak to peak amplitude 10% of the total intensity. The size is measured after 3 ms time of flight. A gaussian is fit to the observed resonance to find the center of 49.37(9) kHz.

the ground band to the second excited band occurs at two times the trap frequency. However, for the lattice depths accessible in our experiment we find that the anharmonicity of the trap causes a significant deviation from this simplistic expectation, even when exciting only the $n = 0 \rightarrow n = 2$ transition. In figure 2.7, twice the trap frequency (red) along with the frequency of the $n = 0 \rightarrow n = 2$ transition (black) are plotted versus the lattice depth. The solid black line is the transition at $q = \hbar k/2$ and the black dashed lines are the transition at the edges of the Brillouin zone ($q = 0$ and $q = \hbar k$). A thermal gas (or Fermi gas) will have atom/molecules across much of the Brillouin zone, which for lattice depths less than 25 E_{rec} will increase the width of the parametric heating resonance. More importantly, care must be taken when measuring trap depths below 25 E_{rec} with parametric heating. The frequency measured with a BEC, which only populates $q = 0$ (the higher dashed line in figure 2.7), and a thermal cloud, which will populate all the quasimomentum with a thermal distribution (spanning the entire range between the two dashed lines in figure 2.7), will be different.

Figure 2.8 shows ratio between the parametric heating resonance and twice the trapping frequency. Even at 100 E_{rec}, there is still a 10% difference. In practice we sidestep this potential problem by comparing our measured parametric heating resonance to an exact solution of the band energies (shown in figure 2.9) to extract the trap depth. This trap depth ($U = 4\alpha I$) can then be inserted in to equation 2.4 to get the trap frequency.

2.7 Band Mapping

Once the atoms or molecules are loaded into the lattice, we would like to know the distribution of the atoms/molecules in the different bands of the lattice. The population of the bands can be directly measured by adiabatically ramping down the lattice and measuring the free space momentum distribution [43, 44]. Usually time-of-flight imaging is done after the trap is rapidly switched off. This diabatic turn off projects the wavefunction onto momentum space. However if we ramp down the lattice slowly compared to the spacing between bands, the quasimomentum in the lattice is mapped onto the free momentum measured in time-of-flight imaging.

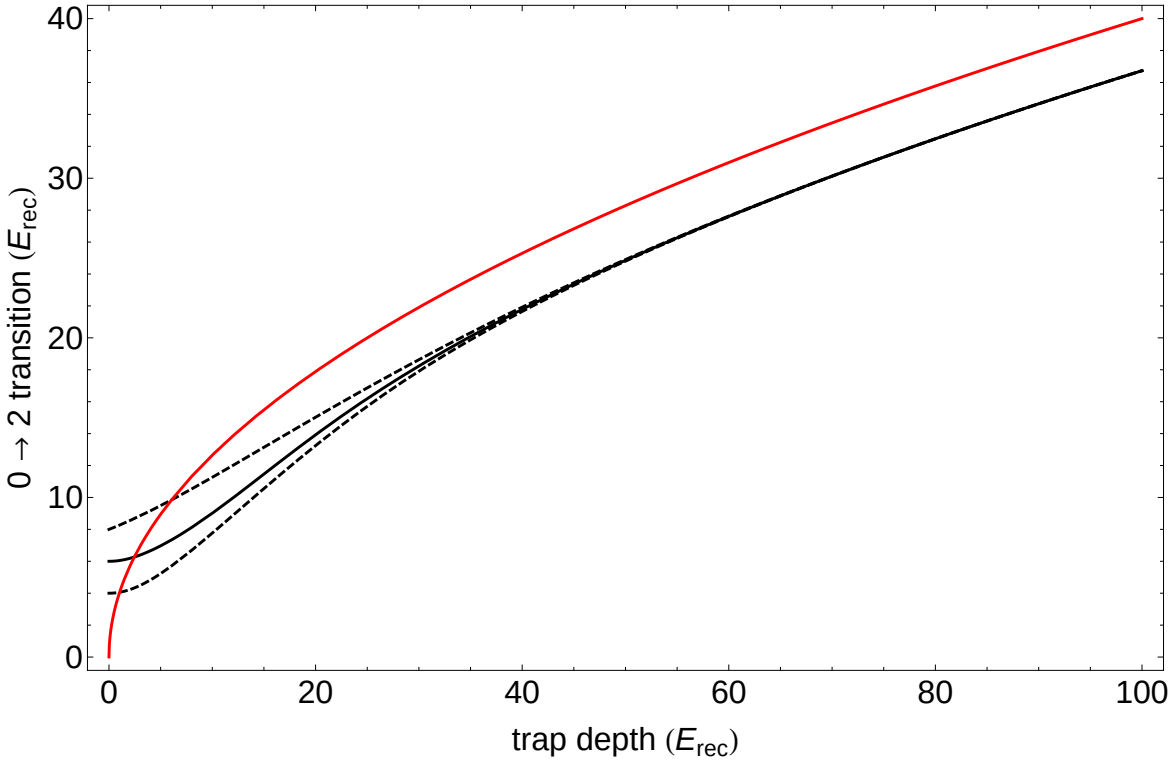

Figure 2.7: The transition from the ground band to the second excited band (in E_{rec}) as a function of the trap depth. The solid black line is the transition at the center of the band ($q = \hbar k/2$). The dashed black lines represent the transition at the edges of the Brillouin zone ($q = 0$ and $q = \hbar k$). Twice the trapping frequency is plotted in red.

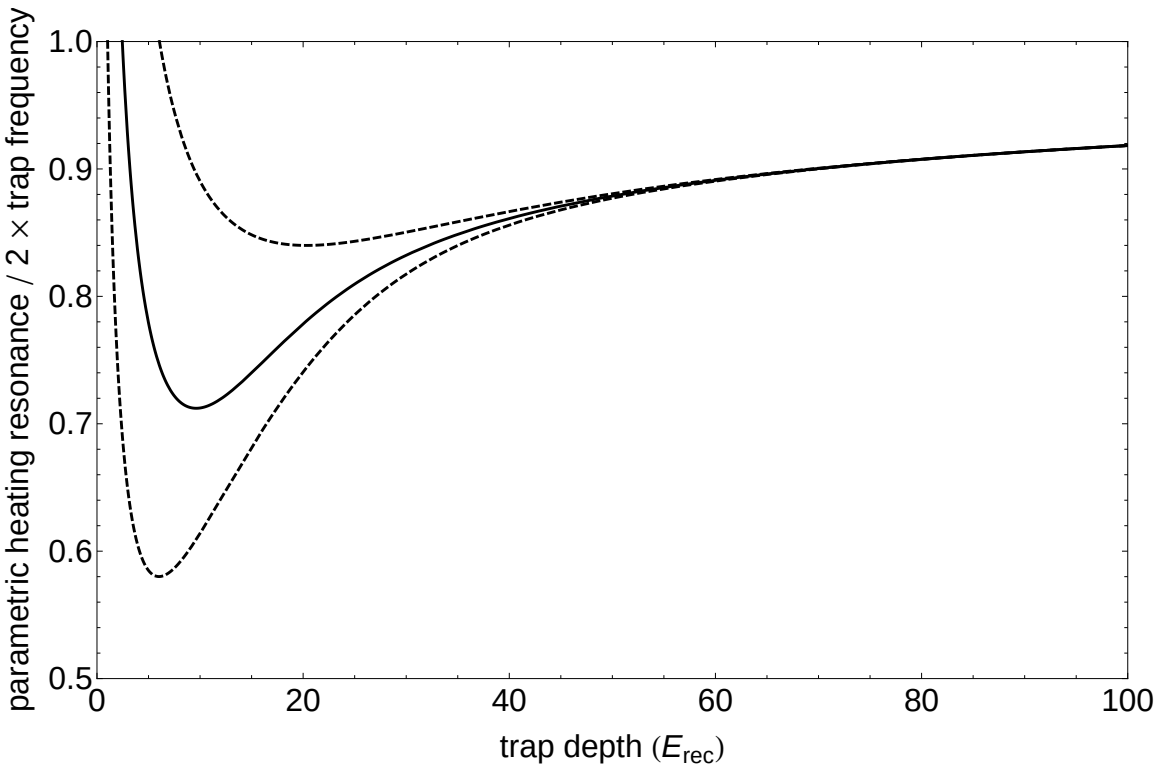

Figure 2.8: The parametric heating resonance divided by twice the trap frequency as a function of trap depth. The dashed lines are the transitions at $q = 0$ (bottom) and $q = \hbar k$ and the solid line is the transition frequency at $q = \hbar k/2$.

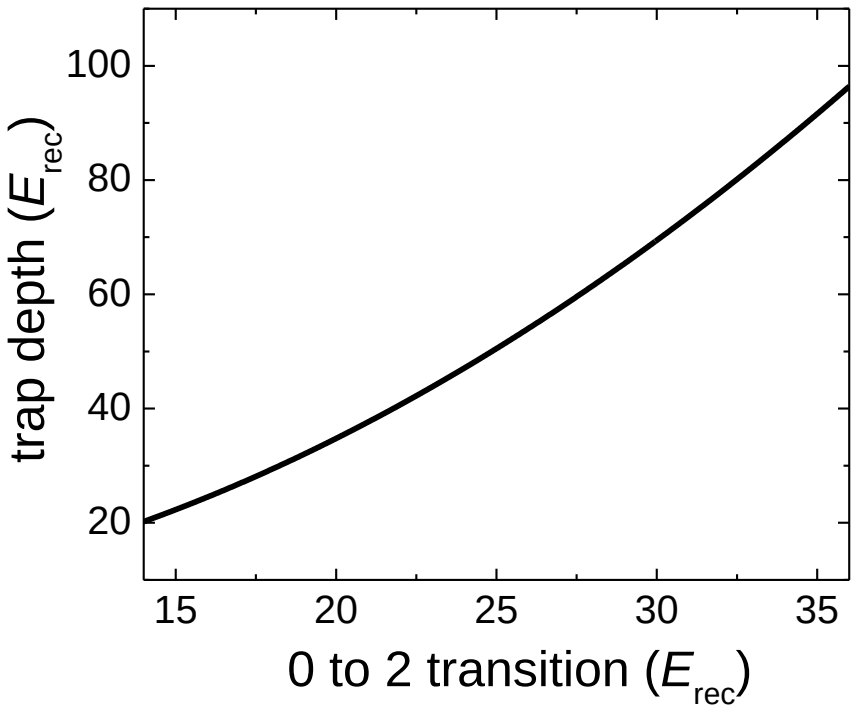

Figure 2.9: The depth of the lattice versus the parametric heating resonance. From this graph we can read off the trap depth from our resonance. Units are given in E_{rec} to keep the plot general for particles of any mass.

The speed for the ramp down must be chosen carefully to ensure the distribution in time of flight does indeed match the distribution in the lattice. The first criteria is that the ramp should be adiabatic with respect to the atomic motion in a single lattice site. This means the ramp must be slow compared to the band spacing, which ensures that we avoid changing the distribution between the different bands. But this criteria cannot be perfectly fulfilled because the band gap goes to zero as the lattice is ramped off. This problem is most evident at the edge of the Brilloiun zone where the bands spacing is the smallest. Here the nonadiabaticity causes a "smearing" of the sharp edges of the Brillouin zone. To further complicate matters, if the ramp is too slow the atoms will tunnel out of the lattice during the last part of the ramp due to the force of gravity. By looking both at the asymmetry of the background due to atoms that leaked out of the lattice during the ramp and the rounding of the Brillouin zone edges, we empirically choose a ramp down time of 500-1000 μs.

The momentum distribution after 18 ms time of flight for a K cloud after band mapping is shown in figure 2.10. A hot K cloud (T=400 nK) was loaded into the lattice to ensure population of both the 0th and 1st bands. We integrate across the image perpendicular to the lattice direction to increase the signal to noise ratio. This trace is shown in figure 2.10b. Because fermions uniformly fill the 0th band, we observe a flat distribution for $-\hbar k < p < \hbar k$. There are also atoms almost uniformly distributed across the 1st excited band of the lattice which appears on either side of the 0th band at $-2\hbar k < p < -\hbar k$ and $\hbar k < p < 2\hbar k$. However, the 1st band is not full, so we see "shoulders" on either side of atom in the 0th band. To extract the relative populations, we simply count the number of atoms in each of the zones. In practice this is done by fitting a series of Heaviside functions (which give the flat topped distributions for each band) convoluted with a gaussian (which accounts for the smearing at the edge of the zones which is a result of not being perfectly adiabatic on the ramp down). The only free parameters in the fit are the amplitude for the 0th and 1st bands and the width of the momentum smearing. The fit to figure 2.10b reveals 28% of the atoms in the 1st excited band.

We can remove the atoms in higher bands by lowering the lattice depth and waiting for the atoms in higher bands to tunnel out of the lattice. We ramp down the lattice in 20 ms, hold

at 3.3 $E_{\mathrm{rec}}^{\mathrm{K}}$ for 1 ms, and then ramp the lattice the rest of the way down in 500 μs to map the quasimomentum into real momentum. The momentum distribution and its corresponding fit after filtering are shown in figure 2.10c,d. Here we are left with only the lowest band and the sharp edges of the Brillouin zone are revealed. This image also reveals a major limitation of our band mapping technique, which is that we are unable to accurately fit populations in the exited bands that are smaller than 5%. This is largely due to the slight asymmetry in the band mapping image that is a result of atoms tunneling out of the trap during the ramp. This asymmetry is not currently accounted for in our simple fitting program, and including it may increase our sensitivity. Even so, it seems unlikely that band mapping can distinguish between an empty band or a band with a few percent population.

2.8 An easier way to detect atoms/molecules in higher bands

In the deep lattice limit, the wavefunctions of the molecules in the optical lattice are well described by the eigenstates of the simple harmonic oscillator. The excited bands will not only have a larger extent in real space, but in momentum space as well. Because the wavefunction of the excited bands has a larger momentum spread, if higher bands are populated, it will be evident in the size of the cloud observed in time-of-flight imaging. Molecules in higher bands will increase the width of the fitted gaussian. To quantitatively extract a percentage in higher bands I simulated the cloud in Mathematica using a thermal distribution to populate the eigenstates of a harmonic oscillator. The probability density for all the atoms is summed up and then fit with a single gaussian. The fit width as a function of percentage in higher bands is plotted in figure 2.11. We see that for 10% of the atoms in higher bands a 10% increase in the momentum is observed.

In figure 2.12, we plot the measured size of a K cloud in time of flight vs. the population in higher bands measured with band mapping. The population in higher bands was varied by changing the initial temperature of the K cloud before it was loaded into the optical lattice. The theory curve from figure 2.11 is overlaid with no free parameters. The size with no population in the excited bands is given by the harmonic oscilator length in momentum space multiplied by the

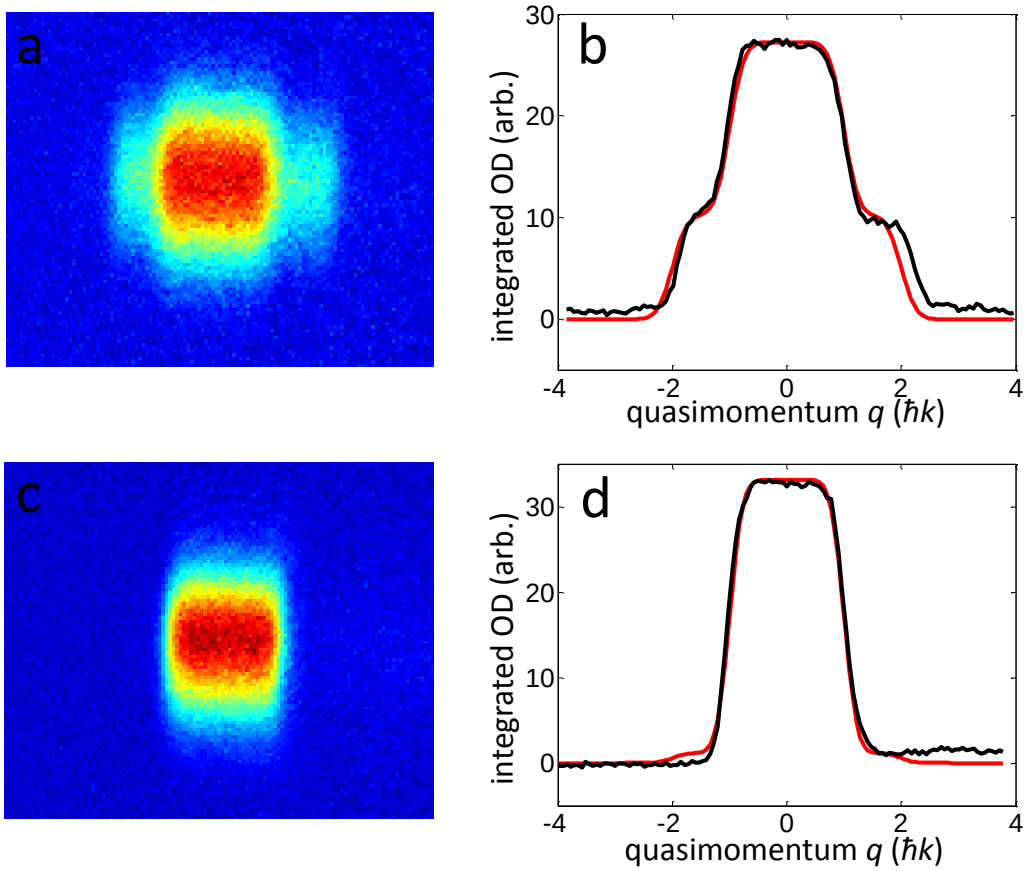

Figure 2.10: Band mapping K atoms in a 1D lattice to measure the population in higher bands. In a and b 28% of the atoms are in the second band. By holding in a weak lattice with depth 3.2 $E_{\mathrm{rec}}^{\mathrm{K}}$ for 1 ms we allow these atoms in higher band tunnel out of the lattice leaving only atoms in the lowest band as shown in c and d. The black trace is the OD of the cloud integrated over the vertical direction (perpendicular to the lattice) to increase signal to noise. The fit is shown in red.

expansion time, t:

$$\sigma_{n=0}(t) = t\sqrt{\frac{\hbar\omega}{2m}}. \tag{2.11}$$

Equation 2.11 assumes the cloud is fully in momentum space, which means the in-trap cloud size is negligible compared to the expanded cloud size. This criteria is easily met with our vertical lattice where the in-trap cloud size is less than one pixel on our camera (one pixel is 5.44 μm at the atoms). It is evident in figure 2.12 that the simple theory underestimates the size for more than 20% of atoms in excited bands. The higher bands have a larger momentum spread than would be expected from the simple picture of a harmonic oscillator, because of the anharmonicity of the lattice potential. This makes the size in expansion difficult to use as a exact calibration of the band populations, but it is still very useful. Most of the time we simply want to check that all the atoms are in the ground band, and a single time-of-flight measurement to ensure that the size matches with equation 2.11 is often the quickest and easiest way to get at the band population.

2.9 How to load just one band

To understand the loading of the lattice, it is instructive to look back at the structure of the Bloch bands with no optical lattice in figure 2.1a. Without an optical lattice, the band structure is simply the energy of a free particle given by $\frac{p^2}{2m}$ that is reflected at the edge of the Brillouin zone. As soon as the lattice is turned on any particle with $p > \hbar k$ will be transported into an excited band of the lattice. This sets an upper limit on the energy of a gas that can be loaded into a single band of $E = \frac{\hbar^2 k^2}{2m} = 1E_{\text{rec}}$. A gas with a temperature larger than E_{rec}/k_B, or even a Fermi temperature larger than this, will have atoms in the excited Bloch bands. This means that for a fixed temperature, it is easier to load lighter particles into the lattice because E_{rec} scales inversely with the mass, for example $E_{\text{rec}}^K = 210$ nK and $E_{\text{rec}}^{\text{KRb}} = 66$ nK. For this reason we load our atoms into the lattice and then create Feshbach molecules in the lattice from a gas of atoms in the lowest band of the lattice.

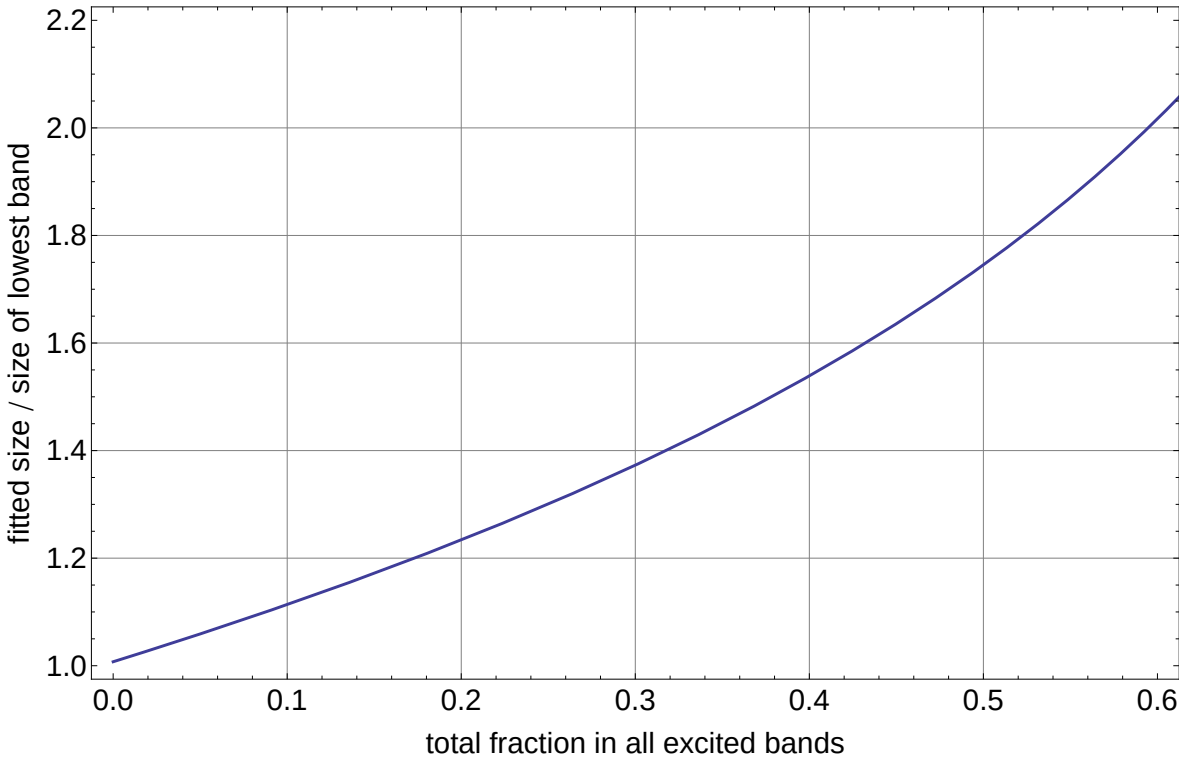

Figure 2.11: The size of a gaussian fit to a simulated with a thermal population of higher bands, imaged after release from the lattice.

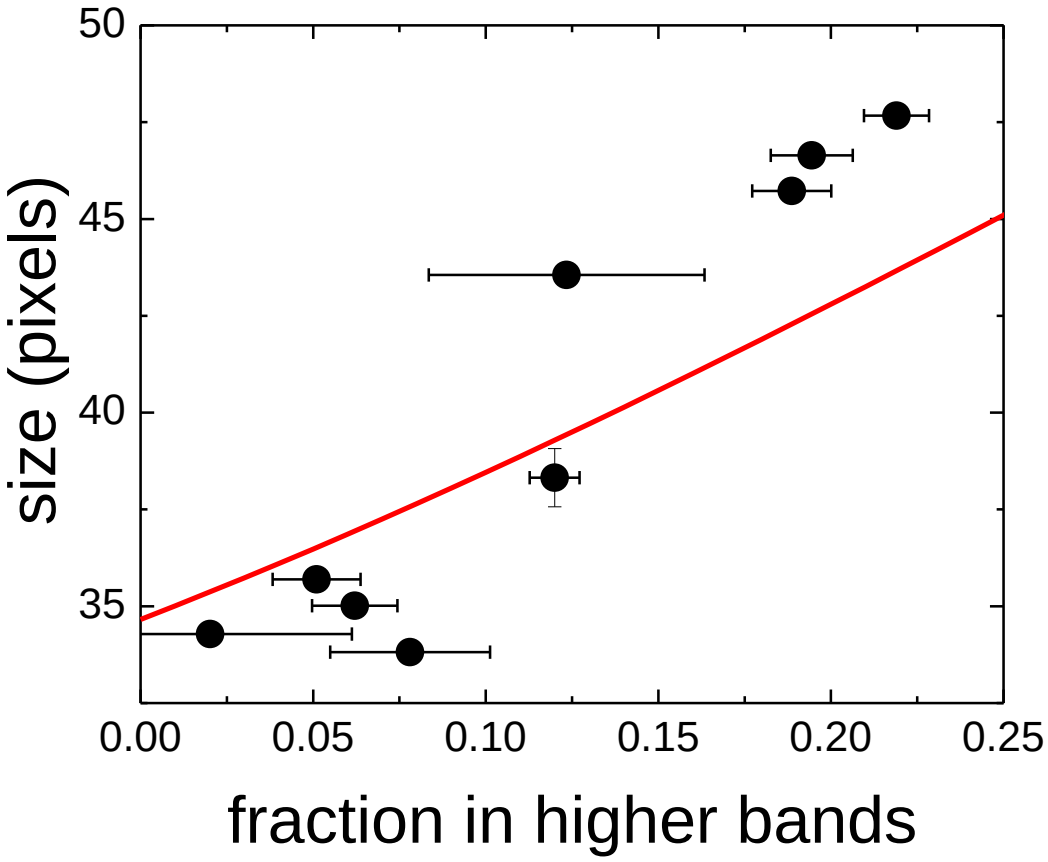

Figure 2.12: The size of a gaussian fit to a K cloud released from the lattice. The population of higher bands was measured using band mapping.

Chapter 3

Universal chemical reactions in KRb

The creation of ultracold KRb in the absolute ground state was exciting for many reasons. Not only was it the first realization of polar molecules in the quantum regime, which opened the way for studies of novel quantum gasses with long-range interactions, but KRb is also chemically reactive giving us the ability to study ultracold chemistry, which up until this point was completely unexplored. At these ultra-low temperatures, chemical reactions might seem counter-intuitive, but KRb's chemical reactions are remarkably easy to understand for two main reasons. First, bimolecular chemical reactions for KRb have no reaction barrier and require no activation energy (this is generally true of all the bialkali molecules with energetically favorable chemical reactions)[21]. Without a reaction barrier, the chemical reaction will always take place (regardless of temperature) if the two molecules come sufficiently close together ($\sim 10a_0$). Secondly, ultracold collisions, where particles scatter only in the lowest angular momentum channel, are governed entirely by quantum statistics, so the rate at which the molecules enter the short-range part of the potential, where chemical reactions happen with near unit probability, can be understood from the Bethe-Wigner threshold laws [45, 22, 6]. Moreover, we observe that KRb's bimolecular chemical reactions are universal in the sense that the details of the short-range potential do not influence the reaction rates, which can be determined using only knowledge of the long-range potentials [46].

In addition, the amount of control that we have over the preparation of our system gives us unique abilities to control the chemical reaction rate. By controlling the internal state of the molecule, we can prepare the molecules in a single quantum state, or an incoherent or coherent

mixture of our choosing. This modifies the quantum statistics of the collision partners and determines whether or not there is an angular momentum barrier that the molecules must tunnel though to chemically react. We can modify the long-range potential directly by applying a DC electric field to orient the molecules and "turn on" the dipole-dipole interaction between molecules. And we will show in Chapters 4 and 5 that we can control the orientation of the molecules during a collision (stereodynamics) and even suppress chemical reaction all together by controlling the external motion state of the molecule in an optical lattice.

In this chapter I will present the studies of the chemical reactions of KRb confined in a three dimensional optical dipole trap. Much of this chapter and its figures will be take directly from references [2, 1] of which I am an author. This chapter will also necessarily overlap with the discussions in the theses of K.-K. Ni [23] and M.H.G. de Miranda [24].

3.1 Bimolecular chemical reactions

In references [20, 19] we showed that we could transfer KRb molecules to the absolute lowest energy state of the molecular potential, namely, the ground electronic, vibrational, rotational, and hyperfine state. One might think that in this absolute ground state the molecules would be assured to be collisionally stable. But for molecules, chemistry is an possible inelastic collision mechanism. In table 3.1, I show the binding energies of all possible combinations of K and Rb. It turns out that only KRb + KRb $\rightarrow$ K_2 + Rb_2 is a exothermic reaction. By chemistry standards it's not very exothermic, as it only releases 10.3(4) cm^{-1} worth of energy. In fact the binding energies of the the reactants and products were so similar that it was not known for certain if the reaction would be exothermic or endothermic until after the transfer to the ground state nailed down the binding energy of KRb [19]. But compared to the energy scales in our experiment, the released energy in this reaction is enough to easily give the products enough kinetic energy to escape the trap.

Experimentally, the chemical reaction manifests itself as molecules disappearing from our optical dipole trap. Once we have prepared a gas of ground-state molecules and removed all unpaired atoms, we see the molecules disappear on a timescale of a few seconds. Figure 3.1 shows a

Molecule	$v = 0$ binding energy (D_0)	reference
$^{87}Rb_2$	3965.8(4) cm^{-1}	[47]
$^{40}K^{87}Rb$	4180.417 cm^{-1}	[19]
$^{40}K_2$	4405.389(4) cm^{-1}	[48]
$^{40}K_2^{87}Rb$	6080($\pm$300) cm^{-1}	[49]
$^{40}K^{87}Rb_2$	5900($\pm$300) cm^{-1}	[49]

Table 3.1: Relevant molecular binding energies involved in possible chemical reactions. The binding energies are given with respect to the threshold energy for free atoms in the absence of magnetic field. The $^{87}Rb_2$ and $^{40}K_2$ binding energies include the isotope shifts from the data in the respective references.

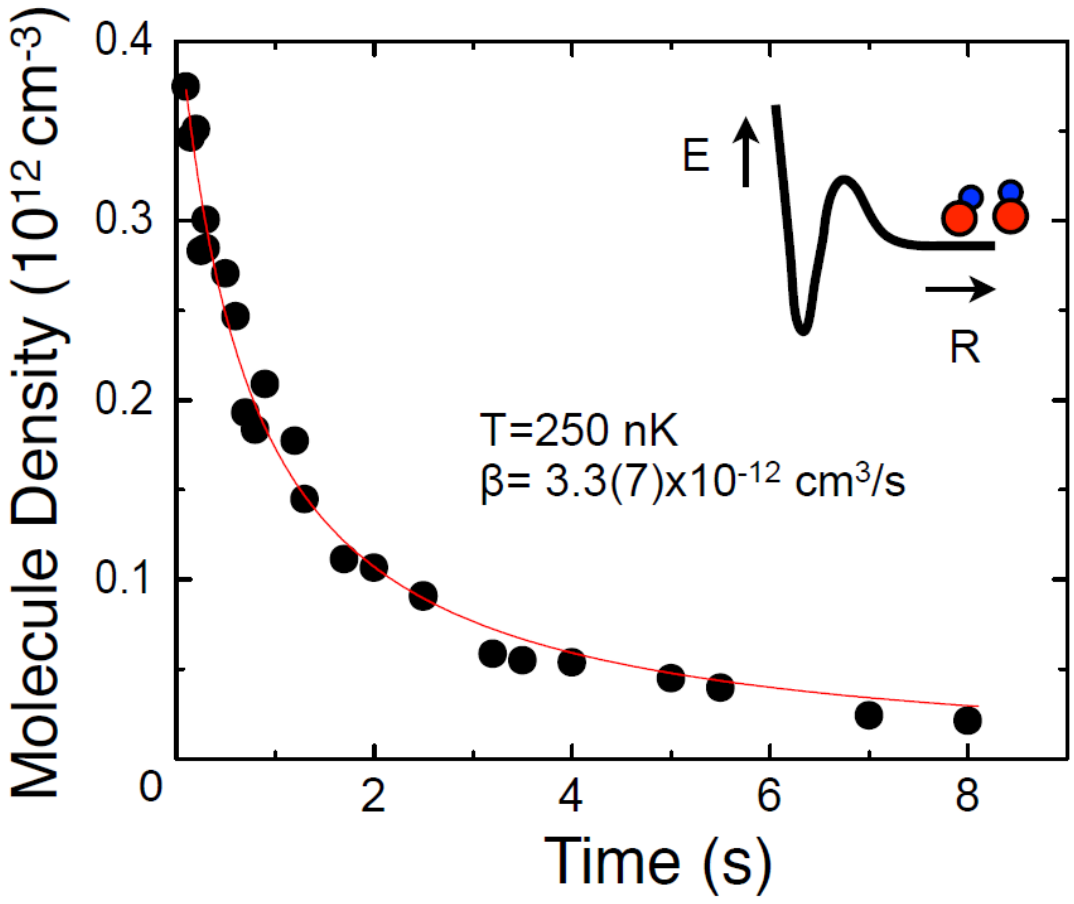

Figure 3.1: A sample molecular density decay vs time for inelastic collisions between indistinguishable fermionic molecules in the ro-vibronic ground-state of $^{40}K^{87}Rb$. Here the molecules are prepared in a single hyperfine state, $|m_I^K = -4, m_I^{Rb} = 1/2\rangle$, and the molecular density-weighted density decays slowly with a rate coefficient of $3.3(7)\times10^{12}$ cm^3/s at T = 250 nK. Figure reproduced from reference [1].

typical loss curve. We see that the molecular density-weighted density, n, decays follows a two-body loss curve that is the solution to the following differential equation,

$$\frac{dn}{dt} = -\beta n^2 - \alpha n \tag{3.1}$$

The first term describes two-body loss of molecules. Here, β is the two-body loss coefficient and has units of cm^3/s. As the molecules are lost, we also observe an increase in temperature, which decreases the density without molecule loss. For each data set we fit the measured temperature to a line to obtain the heating rate c with units of K/s, which we use to calculate $\alpha = \frac{3}{2}\frac{c}{T_0+ct}$, where T_0 is the initial temperature. This heating can be understood from the dynamics of the loss (and will be explained in section 3.5), but for now we enter it in as an empirically measured decrease in density. The data fits well to this two-body decay, and moreover, does so with the same loss coefficient for data taken with molecules in the the lowest hyperfine state($|m_I^{\mathrm{K}} = -4, m_I^{\mathrm{Rb}} = 3/2\rangle$) as well as for data taken with the molecules in an excited hyperfine state ($|-4, 1/2\rangle$).

Although we do not have the ability to measure the product states of the chemical reaction, for a pure gas of molecules in the lowest hyperfine state, there is only one energetically allowed reaction channel that will result in two-body loss, KRb + KRb $\rightarrow$ K_2 + Rb_2. It turns out that KRb + KRb $\rightarrow$ K_2 + Rb_2 is a barrierless chemical reaction, meaning that it requires no activation energy to chemically react. With no chemical reaction barrier, the rate at which the molecules react will be set entirely by the rate at which they come sufficiently close to chemically react ($\sim 10a_0$). At the ultralow temperatures in our experiment, collisions with large impact factors and correspondingly large centrifugal barriers are frozen out and the collisions are dominated by a single partial wave. Because $^{40}\mathrm{K}^{87}\mathrm{Rb}$ is fermionic, the collisional wavefunction has to be antisymmetric with respect to particle exchange. So, if our molecules are all prepared in a single hyperfine state, the lowest allowed partial wave is the $L = 1$ p-wave. The height of the $L = 1$ angular momentum barrier for KRb-KRb collisions is $k_B \cdot 24\mu K$. With the height of this barrier a full order of magnitude higher than the collision energies, the rate at which the molecules tunnel through this barrier and into

the short range part of the potential where chemistry occurs will be given by the Wigner threshold laws. Specifically, for identical fermions tunneling through a p-wave barrier, the rate should scale linearly with the collision energy [6].

We show the measured chemical reaction rate β as a function of temperature in figure 3.2. We fit the data to a power law $\beta(T) \propto T^L$ to find $L = 1.1(2)$ in agreement with the predicted p-wave threshold law. We observe that the loss rates for the $|-4, 1/2\rangle$ and $|-4, 3/2\rangle$ states are the same to within the error. So although hyperfine changing collisions are possible for the $|-4, 1/2\rangle$ state, the loss rate is not significantly increased.

3.2 Two models to understand the loss

To understand the loss rates, we use two models: a simple quantum threshold model (QT) developed by Goulven Quéméner and John Bohn, and a model that uses the formalism of multi-channel quantum defect theory (MQDT) developed by Paul Julienne. The inelastic collisional cross section for indistinguishable particles is given by

$$\sigma^{in}_{L,m_L} = \frac{\hbar^2 \pi}{\mu E_c} |T^{in}_{L,m_L}|^2, \tag{3.2}$$

where E_c is the collisional energy and T^{in}_{L,m_L} is the inelastic transition matrix, L is the relative angular momentum of the two molecules, and m_L is its projection onto the quantization axis. The inelastic rate coefficient for a given temperature T is given by

$$\beta^{in}_{L,m_L} = \langle \sigma^{in}_{L,m_L} v \rangle = \int_0^\infty \sigma^{in}_{L,m_L} v f(v) dv, \tag{3.3}$$

where

$$f(v) = 4\pi \left(\frac{\mu}{2\pi k_B T} \right)^{3/2} v^2 \exp[-(\mu v^2)/(2k_B T)] \tag{3.4}$$

is the Maxwell-Boltzmann distribution for the relative velocities for a given temperature.

In the QT model, we assume $|T^{in}_{L,m_L}|^2 = 1$ for all collision energies, E_c, equal to or above the p-wave barrier (this is just the classical Langevin capture rate [50]). At collision energies less than the p-wave barrier we scale the loss rate according to the Bethe-Wigner threshold laws. Here the

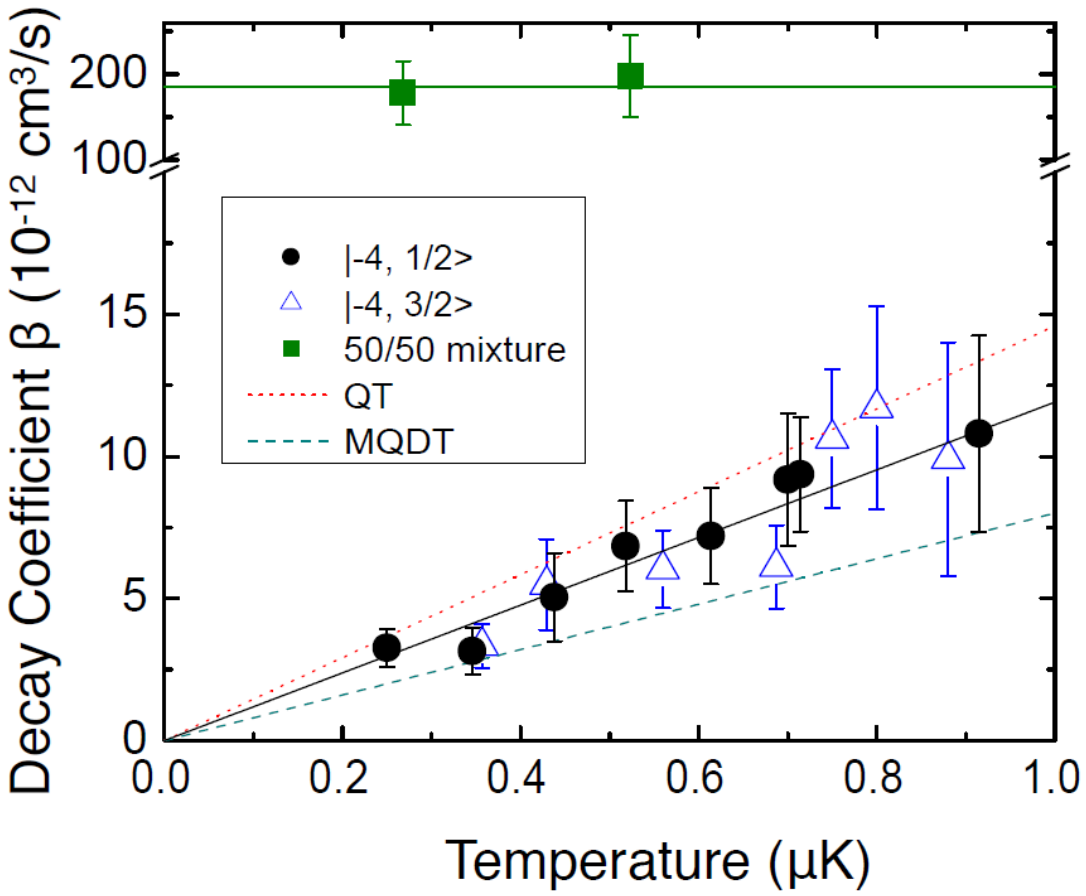

Figure 3.2: Inelastic collision rate coefficient vs temperature for fermionic molecules in the ro-vibronic ground state of $^{40}K^{87}Rb$. For the lower loss coefficients, the collision rate coefficients were measured for molecules prepared in either $|4, 1/2\rangle$ (closed circles) or the lowest energy state $|4, 3/2\rangle$ (open triangles). We observe the loss rate increases linearly with temperature for spin-polarized molecules, which verifies that the dominant collision channel is p-wave. A linear fit (solid line) to the $|4, 1/2\rangle$ data yields the temperature-dependent loss rate to be $1.2(3) \times 10^5$ cm^3/s/K. For the $|4, 3/2\rangle$ case, where the collisional loss can only be due to chemically reactive scattering, the loss rate is similar. The dotted and dashed lines are theoretical predictions from the QT model and MQDT (describe in the text), respectively. In contrast, when the molecular sample is prepared in a mixture of two hyperfine spin states, $|4, 1/2\rangle$ and $|4, 3/2\rangle$ (filled squares), s-wave collisions dominate. Here, we observe a temperature-independent decay rate that is $10 - 100$ times higher than for the spin polarized case. Figure reproduced from reference [1].

$|T|^2 = (\frac{E_c}{V_b})^{(L+1/2)}$, where V_b is the height of the barrier. Using this assumption, we approximate the inelastic cross section and rate coefficient by

$$\sigma^{in}_{L,m_L} = \frac{\hbar^2\pi}{\mu V_b^{L+1/2}} E_c^{L-1/2} \tag{3.5}$$

$$\beta^{in}_{L,m_L} = \frac{\sqrt{2}\hbar^2\pi}{\mu^{3/2} V_b^{L+1/2}} \langle E_c \rangle \tag{3.6}$$

where $\langle E_c \rangle$ is the average collision energy.

We solve for the height of the barrier of the potential given by

$$V(R) = \frac{\hbar^2 L(L+1)}{2\mu R^2} - \frac{C_6}{R^6} \tag{3.7}$$

and obtain

$$V_b = \left[\frac{(\hbar^2 L(L+1))^3}{54\mu^3 C_6} \right]^{1/2}. \tag{3.8}$$

Inserting Eq. 3.8 in Eq. 3.6 and using $\langle E_c \rangle = 3k_B T/2$ we get

$$\beta^{in}_{L=1,M_L} = \frac{\pi}{4} \left(\frac{3^{13}\mu^3 C_6^3}{\hbar^{10}} \right)^{1/4} k_B T. \tag{3.9}$$

This is the rate for each M_L channel, to get the overall rate we must multiply by 3. Using a van der Waals dispersion coefficient of $C_6 = 16130$ a.u. for KRb-KRb with an uncertainty of $\pm 10\%$ [51], the slope of the rate coefficient is predicted to be $1.5(1) \times 10^{-5}$ cm^3/s/K, which agrees with the experimental measurements of $1.2(3) \times 10^{-5}$ cm^3/s/K ($|-4, 1/2\rangle$) and $1.1(3) \times 10^{-5}$ cm^3/s/K ($|-4, 3/2\rangle$).

In the MQDT model, the loss rate coefficient is found directly by calculating the quantum tunneling rate through the p-wave barrier [52], and gives $\beta = 0.8(1) \times 10^{-5}$ cm^3/s/K, which also agrees with the measured value within mutual uncertainties. Both of these calculations know nothing of the short-range potential yet give excellent agreement with the experiment, indicating that these chemical reactions are universal in the sense that they do not depend on the details of the short-range potential and can be estimated using only knowledge of the long-range interactions [46].

3.3 Chemical reactions between distinguishable molecules

The p-wave barrier that set the chemical reaction rate is a consequence of the two colliding molecules being indistinguishable spin-polarized fermions. If however, the gas is prepared in a 50-50 incoherent mixture of two different hyperfine states, then s-wave collisions are allowed and the chemical reaction rate will be very different. Here, the molecules are still identical fermions, so the wavefunction must still be antisymmetric under particle exchange, but because the molecules can be distinguished by their hyperfine state, the antisymmetry can be incorporated in the internal state, which allows the collision to proceed via a symmetric s-wave collision.

With the gas in a incoherent 50-50 mixture of the $|-4, 3/2\rangle$ and $|-4, 1/2\rangle$ states, we measure the time-dependant number density of the molecules for both hyperfine states. We observe the same loss rate for both states, consistent with loss dominated by collisions between distinguishable molecules in different spin states. As shown in figure 3.2, we obtain a rate coefficient of $1.9(4)\times10^{-10}$ cm^3/s. The data are consistent with a rate that is independent of temperature as predicted by the Bethe-Wigner threshold laws.

The QT model is unable to make any predictions for the s-wave rates, but the collision rates can be estimated using the MQDT model. Here, it is assumed that when the molecules approach each other within the van der Waals length $\overline{a}$, chemical reactions occur with near-unity probability. The universal loss rate coefficient $\beta = 2(h/\mu)\overline{a}$ [46] predicts a loss rate of $\beta = 0.8\times10^{-10}$ cm^3/s, which is a factor of two lower than the experimentally observed rate. This suggests that perhaps the reaction is not entirely universal and that there is some probability of reflection of the colliding species back into the entrance channel, which can provide either constructive or destructive interference, depending on the details of the short-range potential.

3.4 Control of chemical reactions with a DC electric field

In the previous section, I showed that the chemical reaction rate of two indistinguishable molecules is determined by the long-range potential. This suggests that the chemical reaction rate

could be modified, and even suppressed with appropriate control over the long-range potential. Fortunately polar molecules give us exactly this ability to modify the long-range potential by applying an external electric field, which induces a long-range, $1/r^3$, dipole-dipole interaction between molecules. We can control the strength of these dipole-dipole interactions, which is characterized by an effective induced dipole moment d, by applying an external electric field to align the molecules along the axis of the electric field. As the applied field strength is increased, the molecules become more aligned and have stronger interactions.

When we apply an electric field, we see the lifetime of the molecule gas decrease as shown in figure 3.3. Just as before in the zero electric field case, we fit the data to a two-body loss curve with a linear heating rate (Eqn. 3.1) At higher induced dipole moments, the observed heating rate can be quite large, but we limit our data to a range where the temperature increases by at most 50%. Figure 3.4 shows a summary of our experimental data in a plot of β/T_0 as a function of the induced dipole moment d. The Bethe-Wigner threshold laws for inelastic loss, which we verified in the case of zero electric field, still hold here even in the presence of the $1/r^3$ dipole-dipole interaction [6]. At low electric field, $d < 0.1$ D, there is no significant modification of the loss rate compared to zero electric field, but for higher electric fields we observe a rapidly increasing loss rate, which is more than 40 times larger at 0.2 D than at 0.1 D. We fit the data to a power law dependance, $\beta/T_0 \propto d^p$, and obtain p=6.1(8).

This loss rate and its scaling on dipole moment can still be understood with the simple QT model, but the simple picture of single partial wave ultracold scattering breaks down when an electric field is applied to a polar molecule. A DC electric field breaks the rotational symmetry of the molecule and mixes rotational states of opposite parity to align the molecule's internuclear axis along the external electric field. The aligned molecules now experience a dipole-dipole interaction, which is a long-range interaction falling off as $1/r^3$. As is true for any long-range interaction, the dipole-dipole interaction will mix partial waves. For example, the lowest adiabatic potential for two identical fermionic KRb molecules colliding in the presence of an electric field with be a mixture of odd partial waves $L = 1, 3, 5....$ Strictly speaking with multiple partial waves mixed together,

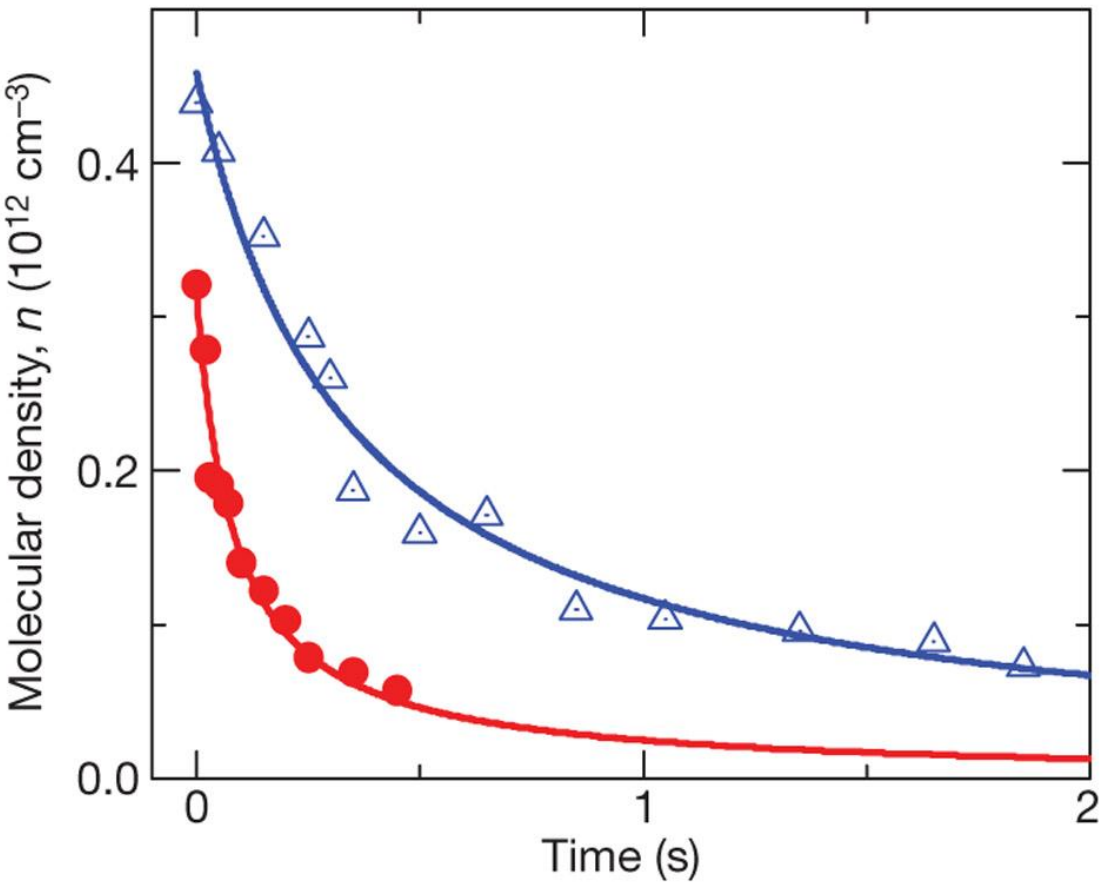

Figure 3.3: Molecular density decay vs. time for induced dipole moments of $d = 0.08$ D (open triangles) and $d = 0.19$ D (filled circles) at $T_0 = 300$ nK. Figure reproduced from reference [2].

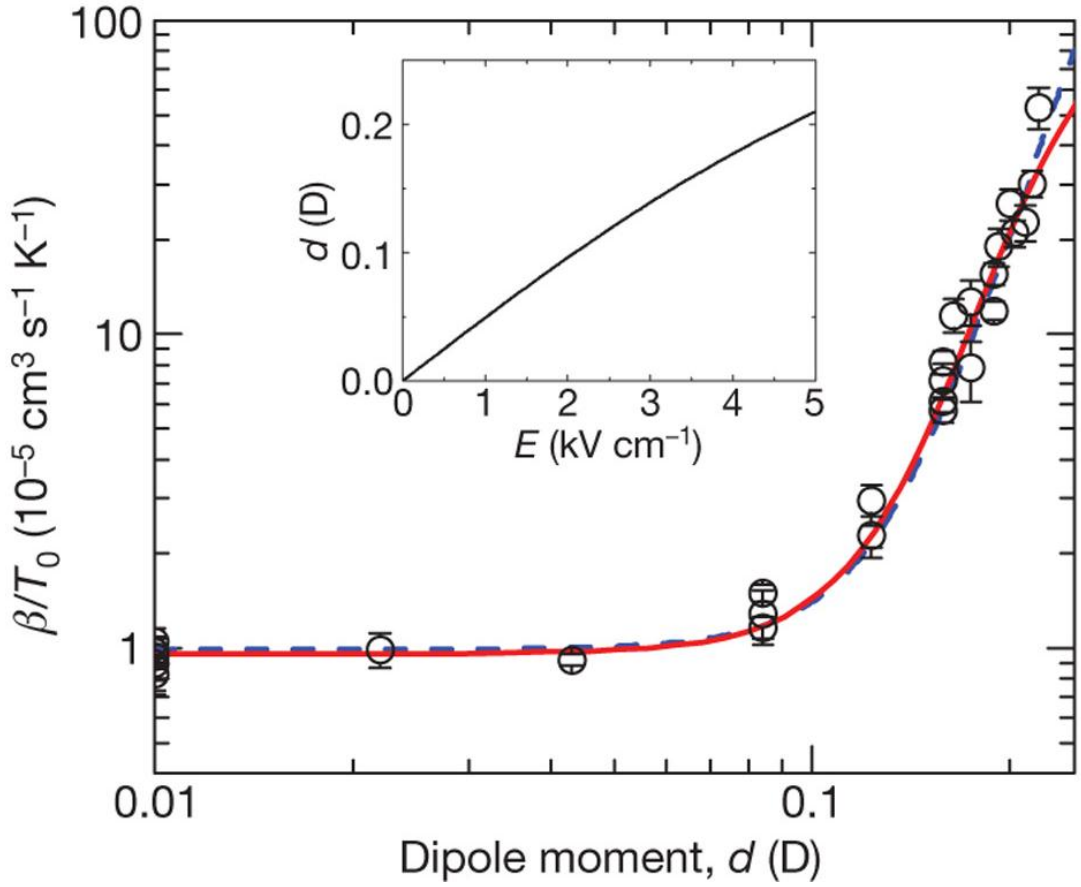

Figure 3.4: Rate coefficient β/T_0 vs. induced dipole moment, d. The dashed line shows a fit to the simple model based on the quantum threshold behavior for tunnelling through a dipolar-interaction modified p-wave barrier. The solid line shows a result of a more complete quantum scattering calculation. Inset, the calculated dependence of d on the applied electric field E. Figure reproduced from reference [2].

our molecules are no longer ultracold, in the sense that they no longer collide in only the lowest allowed partial wave, but they do collide via a single adiabatic potential curve which asymptotically connects to the lowest allowed partial wave at long-range.

In addition to being long-range, the dipole-dipole interaction is also anisotropic, and breaks the degeneracy between the different projections of the $L = 1$ partial wave. This is simply understood by the fact that two dipoles colliding in a head-to-tail orientation (an $m_L = 0$ collision) will have an attractive interaction, while two dipoles colliding in a side-by-side orientation (an $m_L = \pm 1$ collision) will have a repulsive interaction. The head-to-tail attractive interaction effectively lowers the p-wave barrier, while a side-by-side repulsive interaction effectively increases the height of the p-wave barrier. This is schematically shown in figure 3.5.

More quantitatively, the long-range potential in equation 3.7 is modified by the dipole-dipole interaction and becomes

$$\langle LM_L|V(R)|L'M'_L\rangle = \left[\frac{\hbar^2 L(L+1)}{2\mu R^2} - \frac{C_6}{R^6}\right]\delta_{L,L'}\delta_{M_L,M'_L} - \frac{C_3(L,L';M_L)}{R^3}\delta M_L, M'_L \tag{3.10}$$

The $-C_3/R^3$ term is usually written as the classical dipole-dipole interaction $V_{dd}(R,\theta) = d^2(1 - 3\cos^2(\theta)/(4\pi\epsilon_0 R^3)$, but it is often useful to write it in the partial wave basis set, where C_3 is given by

$$C_3(L,L';M_L) = 2(-1)^{m_L}\sqrt{2L+1}\sqrt{2L'+1}\begin{pmatrix} L & 2 & L' \\ 0 & 0 & 0 \end{pmatrix} \times \begin{pmatrix} L & 2 & L' \\ -M_L & 0 & M_L \end{pmatrix}\frac{d^2}{4\pi\epsilon_0}. \tag{3.11}$$

The large brackets denote the $3-j$ coefficients. Notice that in an electric field the interaction potential matrix is no longer diagonal. The long-range dipole-dipole interaction mixes different L levels while preserves M_L, the projection of angular momentum on the quantization axis, so M_L is still a good quantum number. For small dipole moments (small electric fields), we can neglect these couplings and make a diabatic approximation by using only the diagonal elements of the matrix, and ignoring the off-diagonal couplings between different values of L. With this approximation, we can solve for the height of the now modified centrifugal barrier as we did in section 3.2. In figure 3.6, we show the barrier height for M_0 and $M_L = \pm 1$ for both the simple diabatic approximation

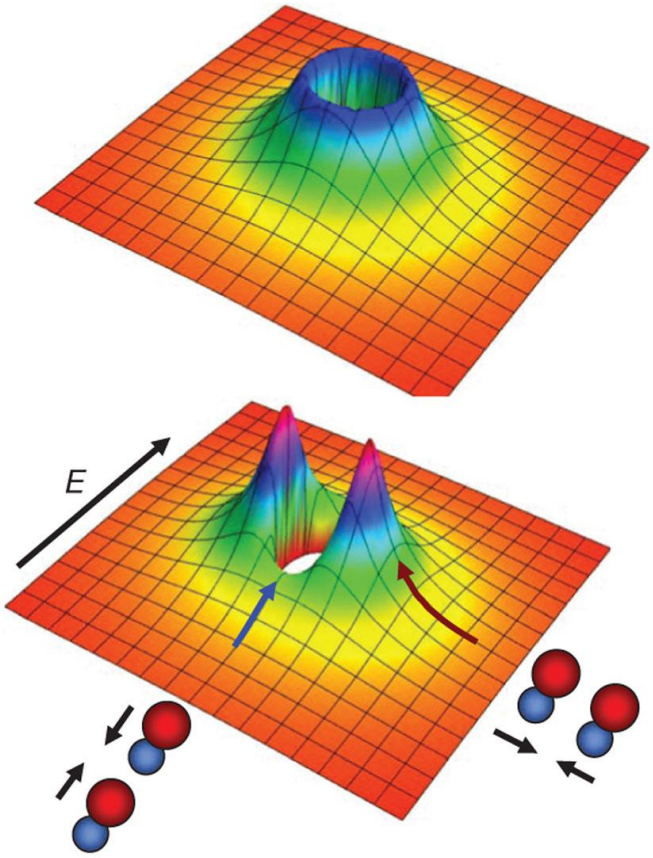

Figure 3.5: Schematic showing the effective intermolecular potential for fermionic molecules at zero electric field. At intermediate intermolecular separation, two colliding molecules are repelled by a large centrifugal barrier for p-wave collisions. For a relatively small applied electric field the spatially anisotropic dipolar interactions reduce the barrier for "head-to-tail" collisions and increase the barrier for "side-by-side" collision. Figure reproduced from reference [2].

(dashed lines) along with the adiabatic solution (solid lines), where the off-diagonal coupling terms were included and the interaction matrix was diagonalized using five partial waves $L = 1, 3, 5, 7, 9$. Although the diabatic approximation works reasonably well for the $M_L = 0$ partial wave, the effect of the couplings can be seen quite dramatically for $d > 0.15$ D where couplings with higher partial waves reduce the adiabatic barrier as the dipole increases.

Although we can use the height of the adiabatic barrier (shown in figure 3.6) in equation 3.6 to get the inelastic rate coefficient, we would like to have an intuitive sense of how these barriers and chemical reaction rates scale with induced dipole moment. For zero electric field, we were able to get an analytic expression for the barrier height, but in the presence of an electric field the addition of the dipole-dipole interaction, which can be either attractive or repulsive, makes this more difficult. We can however look in the two limits of both weak and strong dipole dipole interactions.

For small dipole moments, the centrifugal barrier and van der Waals interaction dominate and we can recover the zero-electric field limit derived above by setting $C_3 = 0$. For large dipole moments, the dipole-dipole interaction dominates and we ignore either the repulsive centrifugal barrier if C_3 is negative (corresponding to a repulsive "side-by-side" dipole-dipole interaction), or we ignore the attractive van der Waals interaction if C_3 is positive (corresponding to an attractive "head-to-tail" dipole-dipole interaction). For positive C_3 coefficients (as for the $M_L = 0$ partial wave), the long-range potential is a balance between the repulsive centrifugal barrier and the attractive dipole-dipole interaction. The height of the barrier is given by

$$V_b = \frac{[\hbar^2 L(L+1)]^3}{54\mu^3 C_3^2} \propto d^{-4}. \tag{3.12}$$

Plugging this barrier height into equation 3.6, we get

$$\beta^{in}_{L=1,M_L=0} = \frac{3\pi}{4}\left(\frac{6^9\mu^6}{5^6\hbar^{14}}\right)^{1/2}\left(\frac{d^2}{4\pi\epsilon_0}\right)^3 k_B T. \tag{3.13}$$

We see that for the $M_L = 0$ at large dipole moment ($d > 0.1D$), the inelastic loss rate increases as d^6, consistent with the measured power law in figure 3.4.

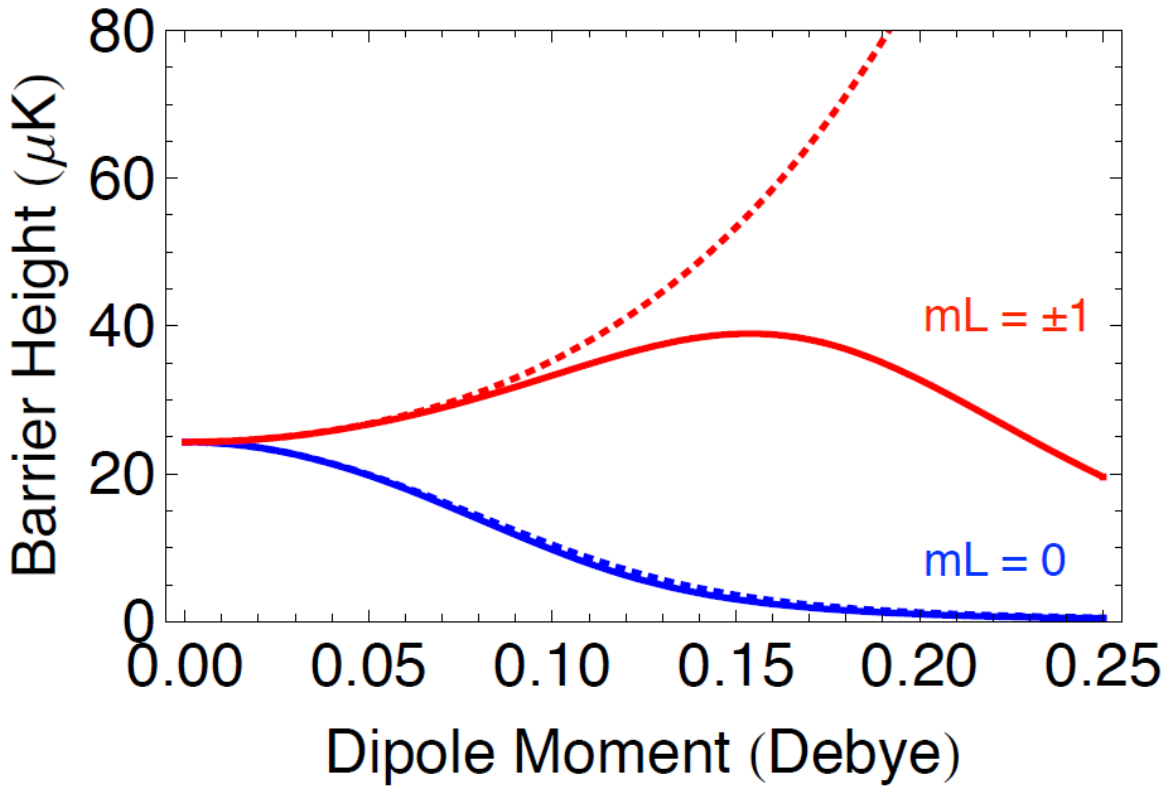

Figure 3.6: Barrier height vs. effective dipole moment, d. The solid lines are calculated using the adiabatic energies considering partial wave mixing up to $L = 9$. The $m_L = \pm 1$ barrier heights rise as the effective dipole moment increases. However, when $d > 0.15D$, the barrier height reduces due to mixing of higher partial waves. The $m_L = 0$ barrier height reduces as the dipole moment increases. The dashed lines are the diabatic curves without partial wave mixing. Figure reproduced from reference [2].

If C_3 is negative (the $M_L = \pm 1$ partial waves) then the long-range potential is a balance between the repulsive dipole potential and the attractive van der Waals potential. Here the height of the barrier is

$$V_b = \frac{|C_3|^2}{4C_6} \propto d^4, \tag{3.14}$$

which again is put into equation 3.6 to obtain the loss rate

$$\beta^{in}_{L=1,M_L=\pm 1} = \frac{3\pi}{4}\left(\frac{50\hbar^4/3C_6}{\mu}\right)^{3/2}\left(\frac{d^2}{4\pi\epsilon_0}\right)^{-3} k_B T. \tag{3.15}$$

Unfortunately, the analytic equation for $L = 1, M_L = \pm 1$ only holds true when the repulsive dipole-dipole interaction is much larger than the centerfugal barrier, which for KRb requires $d > 0.186$ D, but at this large dipole moment the diabatic approximation breaks down and couplings to higher partial waves become important, and start to reduce the barrier height such that the p-wave barrier again becomes significant. Eqn. 3.15 does however confirm our "hand waving" picture that head-to-tail collisions reduce the barrier height and lead to faster loss, while side-to-side collisions increase the barrier height leading to a reduced loss rate.

In a three dimensional trap, the molecules experience both $M_L = 0$ and $M_L = \pm 1$ collisions, but at large dipole moment the loss rate is completely dominated by the $M_L = 0$ channel. Although the derivation above was for the diabatic potential where couplings to higher partial waves were neglected, we can include them now with a simple scaling factor. For $d > 0.1$ D, it can be shown that the coupling with $L = 3$, $M_L = 0$ lowers the diabatic barrier of $L = 1$, $M_L = 0$ by a factor of 0.76, yielding a correction of $0.76^{-3/2} = 1.51$ for $\beta^{in}_{L=1,M_L=0}$ [53].

Although we only have the rates in analytic form in the limits of no electric field and high electric field, we see good agreement with the experiment by simply adding the two rates from the two limits together. This gives us the simple equation

$$\beta^{in}_{L=1} = \frac{\pi}{4}\left[p_1\left(\frac{3^{17}\mu^3 C_6^3}{\hbar^{10}}\right)^{1/4} + 1.51 p_2\left(\frac{2^9 3^{11}\mu^6}{5^6\hbar^{14}}\right)^{1/2} \times \frac{d^6}{(4\pi\epsilon_0)^3}\right] k_B T. \tag{3.16}$$

Here p_1 (p_2) is the loss probability at the height of the barrier for zero (nonzero) electric field. The QT model assumes that $p_1 = p_2 = 1$, but they become fitting parameters for comparison to our

experimental data. By fitting the data in figure 3.4, we obtain $p_1 = 0.7(2)$ and $p_2 = 0.35(8)$. We can alternatively fit a single loss probability p for all values of electric field and a factor b that multiplies the C_6 coefficient. In this parameterization our fit gives $p = 0.35(8)$ and $b = 2.4(9)$. We also compare our data to a more complete quantum scattering calculation. This calculation employs a strong absorptive potential at short range, but captures the long-range physics and uses C_6 as a single fit parameter. This fit also agrees well with the experimental data, and gives $C_6 = 2100 \pm 7000$ a.u. which is consistent with the predicted value of $C_6 = 16130$ a.u.[51].

3.5 Anti-evaporation

In addition to an increased loss rate for increasing d, we observe an increased heating rate for the polar-molecule gas. In figure 3.7, we plot the fractional heating rate normalized by density, $\dot{T}/(T_0^2 n)$, as a function of the induced dipole moment. The heating rate $\dot{T} = c$ is extracted using a linear fit to the temperature of the molecular cloud measured as a function of time over a period sufficiently long to allow T to increase by 20-30%.

This heating rate arises purely from inelastic loss and can be understood as "anti-evaporation", where the collisions preferentially remove particles with lower than average energy and leave the gas with slightly more energy per particle than before the collision. To describe this, we include two competing effects. First, two-body loss preferentially removes molecules from the center of the trap where the density is the highest and the potential energy is lowest, leading to heating. Second, the loss rate due to p-wave collisions scales linearly with temperature, and therefore preferentially removes the particles with large relative kinetic energy, leading to cooling. We model both contributions to determine the rate of heating or cooling. To accommodate the spatial anisotropy of the interaction and the possible anisotropic energy distribution in the trapped gas, we define "temperatures" along three spatial directions using

$$T_i = \frac{E_i}{k_B N}, \tag{3.17}$$

where the index $i = x, y, z$. As the trap shape is a flat disk perpendicular to the vertical (z) axis,

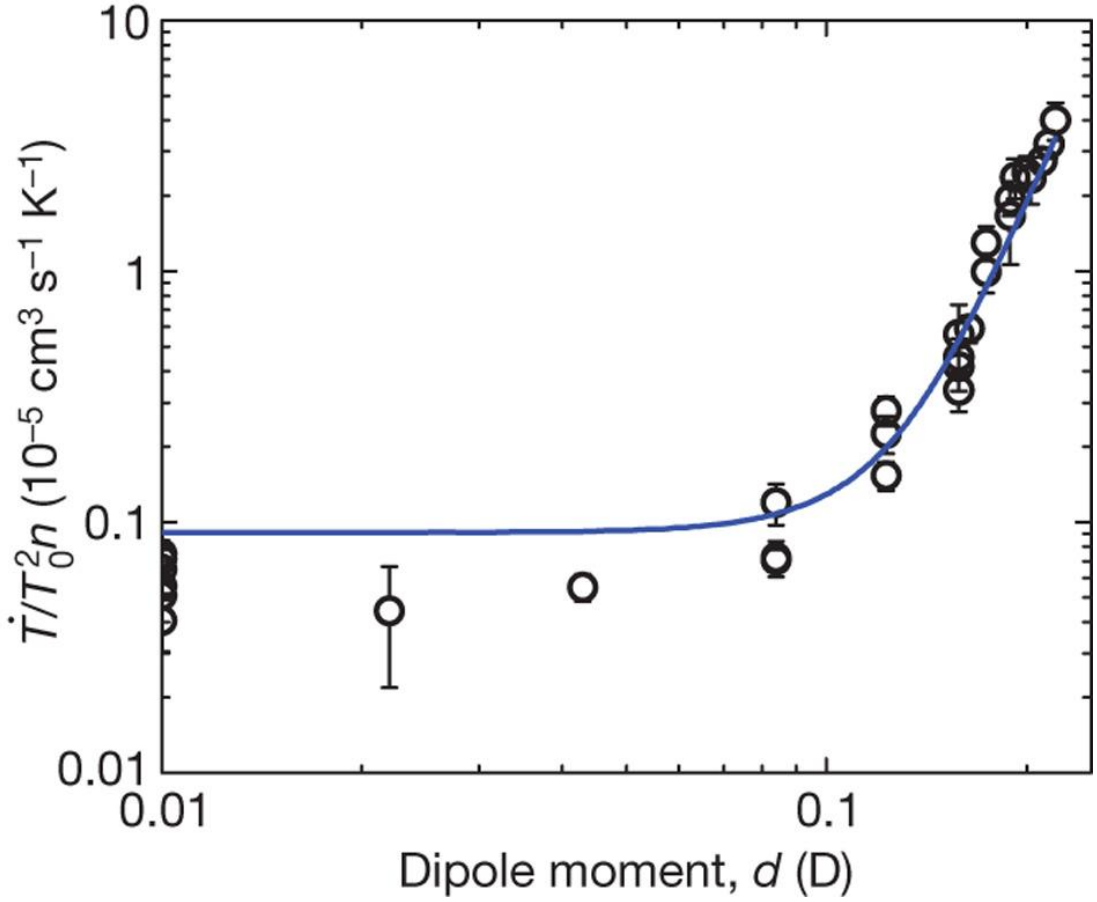

Figure 3.7: Normalized fractional heating rate $\dot{T}/(T_0^2 n)$ as function of dipole moment. The heating rate is extracted using a linear fit to the initial temperature increase and is then normalized by the initial density and temperature of the ensemble. The solid line is the expected heating rate given by $\dot{T}/(T_0^2 n) = (\beta/T_0)/12$. Typical conditions for these data are $n = 0.3 \cdot 10^{12}$ cm^{-3} and $T_0 = 0.5\mu$K s^{-1} at our highest electric fields. Figure reproduced from reference [2].

which is the direction of the electric field, we assume that T_x and T_y are equal. The energies E_i are defined as

$$E_z = \sum(\frac{1}{2}mv_z^2 + \frac{1}{2}m\omega_z z^2) \tag{3.18}$$

$$E_x = \sum(\frac{1}{2}mv_x^2 + \frac{1}{2}m\omega_x x^2), \tag{3.19}$$

where the sum is over all particles. The heating rates are then given by the derivative of Eqn 3.17

$$\frac{dT_i}{dt} = -\frac{T_i}{N}\frac{dN}{dt} + \frac{1}{k_B N}\frac{dE_i}{dt} \tag{3.20}$$

Each two-body inelastic collision removes two particles, so the loss rate is given by

$$\frac{dN}{dt} = -2N\Gamma_{coll}, \tag{3.21}$$

where Γ_{coll} is the inelastic collision rate per particle. Similarly,

$$\frac{dE_i}{dt} = -\Delta E_i N\Gamma_{coll}, \tag{3.22}$$

where ΔE_i is the average E_i for a pair of particles that is lost from the trap. Putting this together, we have

$$\frac{dT_i}{dt} = \left(2T_i - \frac{\Delta E_i}{k_B}\right)\Gamma_{coll}. \tag{3.23}$$

To find the heating caused by inelastic collisional loss, we need to calculate ΔE_z and ΔE_x. To make things easier for ourselves, we consider the energy in center-of-mass and relative coordinates. The total energy of a colliding pair of particles will be the sum of four terms: kinetic and potential energy of the center of mass, and relative kinetic and potential energy. In any of the three directions, the ensemble average for each of the four terms is $1/2k_BT$. However, the average energy for pairs of particles that undergo inelastic collisions is, in general, different from the ensemble average because the collision rate depends on the relative position and relative velocity. Because collisions are only sensitive to relative motion, the kinetic and potential energy of the center-of-mass motion of the two colliding particles will be on average the same as the ensemble average, $(1/2k_BT)$. The relative potential energy is zero for colliding particles (because they must be at the same position to collide).

So even if the loss had no dependence on density or temperature, a colliding pair has only 3/4 of the average energy of a pair of molecules in the gas.

For p-wave inelastic collisions, the collision rate increases linearly with the relative energy of the colliding particles. Furthermore, the spatial anisotropy of the dipole-dipole interaction can result in different rates for $M_L = 0$ and $M_L = \pm 1$ collisions. Therefore, we calculate the heating for $M_L = 0$ and $M_L = \pm 1$ collisions separately and then add the heating rates in the final result. For $M_L = 0$ collisions, we find the average relative kinetic energy for two colliding particles using

$$E^0_{z,rel} = \frac{1}{2}\mu \frac{\int_{-\infty}^{\infty} f(v_z, v_r) v_z^4 dv_z}{\int_{-\infty}^{\infty} f(v_z, v_r) v_z^2 dv_z} \tag{3.24}$$

$$= \frac{3}{2} k_B T_z \tag{3.25}$$

$$E^0_{x,rel} = \frac{1}{4}\mu \frac{\int_0^{\infty} f(v_z, v_r) v_r^2 (2\pi v_r) dv_r}{\int_0^{\infty} f(v_z, v_r) (2\pi v_r) dv_r} \tag{3.26}$$

$$= \frac{1}{2} k_B T_x \tag{3.27}$$

where we assume a Maxwell-Boltzmann distribution of relative velocities given by

$$f(v_z, v_r) \propto \exp -\frac{\mu v_r^2}{2 k_B T_r} \exp -\frac{\mu v_z^2}{2 k_B T_z} \tag{3.28}$$

with $v_r^2 = v_x^2 + v_y^2$. A factor of v_z^2 in both the numerator and denominator of equation 3.24 accounts for the fact that the $M_L = 0$ p-wave inelastic collision rate scales as collision energy $\propto v_z^2$. Similarly, for $M_L = \pm 1$ collisions, the collision rate scales as v_r^2. We find the average relative kinetic energy for two colliding particles using

$$E^1_{z,rel} = \frac{1}{2}\mu \frac{\int_{-\infty}^{\infty} f(v_z, v_r) v_z^2 dv_z}{\int_{-\infty}^{\infty} f(v_z, v_r) dv_z} \tag{3.29}$$

$$= \frac{1}{2} k_B T_z \tag{3.30}$$

$$E^1_{x,rel} = \frac{1}{4}\mu \frac{\int_0^{\infty} f(v_z, v_r) v_r^4 (2\pi v_r) dv_r}{\int_0^{\infty} f(v_z, v_r) v_r^2 (2\pi v_r) dv_r} \tag{3.31}$$

$$= k_B T_x. \tag{3.32}$$

Adding the center of mass energy and putting ΔE_i into the expression for the heating rate (equation 3.23), remembering that $\Gamma_{coll} = \Gamma^0_{coll} + 2\Gamma^{\pm 1}_{coll}$ we find that

$$\frac{dT_z}{dt} = -\frac{1}{2} T_z \Gamma^0_{coll} + T_z \Gamma^{\pm 1}_{coll} \tag{3.33}$$

$$\frac{dT_x}{dt} = +\frac{1}{2}T_x\Gamma^0_{coll} \tag{3.34}$$

Remembering that $\beta = \frac{2\Gamma_{coll}}{n}$ and assuming thermal equilibrium $T = T_z = T_x$ we get an overall heating rate of

$$\frac{dT}{dt} = \frac{1}{3}\frac{dT_z}{dt} + \frac{2}{3}\frac{dT_x}{dt} \tag{3.35}$$

$$= \frac{n}{12}[T_z(2\beta_1 - \beta_0) + 2T_x\beta_0] \tag{3.36}$$

Assuming thermal equilibrium, $T = T_z = T_x$ we get

$$\frac{dT}{dt} = \frac{1}{12}Tn\beta \tag{3.37}$$

or equivalently,

$$\frac{dT}{dt}/(T^2n) = \frac{\beta/T}{12}. \tag{3.38}$$

In figure 3.7, we plot equation 3.38 with no free parameters (solid line) and see that it fits well to our data.

Chapter 4

KRb in 2D

In the previous chapter we showed that atom-exchange chemical reactions cause loss and heating in our gas of $^{40}K^{87}Rb$. We showed that the chemical reaction rate could be changed by either changing the spin polarization of the particles (making them distinguishable or indistinguishable fermions by manipulating the internal states of the molecule) or by introducing a long-range dipole-dipole interaction by applying an external electric field. Unfortunately, either method of changing the chemical reaction rate made the rate increase compared to the rate for spin polarized molecules at zero electric field. Even more discouraging is the fact that the chemical reaction rate is tied to the strength of the dipolar interaction, such that whenever there are strong dipole-dipole interactions (one of the main motivations for creating polar molecules) there is also strong inelastic loss. This can make it difficult to study dipolar interactions in the ultracold gas.

Although the chemical reaction rate increased as the induced dipole moment was increased, it was due to a single adiabatic channel corresponding to "head-to-tail" collisions. In this "head-to-tail" orientation, the dipole-dipole interaction is attractive and effectively lowers the p-wave centrifugal barrier that the molecules have to tunnel through to get to short range where chemical reactions take place. But there are two other collision channels that correspond to "side-by-side" collisions, where the dipole-dipole interaction is repulsive and effectively raises the p-wave centrifugal barrier and lowers the chemical reaction rate. In 3D, all three collision channels take place and the loss is dominated by the "head-to-tail" collisions, but by reducing the dimensionality of the system, we can use Fermi statistics to suppress the "head-to-tail" collisions in much the same way

that Fermi statistics were used to suppress s-wave collisions in 3D.

In this chapter I will show how we can gain control over the orientation of the collision by going to a quasi-2D system. This control over the stereodynamics lets us control the chemical reaction rate. Specifically, we can suppress the $M = 0$ "head-to-tail" collisions, allowing us to create a gas of polar molecule with suppressed inelastic loss (leading to a long lifetime) and strong dipolar interactions. Much of this chapter and its figures will be taken directly from Ref. [3] of which I am an author. This chapter will also necessarily overlap with the thesis of Marcio de Miranda [24] as we worked on these experiments together.

4.1 Controlling chemical reactions

In chapter 3 I showed that in the quantum regime KRb's bimolecular chemical reaction rate could be controlled. This control came about in two ways. First, an electric field could be applied to change the long-range potential. Second, is that the quantum statistics of the molecules dictated a particular symmetry of the total wavefunction with respect to exchange of two molecules. This couples the internal degrees of freedom of the molecules with their motional degrees of freedom, resulting in a strong modification of the collision process through control of internal states. Exploiting this coupling relies on the fact that ultracold collisions, including ultracold chemical reactions, will be dominated by the allowed collision channel with the lowest centrifugal barrier. In three dimensions, ultracold fermions, such as our molecules, that are spin-polarized (in the same internal state) collide in the partial-wave channel with $L = 1$ (p wave), where $\hbar L$ is the quantized relative angular momentum. On the other hand, fermions in different internal states can collide in s waves ($L = 0$). This behaviour is familiar from the example of ultracold fermionic atoms [54]. For the case of dipoles, the dipole-dipole interaction mixes states with different L, such that one should replace $L = 0$ with the lowest-energy adiabatic channel with even L, which does not have a centrifugal barrier. Similarly, $L = 1$ becomes the odd-L adiabatic channel with the lowest centrifugal barrier. The approach of controlling the relative motion through control of the internal molecular states has a serious limitation, which is that we do not have control over the projection

of the relative angular momentum of the colliding particles on the $\hat{z}$ axis, M. This is especially important for dipoles, where M describes whether the dipoles approach 'side-by-side' (for example, $L = 1, M = 1$), and therefore experience a repulsive dipole-dipole interaction, or 'head-to-tail' (for example, $L = 1, M = 0$), where the dipole-dipole interaction is attractive.

By confining polar molecules in a two dimensional plane, we gain control over M. With extremely strong confinement and large dipole moments oriented perpendicular to the 2D plane, one could, in principle, achieve a fully 2D geometry where the molecules could approach each other only side-by-side (odd M) simply because of the repulsive part of the dipole-dipole interaction [55, 56]. Alternatively, in our present experimental situation of quasi-2D trapping, we can again use the overall symmetry of the two-molecule wavefunction for fermionic molecules to control M. In quasi-two dimensions, L is no longer a good quantum number for describing how molecules approach each other at intermolecular separations that are much larger than a_{ho}, where $a_{\mathrm{ho}} = \sqrt{\frac{\hbar}{2m\omega}}$ and is the extent of the molecular cloud in the lowest harmonic oscillator state in $\hat{z}$. In 2D (and quasi-2D) the relative motion is described by M. In addition, we have a new (compared with the 3D case) quantum number that describes the harmonic oscillator motional state in $\hat{z}$ for each molecule. This quantum number, which we label v, acts as a new internal degree of freedom for the molecules as they approach each other in the long range, in the sense that we can relatively easily control the occupation in the different v states and this will in turn give us control over the relative motion described by M. Specifically, fermionic molecules in the same internal state and the same v must collide with odd M, whereas fermions in the same internal state but different v can collide with even M.

4.2 What is 2D?

The spatial geometry of the confining potential can influence collisions in a trapped dipolar gas. This effect has been explored for elastic collisions of magnetic atoms [57]; here, we exploit spatial geometry to control chemical reactions of polar molecules. In particular, a 2D trap geometry, with the dipoles oriented parallel to the tight confinement direction $\hat{z}$, is well matched to the spatial

anisotropy of the dipole-dipole interaction [58]. We can realize such a geometry using a 1D optical lattice (see figure 1a and Chapter 2), where the trapped molecules are divided among several isolated layers. In each of these layers, the lattice potential provides tight harmonic confinement in $\hat{z}$ such that only the lowest few quantized motional states in $\hat{z}$ are occupied. Consequently, within each isolated layer, colliding molecules approach each other in two dimensions. At long intermolecular distances, the molecules do indeed behave as if they are confined in a 2D geometry and collisions are best described in a cylindrical symmetry with quantum numbers M and v. But at shorter intermolecular separations this description breaks down.

The extent of the cloud in the direction of tight confinement (given by the harmonic oscillator length a_{ho}) is larger than both the van der Waals length and the dipole length. At these small intermolecular separations the collisions are still best described in 3D with quantum numbers L and M_L. Put another way, just as the cylindric symmetry and tight harmonic confinement in $\hat{z}$ makes L a bad quantum number at large intermolecular separations, the spherical symmetry of the van der Waals potential makes v a bad quantum number at shorter intermolecular separations. The energies involved in the collision around the p-wave barrier are large enough to mix many v levels together.

Because collisions can be treated in 2D at large intermolecular separation, R, but are 3D at small R, our system is quasi-2D. But the molecules are oblivious to our need to change from cylindrical to spherical coordinates midway through a collision. In both regions, M is a good quantum number that is strictly conserved for all R. So, molecules that start in an adiabatic potential curve at long range with $M = 0$ will smoothly connect to a potential curve at short range that is $M_L = 0$. In this sense, it does not matter that the system are quasi-2D, just being 2D at long-range is good enough to select out a single M state. Moreover, being 2D at long range also provides us with an easily controlled quantum number v that allows us to control the symmetry of the wavefunction which chooses the orientation of the collision.

I will note here that although we rely on the quantum statistics of our fermionic molecules to provide a "statistical suppression" of collisions that arises from the centrifugal repulsion of

indistinguishable fermions, suppression that relies directly on a strong confining potential and a repulsive dipole-dipole interactions can also be realized, but it requires both tighter harmonic confinement and larger dipole moments [55, 56]. Although this regime is currently unreachable for our experimental apparatus, the required lattice strengths and dipole moments are not entirely unreasonable, and this suppression has the advantage of not relying on quantum statistics, which should allow it to work for bosons, fermions, and even distinguishable particles.

4.3 Stereodynamics and quantized collisions

We now consider the quantized collision channels that define the stereodynamics in this quasi-2D geometry. We identify three relevant collision channels, and we label these $|1\rangle$, $|2\rangle$, and $|3\rangle$, in order of increasing centrifugal barrier heights. Figure 4.1b shows schematically the adiabatic potentials for these three lowest-energy collision channels. Collision channel $|1\rangle$ corresponds to spatially isotropic collisions, collision channel $|2\rangle$ is the quantum analogue of 'head-to-tail' collisions, and collision channel $|3\rangle$ is the quantum analogue of 'side-by-side' collisions.

Channels $|1\rangle$ and $|2\rangle$ become increasingly favourable for chemical reactions as the dipole-dipole interaction strength is increased, for example by increasing the external electric field $|\overrightarrow{E}|$. In contrast, channel $|3\rangle$ has a centrifugal barrier whose height increases for higher dipole moment, within the $|\overrightarrow{E}|$ range considered in this work. This barrier hence continues to prevent molecules from reaching short range.

The low-energy collision channels $|1\rangle$ $|2\rangle$, and $|3\rangle$ can be labelled with four relevant quantum numbers, η, L, γ and M. The quantum number γ identifies the exchange symmetry of the part of the two-molecule wavefunction that describes the relative motion in $\hat{z}$; for the symmetric case, $\gamma = 1$ and for the antisymmetric case, $\gamma = -1$. For two molecules in the same $\hat{z}$ harmonic oscillator state, $\gamma = 1$, whereas both $\gamma = 1$ and $\gamma = -1$ are possible for two molecules in different harmonic oscillator states. Similarly, we use a quantum number η to keep track of the exchange symmetry of the part of the wavefunction that describes the internal states of the two molecules. For two molecules in the same internal quantum state, $\eta = 1$ whereas $\eta = \pm 1$ for molecules in different

internal states. In two dimensions, three quantum numbers (M, γ, η) are sufficient to describe the quantum stereodynamics. However, because the interactions at short range must be described in three dimensions, the quantum number corresponding to the 3D angular momentum, L, as well as M becomes relevant. With collisional channels described by quantum numbers η, L, γ, and M, the fermionic symmetry can be concisely stated in the following relations:

$$\begin{aligned} \eta(-1)^L &= -1 \text{ short range, 3D} \\ \eta\gamma(-1)^M &= -1 \text{ long range, 2D} \end{aligned} \tag{4.1}$$

Each of the collision channels satisfies both the short-range and long-range symmetry requirements in Eqn. 4.1. Figure 4.1c shows how these different collision channels can be accessed through control of the internal molecular states and the $\hat{z}$ motional states. In figure 4.1c, molecules in different internal states are shown in different colours and the harmonic oscillator states in $\hat{z}$ are labelled by v. In case (1) for two molecules in different internal molecular states and in any combination of v levels, $\eta = -1$ allowing for $L = 0$ barrierless collisions in channel $|1\rangle$. In case (2), the molecules are prepared in identical molecular states (so $\eta = 1$), but in different v levels so the lowest-energy collision channel vibration state is $|2\rangle$ with $\gamma = -1$. At short-range there is a $L = 1$ p-wave barrier, but to fulfill the symmetry requirements at long-range $M = 0$, which is a "head-to-tail collision" where the barrier height decreases as the dipole moment is increased. In case (3) where the molecules are prepared in the same internal state and the same v level, $\eta = 1$ and $\gamma = 1$, so at short range $L = 1$ and at long range $M = \pm 1$. This provides a p-wave barrier with "side-by-side" dipolar collisions where the barrier height increases as the dipole moment increases. This case is the least favorable for bimolecular chemical reaction, and should allow for the creation of a gas that has strong dipole-dipole interactions without fast loss from chemical reactions.

4.4 Preparation of the 2D molecular system

For the set of experiments described in this chapter, we start with a mixture of ^{40}K and ^{87}Rb in a crossed-beam optical dipole trap, with a harmonic trapping frequency of 180 Hz along

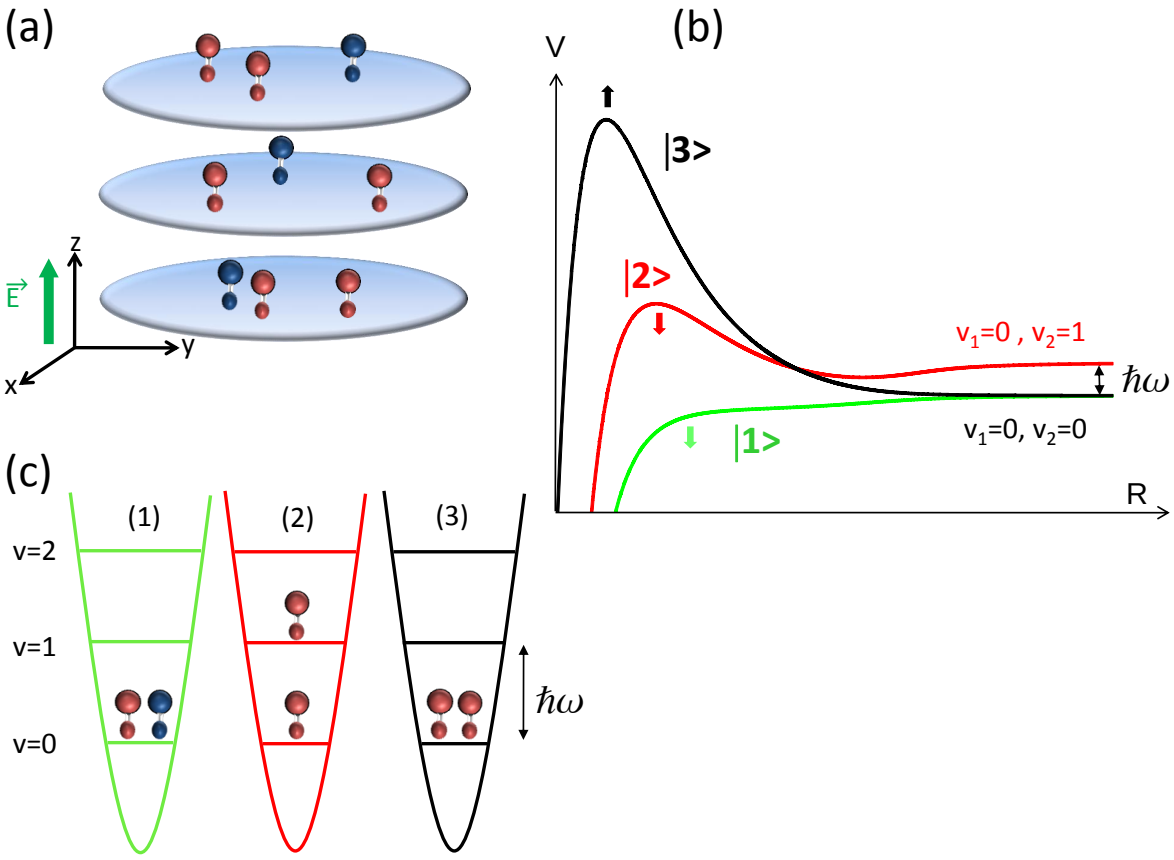

Figure 4.1: (a) A quasi-2D geometry for collisions is realized for polar molecules confined in a 1D optical lattice. An external electric field is applied along the tight confinement axis. (b) Schematic showing the three lowest adiabatic potentials for collisions as a function of the intermolecular separation, R. These three channels are ordered with increasing magnitude of the centrifugal barrier. The arrows indicate the change in the potential for an increasing external electric field, and hence a growing induced dipole moment. (c) Schematic showing each individual case for the three lowest collision channels. The lowest-energy collision channel occurs when two molecules are prepared in different internal states (indicated here by the colors of the molecules). The second channel is realized when two identical molecules are prepared in different vibrational levels v for their $\hat{z}$ motions. The third case as a much reduced loss rate as a consequence of an increased centrifugal barrier when the two identical molecules are prepared in the same vibrational level along $\hat{z}$. Figure reproduced from reference [3].

the vertical direction $\hat{z}$ and 25 Hz in the transverse directions. We add an optical lattice along $\hat{z}$, which is formed by a retro-reflected beam with a $1/e^2$ waist of 250 μm and a wavelength of 1064 nm. Both optical dipole trap beams and the optical lattice beam are linearly polarized and their polarizations are mutually orthogonal. Each layer of the optical lattice trap is tightly confining in $\hat{z}$ with a harmonic trapping frequency of $\nu_z = 23$ kHz for the molecules, whereas in the transverse directions, the combined trap has a harmonic trapping frequency of 36 Hz. The tunnelling rate between lattice layers is negligible and, therefore, each layer realizes an isolated trap for the molecules. Initially, 34,000 ground-state molecules are confined in roughly 23 layers, with the center layer having 2,200 molecules and a peak density of 3.4×10^7 cm^2.

We start by loading ultracold ^{40}K and ^{87} Rb atoms from the crossed-beam dipole trap into the combined trap by turning up the intensity of the optical lattice beam in 150 ms. We then create molecules in the lattice by first forming extremely weakly bound molecules through magneto-association of atom pairs and then coherently transferring these molecules into their rovibrational ground state using optical transitions [19]. The temperature of the molecular gas, T, in the combined optical dipole plus lattice trap can be varied between 500 and 800 nK by varying the initial atom gas conditions.

To completely freeze out the motion of the molecules along $\hat{z}$ requires that $k_BT/h\nu_z$. For a gas at $T = 800$ nK in our lattice, $k_BT = h\nu_z = 0.72$ and we expect 25% of the molecules will occupy higher v levels. As discussed above, to control the stereochemistry of bimolecular reactions in the ultracold gas, we need to control both the internal state and the harmonic oscillator level, v, of the molecules. We create the molecules in a single internal quantum state. If desired, we can subsequently create a 50/50 mixture of molecules in the ground and the first excited rotational states by applying a resonant microwave $\pi/2$-pulse [20]. The occupation of lattice levels v can be controlled by varying T; alternatively, we can prepare a non-thermal distribution of molecules using parametric heating (for details see section 2.6). Here, the lattice intensity is modulated at twice ν_z, and, as a result, molecules initially in the $v = 0$ level are excited to the $v = 2$ level, as discussed in chapter 2.

We determine the population in each lattice level using an adiabatic band-mapping technique [43, 44] described in section 2.7. As the lattice potential is ramped down slowly (compared to h/E_{bg} where E_{bg} the band gap), the quasimomentum in the lattice is mapped into real momentum, and molecules in different vibrational levels of the lattice are mapped onto Brillouin zones. The measured molecule momentum distribution following this ramp is shown in figure 4.2a for a $T = 800$ nK molecular gas. The measured fraction in $v = 0$ matches well with the expected thermal distribution. In contrast, figure 4.2b shows the measured non-equilibrium occupation of lattice vibrational levels following parametric heating.

4.5 Measurement of the molecular loss rate

We measure the bimolecular reaction rate by monitoring the loss of trapped molecules as a function of time. To image the molecules, we reverse our coherent transfer process to bring the molecules back to a weakly bound state where we can detect the molecules with time-of-flight absorption imaging [19]. The molecules are imaged after free expansion from the combined optical dipole plus lattice trap. From the images, we obtain the total number of molecules and the radial cloud size.

As we do not resolve the individual layers of the optical lattice, we obtain an average 2D density per layer by dividing the total number by the cross-sectional area of the cloud, and by an effective number of layers ξ. To determine ξ, we assume that as we load the optical lattice the extent of the cloud in the $\hat{z}$ direction does not change, but the cloud is simply sliced into pancakes. This is a reasonable assumption because the lattice provides no additional harmonic confinement in the $\hat{z}$ direction. To measure the in-trap distribution we first load the lattice with atoms, create molecules, transfer to the ground state, remove the residual atoms, and then load the molecules back into the optical trap by ramping down the optical lattice with a 10 ms linear ramp. We hold the molecules in the optical trap for 20 ms and then measure the size of the cloud in time of flight. Although the cloud size in the $\hat{z}$ direction is below our imaging resolution, we can extract the in-trap size by measuring the temperature and trap frequency. In this manner we are able to

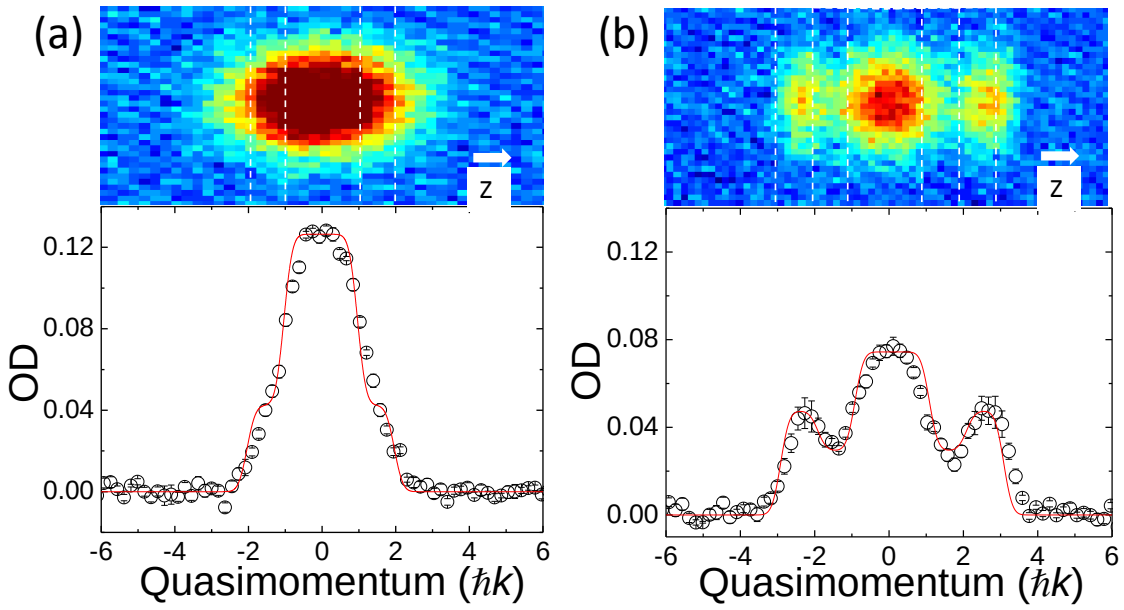

Figure 4.2: We measure the relative population in each lattice vibrational level using a band-mapping technique. The results for the initial distribution of molecules (a) and for a non-thermal distribution created by parametric heating in $\hat{z}$ (b). The two images use the same colour scale for the optical depth (OD). The images are an average of five shots (a) and seven shots (b), taken after 10 ms of free expansion. Below each image we show a trace along $\hat{z}$ that corresponds to the OD averaged over the transverse direction. A fit (red line) to the trace, which takes into account both the size of the Brillouin zones and our imaging resolution, is used to extract the relative populations, n_v/n_{tot}, in each lattice level v. The horizontal axis corresponds to momentum in $\hat{z}$ and is marked in units of the lattice momentum $\hbar k$, where k is the lattice wave vector. Figure reproduced from reference [3].

measure the $1/e^2$ gaussian radius of the cloud in-trap (σ_z). For a typical cloud we measure $\sigma_z = 3.8$ μm.

On a single pancake the density-weighted density, n, is given by $N_i/(4\pi\sigma_r^2)$, where N_i is the number of molecules on the ith lattice site and σ_r is the size of the cloud in the radial direction. We also know that on a single pancake the molecules chemically react following $\frac{dn(t)}{dt} = -\beta n(t)^2$. Integrating over $\hat{x}$ and $\hat{y}$ and summing over the different layers in $\hat{z}$ we get

$$\dot{N}_{\text{total}}(t) = -\frac{\beta}{4\pi\sigma_r^2}\sum_{i=-\infty}^{\infty} N_i(t)^2 \tag{4.2}$$

$$= -\frac{\beta N_{\text{total}}(t)^2}{4\pi\sigma_r^2}\sum_{i=-\infty}^{\infty}\left(\frac{N_i(t)}{N_{\text{total}}}\right)^2 \tag{4.3}$$

where $\frac{N_i(t)}{N_{\text{total}}}$ is the percentage of molecules in the ith pancake and $\sum_{i=-\infty}^{\infty}\left(\frac{N_i(t)}{N_{\text{total}}}\right)^2 = 1/\xi(t)$, the effective number of layers in our system. We can rewrite Eqn. 4.3 in the more familiar form of the two-body loss equation

$$\dot{n_{\text{2D}}} = -\beta n_{\text{2D}}^2 \tag{4.4}$$

where $n_{\text{2D}} = N_{\text{total}}/(4\pi\sigma_r^2\xi)$ is the average 2D density of the system and N_{total}/ξ is the number-weighted average N_i, averaged over the occupied layers. This result relies on the assumption that ξ is time independent, which is not correct. For the conditions used in this experiment $\xi_{\text{initial}} = 23$, but the loss is density dependent so the layers at the center of the cloud, with high density, will decay faster than the layers on the edge of the cloud, with low density. ξ increases for longer time as the initial gaussian distribution across the layers become much flatter as illustrated in figure 4.3. For our analysis we use a time averaged value $\xi = 30$ that was determined by comparing an analysis based on a uniform layer density with a numerical simulation of the loss in each layer, shown in figure 4.4.

In figure 4.5, we show the average 2D density as a function of time. For these data, the molecules are all prepared in the same internal state and $|\overrightarrow{E}|$ is 4 kV/cm, which gives an induced molecular dipole moment in the laboratory frame of 0.158 Debye. The two data sets in figure 4.5 correspond to an unperturbed $T = 800$ nK gas (black squares) and a parametrically heated gas

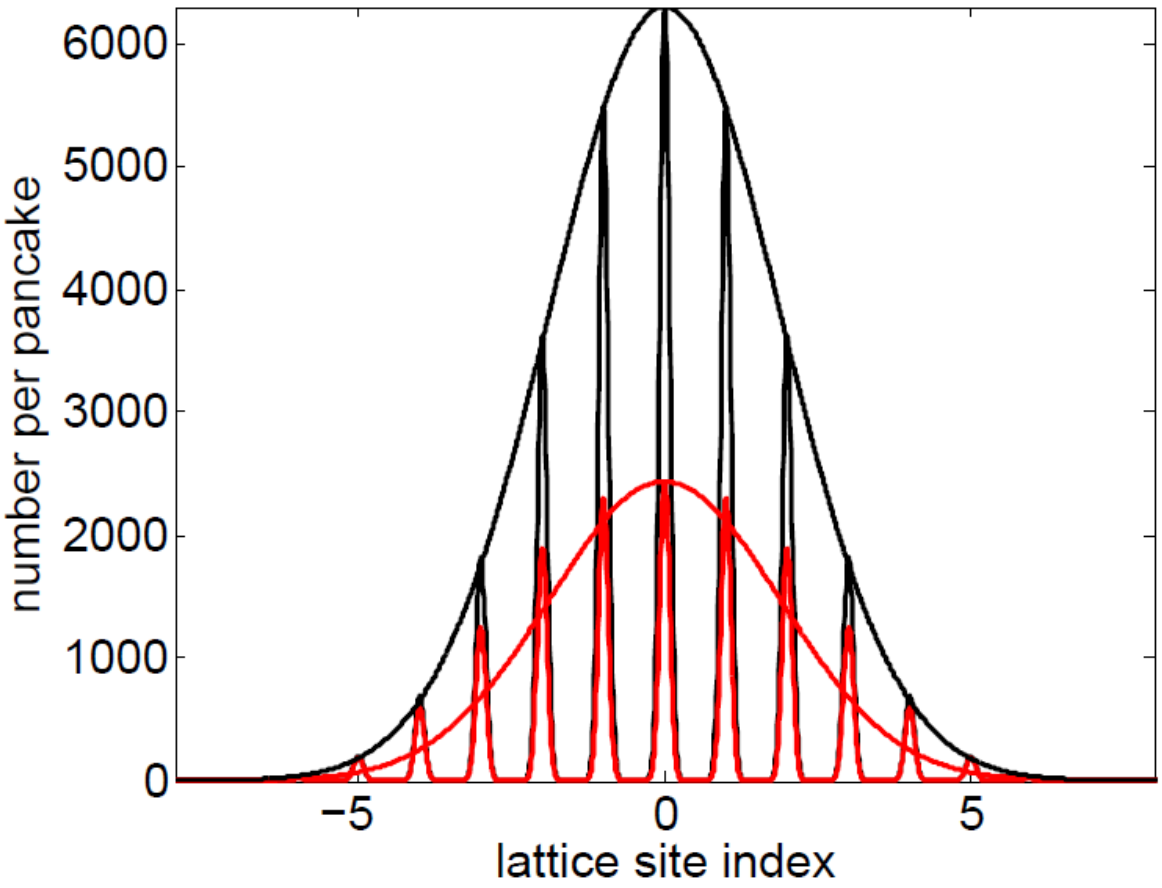

Figure 4.3: The molecule distribution in the $\hat{z}$ direction. Initially the molecule distribution follows a gaussian distribution (black), but after 500 ms (red) the most dense pancakes at the center of the cloud have decayed the most resulting in a distribution much flatter than the initial gaussian.

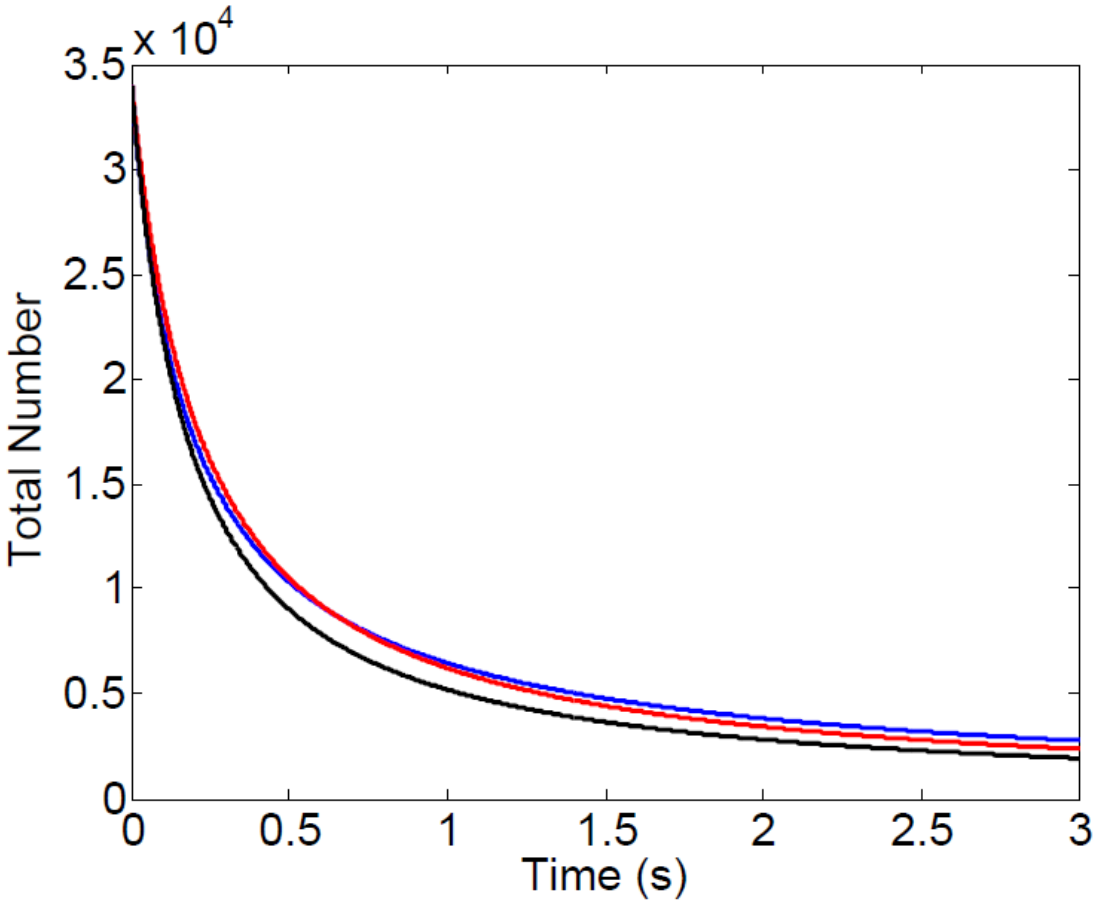

Figure 4.4: The calculated number loss due to two-body decay in a one-dimensional optical lattice. The exact numerical solution solving for the time dependent density in each pancake and then summing over all pancakes to find the total number is shown in blue. If we use the initial number of layers, ξ_{initial}, to scale the total number we overestimate the loss (black curve). In the red curve we use ξ as a fit parameter to find the time averaged value of $\xi = 30$.

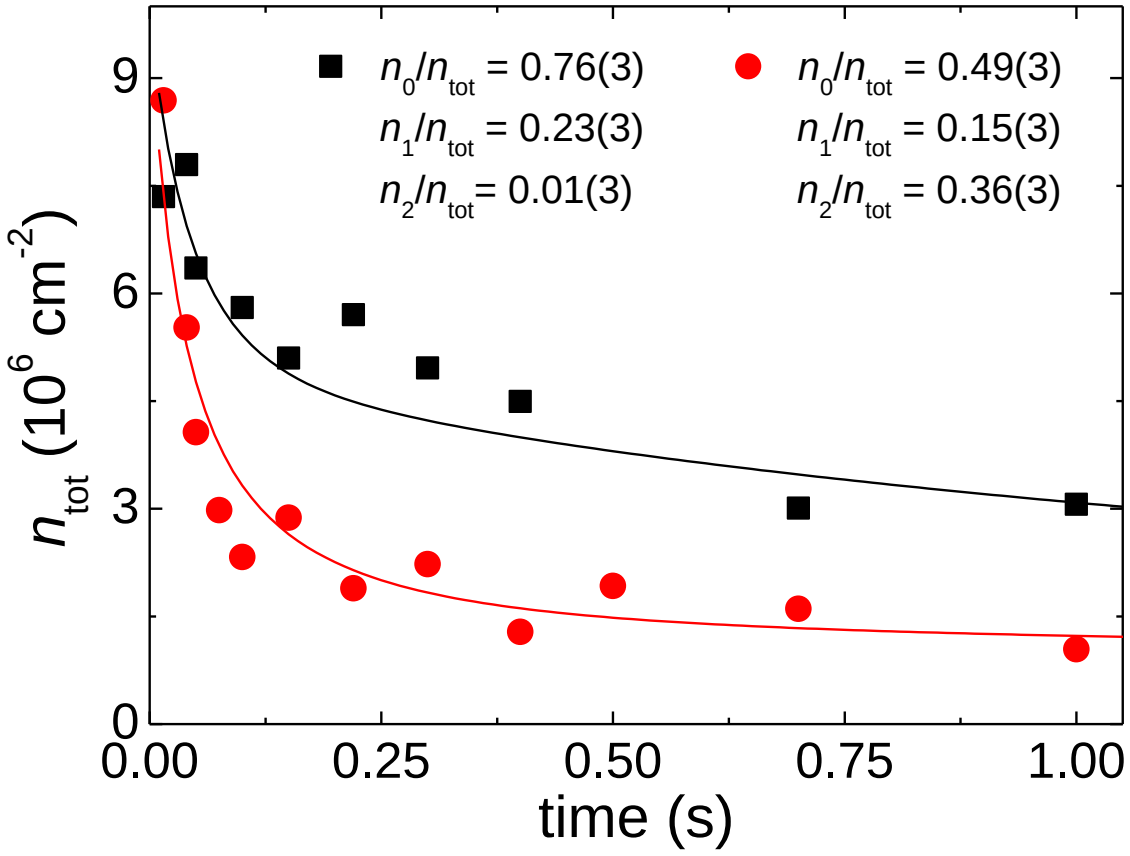

Figure 4.5: Measurement of 2D loss rates. A fit (solid lines) to the measured loss curves, with (red circles) and without (black squares) 0.3ms of parametric heating in $\hat{z}$, is used to extract the loss-rate coefficients $\beta_{|3\rangle}$ and $\beta_{|2\rangle}$. Figure reproduced from reference [3].

(red circles). For the case where parametric heating was used to increase population in $v > 0$ levels, the data show a faster initial loss of molecules. This indicates that the initial loss is predominately due to interlevel collisions as described in case (2) of figure 4.1c, whereas intralevel collisions (case (3) of figure 4.1c) give a slower loss of molecules at longer times. It should be pointed out here that because of the separation of timescales between intralevel and interlevel loss, the system is self purifying, meaning that if the gas is initially prepared with a small fraction in excited v states the fast interlevel loss will quickly get rid of these molecules and leave a gas entirely in a single band harmonic oscillator state. However, this self purification is not without a cost, every unwanted molecule in a higher v state will react with a molecule in the ground v state, and thus reduce the number and density of the molecules in the ground state.

We fit the data using a simple model, which assumes two loss-rate constants: one for interlevel collisions, $\beta_{|2\rangle}$, and a second one for intralevel collisions, $\beta_{|3\rangle}$ (with the subscripts referring to the adiabatic channels labelled in figure 4.1b). Here,

$$\begin{aligned} \frac{dn_0}{dt} &= -\beta_{|3\rangle} n_0^2 - \beta_{|2\rangle} n_0 n_1 - \beta_{|2\rangle} n_0 n_2 \\ \frac{dn_1}{dt} &= -\beta_{|2\rangle} n_0 n_1 - \beta_{|3\rangle} n_1^2 - \beta_{|2\rangle} n_1 n_2 \\ \frac{dn_2}{dt} &= -\beta_{|2\rangle} n_0 n_2 - \beta_{|2\rangle} n_1 n_2 - \beta_{|3\rangle} n_2^2 \end{aligned} \tag{4.5}$$

where n_v is the 2D density of molecules in a particular lattice vibrational level v. To fit the measured time dependence of the total 2D density, $n_{\rm tot}(t)$, we use $n_{\rm tot}(t) = n_0(t) + n_1(t) + n_2(t)$. We input the measured initial populations $n_v/n_{\rm tot}$ (see figure 4.2) at $t = 0$, and we fit the data to the numerical solution of Eqn. 4.5. We obtain $\beta_{|2\rangle}$ and $\beta_{|3\rangle}$ from a simultaneous fit to the two measured $n_{tot}(t)$ curves shown in figure 4.5.

By repeating this procedure for different values of $|\vec{E}|$, we measure the chemical reaction rate constants, $\beta_{|2\rangle}$ and $\beta_{|3\rangle}$, as a function of the induced dipole moment. In figure 4.6, we show the intralevel (black squares) and interlevel (red circles) chemical rate constants as a function of the dipole moment. Also shown as green triangles in figure 4.6 are the results of two measurements for a 50/50 mixture of molecules in different rotational states (case (1) of figure 4.1c). The

mixture of distinguishable molecules is achieved with a single $\pi/2$ pulse between $|0,0,-4,1/2\rangle$ and $|1,1,-4,1/2\rangle$ (using the notation $|N,m_N,m_I^K,m_I^{Rb}\rangle$). Although the microwave pulse puts the molecules in a coherent superposition of the two rotational states (where the molecules would still be indistinguishable), we observe that this coherence is lost (making the molecules distinguishable) in less than 1 ms due to the difference in polarizabilities between the two rotational states (see chapter 6). Here, we fit the loss of molecules in the ground rotational state to the solution of $\frac{dn_{\rm tot}}{dt} = -\beta_{|1\rangle} n_{\rm tot}^2$ to extract a single loss-rate constant.

4.6 Comparison to theory

We compare our measurements to quantum scattering calculations performed by Goulven Quéméner and John Bohn using a time-independent quantum formalism based on spherical coordinates with cylindrical asymptotic matching to describe the molecular collisions in quasi-two dimensions [59]. They use an absorbing potential at short distance to represent chemical reactions [53, 52]. This technique showed excellent agreement with previous experimental data for KRb bimolecular reactions in three dimensions (see chapter 3 and Refs. [1, 2]). They computed the loss-rate coefficients β_{v_1,v_2} for molecules in different initial lattice vibrational states v_1, v_2, at a collision energy of 800 nK. When the induced dipole moment is still small (< 0.2 D), the measured temperature is a good approximation for the mean collision energy. The loss rates of the different processes can be separated into fast loss rates $(\beta_{0,1}, \beta_{0,2}, \beta_{1,2}) \approx \beta_{|2\rangle}$ and slow loss rates $(\beta_{0,0}, \beta_{1,1}, \beta_{2,2}) \approx \beta_{|3\rangle}$. The black theoretical curve in figure 4.6 corresponds to an average of the slow rates weighted by the initial populations n_0, n_1, n_2. The red curve corresponds to the same average, but for the fast rates. The green curve corresponds to the loss rate of molecules in different internal states.

The three measured reaction rate constants shown in figure 4.6 are consistent with the quantum scattering calculations for the collision channels shown in matching colors in figure 4.1b,c. Molecules in different rotational states (green triangles in figure 4.6) have the highest rate for chemical reactions, consistent with the fact that they can collide in channel $|1\rangle$, which corresponds

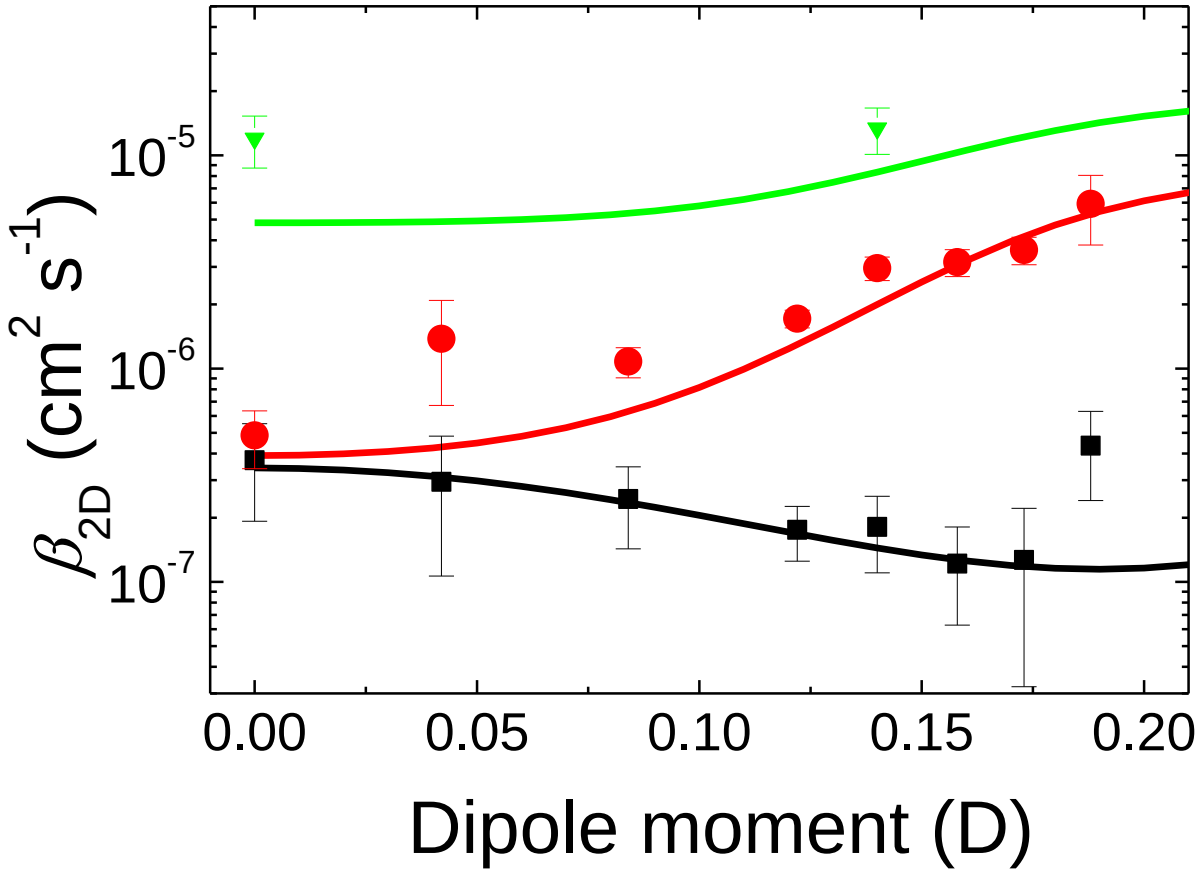

Figure 4.6: The extracted loss-rate coefficient for collisions of molecules in the same lattice vibration level (black squares) and from different lattice vibrational levels (red circles) plotted for several dipole moments. Measured loss-rate coefficients for molecules prepared in different internal states are shown as green triangles. For comparison with each of these three measurements, we include a quantum scattering calculation for $\nu_z = 23$ kHz, $T = 800$ nK (solid lines). The potentials corresponding to the dominant loss channel for the three cases are shown in matching colors in figure 4.1b,c. Figure reproduced from reference [3].

to spatially isotropic collisions with no centrifugal barrier. On the other hand, molecules prepared in the same internal molecular state (red circles and black squares in figure 4.6) have suppressed reaction rates because the lowest-energy collision channel is no longer allowed. Instead, identical molecules in different lattice levels (red circles in figure 3b) react predominantly through collisions in channel $|2\rangle$, or "head-to-tail", whereas identical molecules in the same lattice level (black squares in figure 4.6) react through collisions in channel $|3\rangle$, or "side-by-side". The importance of stereodynamics on the reaction rate for polar molecules is manifest in the very different dipole-moment dependence of the reaction rates in these two collision channels. In particular, for the case where the molecules are prepared both in the same internal quantum state and in the same v level, the reaction rate is suppressed even as the dipole moment is increased.

4.7 2D vs. 3D

Figure 4.7 shows how the initial loss rate in a gas of identical molecules depends on the fractional occupation of the lowest lattice level, $n_0/n_{\rm tot}$. The fractional molecular population $f(v,T)$ in a vibration level v at temperature T is obtained from a Boltzmann distribution, and the effective $\beta_{\rm initial}$ is then calculated as

$$\beta_{\rm initial} = \beta_{|3\rangle} \sum_v f(v,T)^2 + \beta_{|2\rangle} \sum_{v_1 \neq v_2} f(v_1,T) f(v_2,T) \tag{4.6}$$

As $n_0/n_{\rm tot}$ increases, the calculated initial loss-rate constant for a molecular gas in thermal equilibrium (solid black line) changes from close to $\beta_{|2\rangle}$ (the red line indicating the measured value at 0.174 D from figure 4.6) to $\beta_{|3\rangle}$ (open symbol at $n_0/n_{\rm tot} = 1$). On the top axis of figure 4.7, we give the corresponding values of the scaled temperature ($k_B T/h\nu_z$). The filled triangles in figure 4.7 correspond to the measured initial loss rate at different temperatures (500 nK and 800 nK), and the open symbol at $n_0/n_{\rm tot} \approx 0.5$ corresponds to the initial loss rate for the parametrically heated, non-thermal molecular gas.

We also directly compare the suppressed chemical reaction rate in quasi-two dimensions with that of the 3D case in figure 4.8. Here, we compare data for a 3D geometry from chapter 3 against

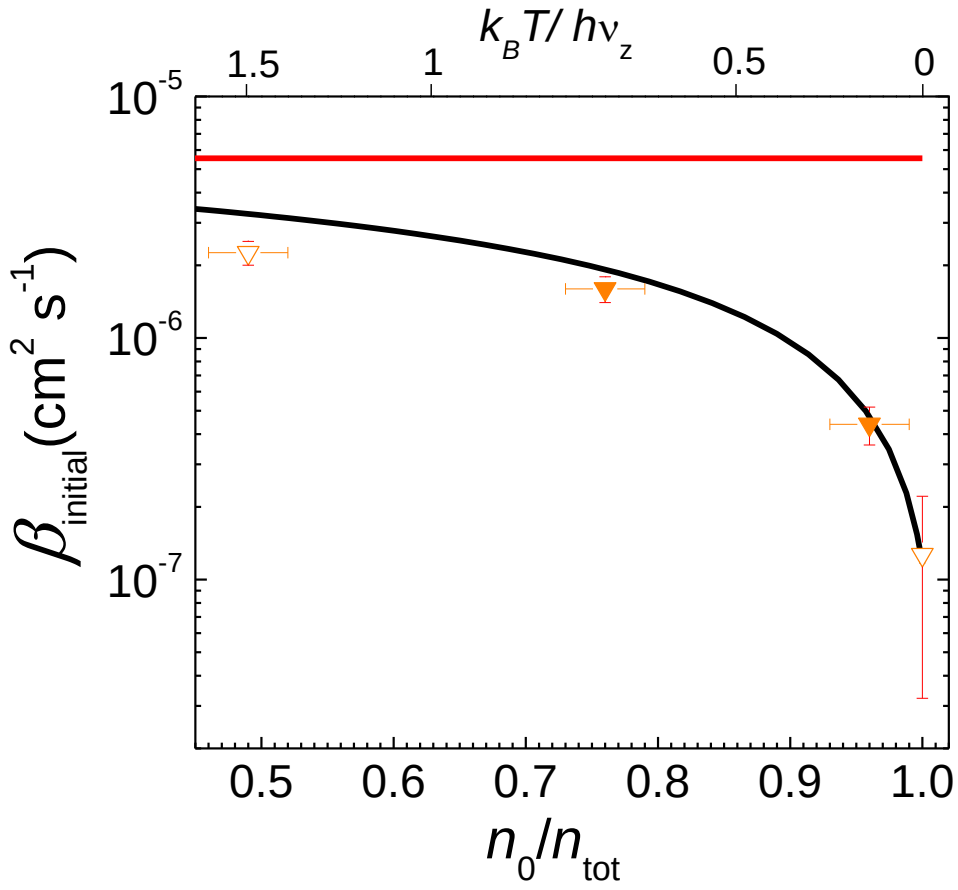

Figure 4.7: The effective initial loss rate, β_{initial}, for polar molecules confined in a 2D geometry depends on the fractional population (n_0/n_{tot}) in the lowest harmonic oscillator level in $\hat{z}$, which for a gas in thermal equilibrium depends on the ratio $k_B T/h\nu_z$. The measured initial loss rates for a dipole moment of 0.174 D are shown for two different thermal distributions (solid triangles), a non-thermal sample created by parametric heating (the top open triangle) and an extracted pure $\beta_{|3\rangle}$ for the limit of the entire population residing in the lattice ground vibrational level (the bottom open triangle). The experimental results agree well with a simple model (black curve) described in the text. The top line indicates the value of $\beta_{|2\rangle}$ as given in figure 4.6. Figure reproduced from reference [3].

the suppressed loss-rate constant measured in quasi-two dimensions. For the comparison, the 2D loss rate is scaled to three dimensions using $\beta_{3D} = \sqrt{\pi} a_{ho} \beta_{2D}$ [58, 60, 61]. At $d = 0$ the loss rate for 2D is 2/3 of the 3D rate because only two of the three $L = 1$ channels are allowed in 2D for indistinguishable molecules in the same v state. For a dipole moment d, greater than 0.1 D, the 3D loss-rate constant increases markedly as d^6 [2, 53], whereas the scaled loss-rate constant for the quasi-2D case remains close to the value at zero electric field. At a dipole moment of 0.174 D, the measured suppression in quasi-two dimensions is a factor of 60.

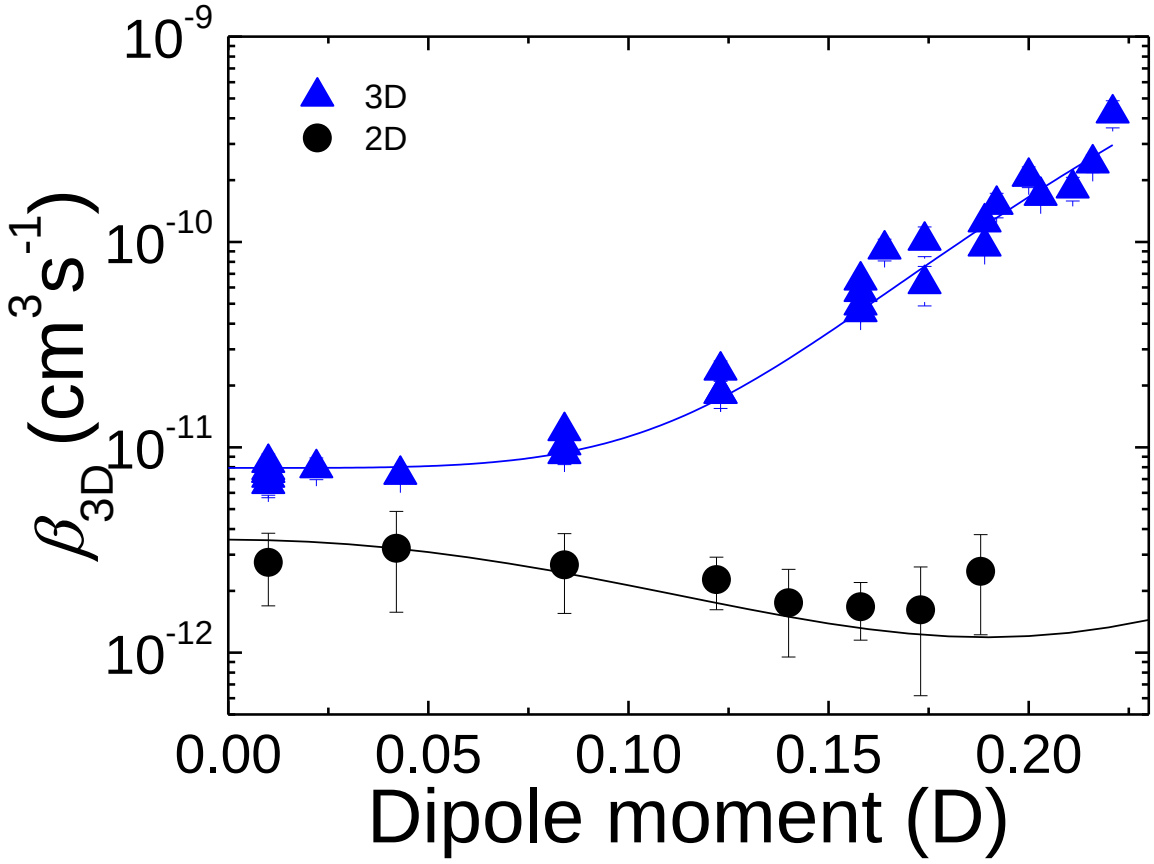

Figure 4.8: The extracted intralevel loss rate for identical fermionic KRb molecules in two dimensions (black circles) compared with the loss rate in three dimensions (blue triangles). The 3D data for $T = 300$ nK are from Ref. [2]. The 2D data were taken at $T = 800$ nK and are converted to 3D rates by multiplication with $\sqrt{\pi}a_{\mathrm{ho}}$, where a_{ho} is the harmonic oscillator length in $\hat{z}$. Figure reproduced from reference [3].

Chapter 5

Molecules in a 3D lattice

Controllable long-range and anisotropic dipole-dipole interactions can enable novel applications of quantum gases in investigating strongly correlated many-body systems [62, 7, 63, 13, 64, 65]. Recent experiments have realized an ultracold gas of polar molecules in the ro-vibrational ground state [19] with high-resolution, single-state control at the level of hyperfine structure [20]. However, an obstacle to creating long-lived quantum gases of polar molecules was encountered with the observation of bimolecular chemical reactions in the quantum regime [1]. Even with the demonstrated strong suppression of the reaction rate for spin-polarized fermionic KRb molecules, the lifetime of a 300 nK sample with a peak density of $10^{12}/\text{cm}^3$ was limited to $\sim$1 s. Furthermore, when an external electric field is applied to polarize the molecules in the lab frame, the attractive part of the dipole-dipole interaction dramatically increases the ultracold chemical reaction rate, reducing the lifetime of the dipolar gas to a few ms when the lab-frame molecular dipole moment reaches 0.2 Debye [2]. A promising recent development was the demonstration that confining fermionic polar molecules in a 1D optical lattice could suppress the rate of chemical reactions even in the presence of dipolar interactions. Here, the spatial anisotropy of the dipolar interaction was exploited by confining a gas of oriented KRb molecules in a two-dimensional geometry to suppress the attractive part of the dipolar interaction and thus achieve control of the stereodynamics of the bimolecular reactions [3]. In this regime, the lifetime of a trapped gas of polar molecules with a lab-frame dipole moment of approximately 0.2 Debye, a temperature of 800 nK, and a number density of 10^7 cm^{-2}, was approximately 1 s.

In this chapter, we study KRb molecules confined in 2D and 3D optical lattice traps, where we explore the effects of the lattice trap confinement on the lifetime of the ultracold gas. We note that a lifetime of 8 s has been achieved for homonuclear Cs_2 molecules in a 3D lattice [66]. In our work, we also find that long lifetimes are achieved for the molecules in a strong 3D lattice trap, even when there is a significant dipole moment in the lab frame. In addition, we observe that adding a weak axial corrugation to a 2D lattice can result in long lifetimes for the trapped molecules. In contrast to our previous experiments where ground-state polar molecules were created starting with ultracold atoms in a harmonic trap, here we report on the creation of ground-state KRb molecules starting from ultracold K and Rb atoms loaded into a 3D lattice. To aid in future efforts to optimize the ground-state molecule creation process, we have also examined the creation efficiency and lifetime for the weakly bound Feshbach molecules that provide the starting point for coherent two-photon optical state transfer to the molecular ground state. Much of this chapter is reproduced from reference [4] of which I am an author.

5.1 Preparation of ground state molecules in a 3D lattice

The experiments start with an ultracold mixture of 2.9×10^5 ^{40}K atoms and 2.3×10^5 ^{87}Rb atoms in a crossed optical dipole trap (ODT) at 1064 nm, at a temperature that is twice the Rb condensation temperature T_c. The trap frequencies for Rb are 21 Hz in the horizontal (x, y) plane and 165 Hz in the vertical (z) direction; the trap frequencies for K are 1.37 times larger. The atoms are transferred into a 3D optical lattice in three steps. We first turn on a retro-reflected vertical beam in 150 ms to create a weak 1D lattice. In the second step, the ODT is ramped off in 100 ms so that the two beams used for the ODT (which propagate along x and y) can be converted to lattice beams by allowing them to be retro-reflected. The intensities along all three directions are then ramped to their final values in 100 ms. The three lattice beams are derived from a common laser but individually frequency shifted to give a 160 MHz frequency offset between the x and y beams and an 80 MHz frequency offset between the z beam and each of the horizontal beams. The x and y beams are elliptical with a 200×40 μm waist and are linearly polarized orthogonal in the x-y

plane; the z-beam has a circular waist of 250 μm and is linearly polarized along x. We calibrate the lattice strength using Rb atoms and then account for the differences in mass and ac polarizability to get the lattice strength for KRb molecules. We use two different calibration methods, which yield consistent results. The first method consists of fitting the time-dependent oscillations seen in the diffraction pattern of a BEC after a Kapitza-Dirac scattering pulse [41], while in the second method, the lattice intensity is modulated to drive atoms in a reasonably deep lattice to higher lattice vibrational states. The values reported herein for the lattice depth in each direction are expressed in units of the molecule recoil energy, $E_{\rm rec}$, and have an estimated 10% uncertainty.

Once the atoms are loaded in the 3D lattice, we ramp an external magnetic field across an s-wave Feshbach resonance at 546.78 G to form loosely bound ^{40}K^{87}Rb molecules with an efficiency of about 10%. With the Feshbach molecules at $B = 545.8$ G, where their binding energy is $h\times$400 kHz, we use two-photon stimulated Raman adiabatic passage (STIRAP) to coherently transfer the Feshbach molecules to the ro-vibrational ground state [19], with a typical one-way transfer efficiency of 80%. All the molecules are in a single nuclear spin state in the rotational ground state, $|N = 0, m_N = 0, m_I^K = -4, m_I^{Rb} = 1/2\rangle$, following the notation defined in [20]. We then remove unpaired K atoms using a resonant light pulse on the $S|F = 9/2, m_F = -9/2\rangle \rightarrow P|F = 11/2, m_F = -11/2\rangle$ transition, where S and P denote electronic ground and excited states of the atoms, while F and m_F denote the total atomic spin and its projection. We remove unpaired Rb atoms using a microwave adiabatic rapid passage from $S|1,1\rangle \longrightarrow S|2,2\rangle$ followed by a light pulse on the $S|2,2\rangle \longrightarrow P|3,3\rangle$ transition. To measure the number of ground-state molecules in the lattice, we reverse the STIRAP process and then image the resultant Feshbach molecules using absorption of a probe beam that is tuned to the $S|9/2,-9/2\rangle \rightarrow P|11/2,-11/2\rangle$ transition for K atoms.

5.2 Ground state molecule lifetime in the 3D lattice

Figure 5.1 shows a time-dependent evolution of the ground-state molecule population in the 3D lattice. In the first few hundreds of ms, the measured number of molecules exhibits relatively

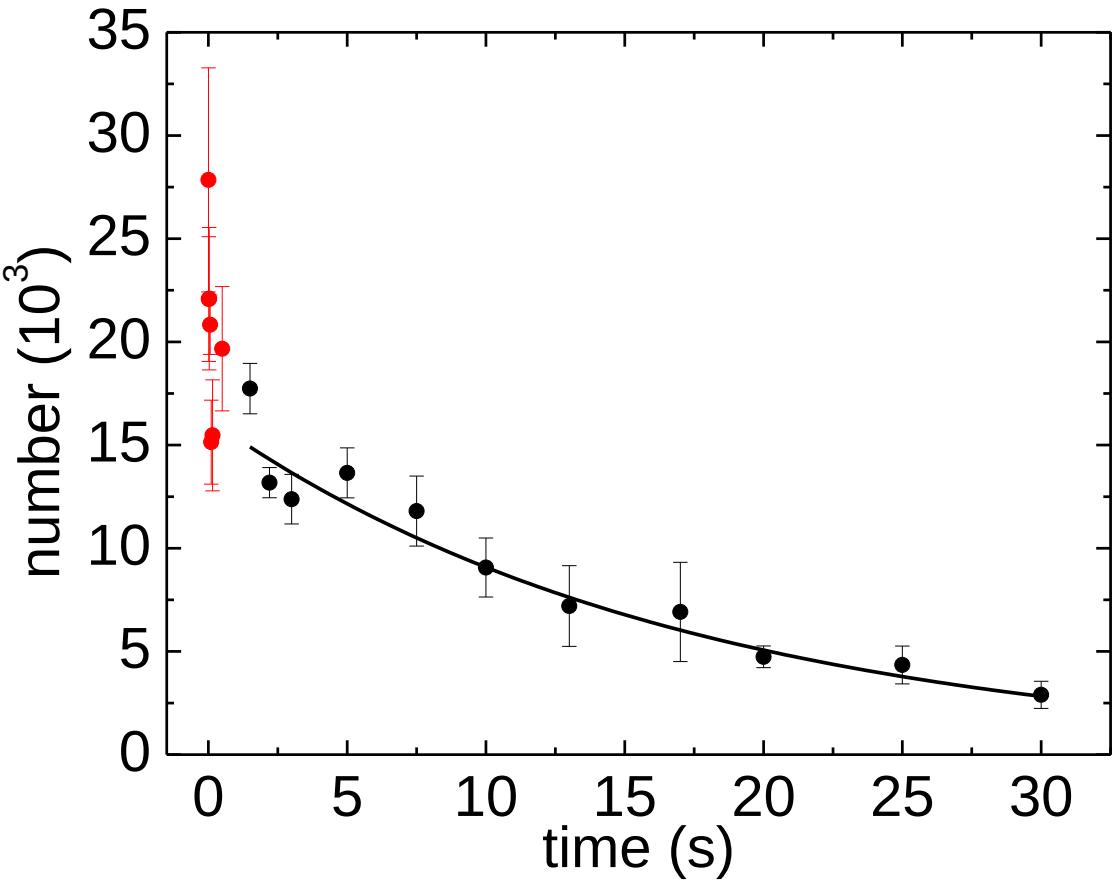

Figure 5.1: Loss of ground-state KRb molecules as a function of time in a 3D lattice with depths of 56, 56, and 70 E_{rec} in x, y, and z, respectively, where $E_{\mathrm{rec}} = \hbar^2 k^2/2m$ is the KRb recoil energy, k is the magnitude of the lattice beam wave vector, and m the molecular mass. Neglecting the very short time points (red solid circles), the number of molecules for times larger than 1 s (black solid circles) are fit to a single exponential decay, yielding a $1/e$ lifetime of 16.3±1.5 s. Figure reproduced from reference [4].

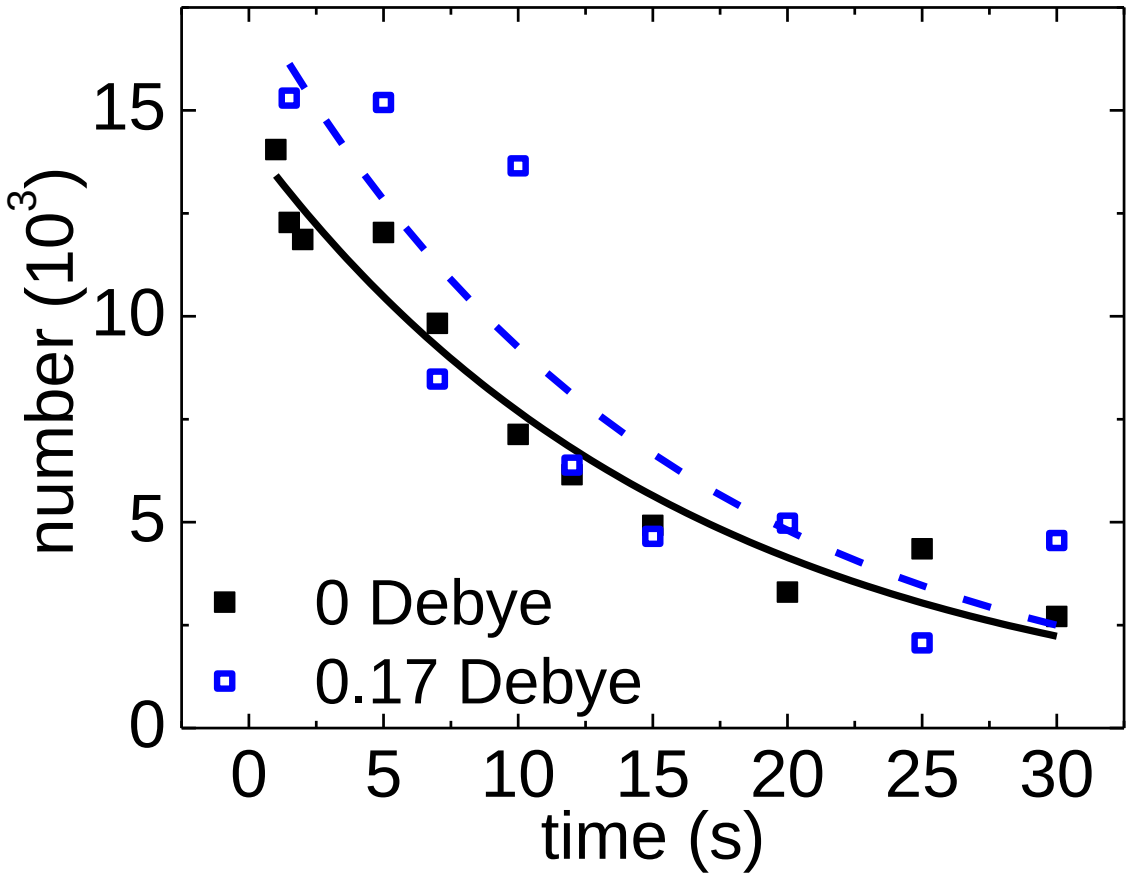

Figure 5.2: Comparison of the molecule lifetime in an isotropic lattice with a depth of 50 E_{rec} in each direction, with (blue open squares) and without (black squares) an applied electric field. The $1/e$ lifetime for molecules with an induced dipole moment of 0.17 Debye, 15±4 s, and the lifetime from molecules without dipole-dipole interactions, 16.2±1.5 s, agree within uncertainty. Figure reproduced from reference [4].

large variations in repeated iterations of the experiment and is consistent with some fast initial decay in the number of trapped ground-state molecules. In all our measurements of ground-state molecules in deep 3D lattices (for example, in the data for figure 5.3), we observe a similar feature. One possible explanation for this fast decay is collisions of the ground-state molecules with impurities, such as molecules in excited internal states that might be produced in the STIRAP process. Fitting the data for times greater than 1 s to an exponential decay, which is consistent with a single-body loss mechanism, gives a $1/e$ lifetime of 16.3±1.5 s. This is much longer than previously measured lifetimes of trapped ultracold polar molecules of about 1 s in an ODT [1] or in a 1D lattice [3] where bimolecular reactions are the dominant loss mechanism.

The long lifetime for ground-state molecules in a reasonably deep 3D lattice can be understood simply from the fact that the optical lattice trap localizes the molecules and therefore prevents bimolecular reactions. It was previously seen that an applied electric field, which induces a lab-frame dipole moment in the molecules, strongly increased the chemical reaction rate [2]. However, for molecules individually isolated in a 3D lattice, we expect no dependence of the lifetime of the trapped molecules on the strength of an applied electric field. In figure 5.2, we show that indeed we do not observe any decrease of the lifetime for polarized molecules with a dipole moment of 0.17 Debye.

5.3 2D to 3D

To understand what limits the lifetime of the molecules in the 3D lattice, we investigate its dependence on the lattice strength as summarized in figure 5.3. First, we explore the transition from a 2D lattice (an array of one-dimensional tubes) to a 3D lattice. The x and y lattice beams are kept at an intensity corresponding to 56 E_{rec} and the intensity of the lattice beam along z is varied from 0 to 136 E_{rec}. In this configuration, the harmonic trapping potential due to the gaussian spatial profiles of the x and y beams can support the molecules against gravity even for the case of no lattice in z. For a molecular gas confined in the tubes with no lattice in z, we find a lifetime of ∼1 s, similar to that observed in the ODT [1] or in a 1D lattice [3]. However, as soon as a small

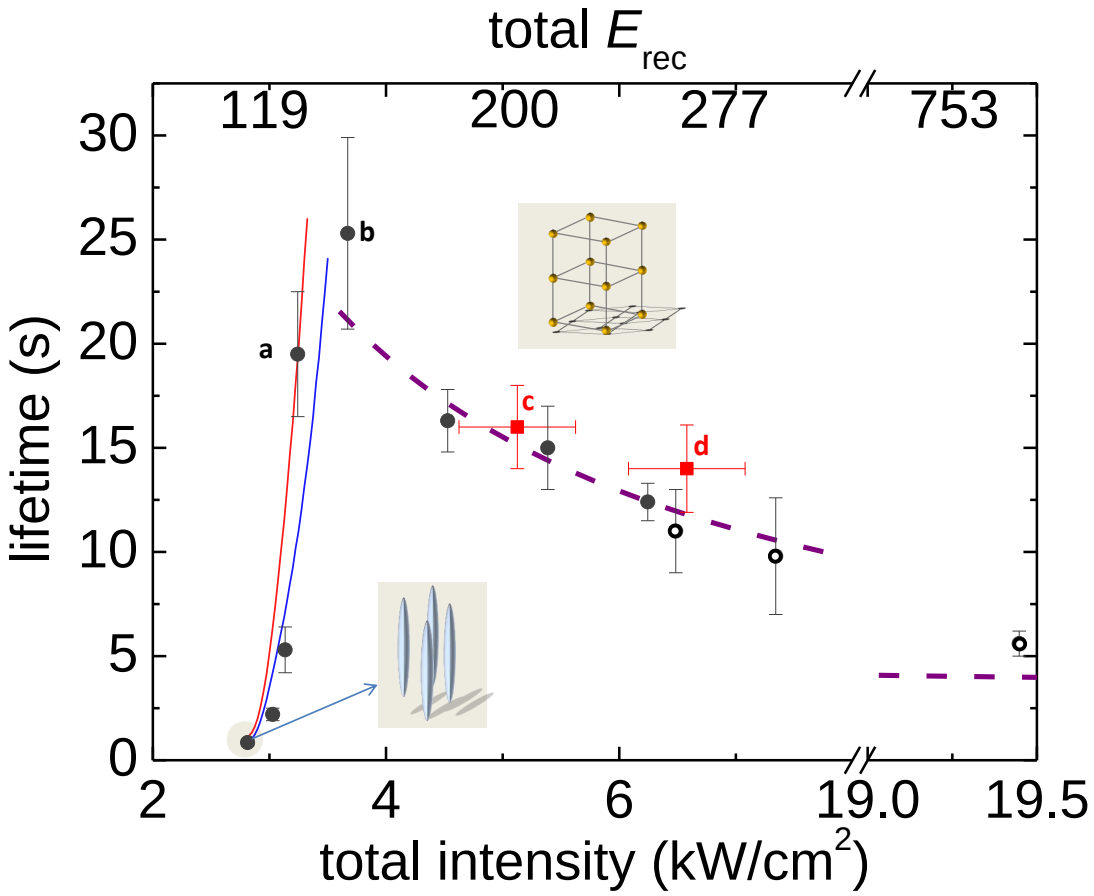

Figure 5.3: Measurement of the lifetime of KRb ground-state molecules in an optical lattice as the confinement is changed from a 2D lattice to a 3D lattice. Black circles: The radial confinement by the x and y lattice beams is set at 56 E_{rec} per beam, while the potential along z is varied from 0 to 136 E_{rec} (1 E_{rec} corresponds to a lattice intensity $I = 0.025$ kW/cm^2). The lifetime reaches a maximum of 25±5 s when the z lattice depth is 34 E_{rec} (point **b**). For higher lattice intensities, the lifetime decreases, and we find that the lifetime depends on the total intensity of the light, rather than just on the lattice strength, which is consistent with loss due to off-resonant light scattering. The open circles correspond to 3D lattices where the radial confinement was also varied. The red squares correspond to lifetimes measured with an additional traveling-wave beam at 1064 nm illuminating the molecules in the 3D lattice. Point **c** (**d**) corresponds to the 3D lattice of point **a** with an intensity of 3.2 kW/cm^2 (**b** with 3.7 kW/cm^2) plus the additional beam intensity of 2.3 kW/cm^2 (3.5 kW/cm^2). Figure reproduced from reference [4].

lattice potential is added along z, the lifetime is dramatically increased, reaching 5 s at 12 E_{rec} and 20 s at $17E_{\mathrm{rec}}$ (point **a** in figure 5.3). To verify that bimolecular reactions are the dominant loss mechanism, we have checked that the lifetime in uncorrugated tubes decreases significantly (to 0.1 s) when we apply an electric field (oriented along the tubes) that gives an induced dipole moment of 0.17 Debye. In addition, the fact that we can place an upper limit of 10% of the initial number remaining at long times puts a limit on the contribution to our signal from tubes that are occupied with only one molecule.

We consider a number of factors to understand the rapid suppression of loss as a function of the lattice strength in $\hat{z}$. In general, Pauli blocking for identical fermions and dissipation blockade effects (suppression of loss when the loss rate for particles on the same site is much larger than the tunneling rate [67]) can play a role in the lifetime of KRb molecules in an optical lattice. However, it should be noted that in the measurements reported here, the optical lattice is sparsely filled. For our identical fermionic molecules, we expect Pauli blocking would give rise to a rapid suppression of loss as a function of the lattice strength in z, with an even steeper function than we observe in the measurements. Moreover, we find that for the case of a 5 E_{rec} lattice in z, the lifetime of KRb molecules in the tube does not change significantly in the presence of an applied electric field. This observed insensitivity of the lifetime to a change of the on-site loss rate suggests that an incoherent process, such as heating of the trapped gas, is responsible for limiting the lifetime in this regime of weak lattice confinement. Instabilities in the optical phase of the lattice beams directly give rise to translational noise of the lattice, which can promote molecules to higher bands of the lattice, where they have increased mobility and could then collide with other molecules. Using a simple model employing a single parameter representing a constant heating rate, and considering that molecules in higher bands will collide on a timescale much shorter than the heating time, the theoretically predicted trend of loss suppression (represented by two solid lines in figure 5.3, corresponding to heating rates of 1 E_{rec}/s (66 nK/s) and 2 E_{rec}/s, respectively) is consistent with the experimental observation.

The lifetime reaches a maximum of 25$\pm$5 s when the lattice potentials are 56, 56, and 34 E_{rec}

in x, y, and z, respectively. As the intensity is increased further, the lifetime starts to decrease, consistent with off-resonant photon scattering becoming the dominant loss mechanism. The rich internal state structure of molecules ensures that each off-resonant photon scattering event has a high probability of causing the loss of a molecule from the ground state. To explore this effect, we added an additional traveling-wave beam with a wavelength of 1064 nm; this increases the photon scattering rate without increasing the trap depth. In figure 5.3, we compare the measured lifetimes with (red squares **c** and **d**) and without (black circles **a** and **b**) this extra light beam and observe a significant reduction of the lifetime due to the additional light. We can extract the imaginary part of the polarizability of ^{40}K^{87}Rb molecules by fitting the lifetime as a function of the light intensity to $1/(\alpha I)$. Here, α is the imaginary part of the polarizability at 1064 nm, which we determine to be $(2.052 \pm 0.009) \times 10^{-12}$ MHz/(W/cm^2); this is consistent with a theory estimate for KRb [68]. Light scattering has also been found to limit the lifetime of ground state Cs_2 in a 3D lattice [66].

5.4 Feshbach molecules in 3D

We have also explored the lifetime of KRb Feshbach molecules in the 3D optical lattice. In addition to intrinsic interest in these exotic weakly bound molecules, understanding their lifetime is important because the Feshbach molecules are the starting point for the coherent Raman transfer that produces ground-state KRb molecules. The Feshbach molecules only exist near a magnetic-field-tunable Feshbach scattering resonance and their size can be controlled with the detuning of the magnetic field from the resonance. It has been shown that these weakly bound molecules can be rapidly lost from an ODT due to collisions with atoms [69]. Our conversion of atoms to Feshbach molecules typically has an efficiency of only 10 to 20%, and therefore removal of the remaining atoms is important to prevent loss due to atom-molecule collisions. Even with removal of the Rb atoms (as described above) and the RF transfer of the K atoms to a different hyperfine state, all previously measured lifetimes for KRb Feshbach molecules were less than 10 ms [18]. However, with the ability to create ground-state molecules, which do not scatter light that is resonant with the single-atom transitions, we can more efficiently use light pulses to remove any residual atoms.

In particular, removal of K atoms, where light on the cycling transition is absorbed by the Feshbach molecules as well as by the atoms, is facilitated by hiding the molecules in the ground state. A few ms after this atom removal, we reverse the STIRAP process and re-create a Feshbach molecule gas. For the case of molecules in the ODT (no lattice), we find that this extends the lifetime of the Feshbach molecules to 150 ms. Therefore, we can conclude that previous lifetime measurements were likely limited by collisions with residual atoms.

When we perform the procedure described above for KRb molecules in an optical lattice, we find that the purified gas of Feshbach molecules can have lifetimes as long as 10 s. We explore the lifetime of the Feshbach molecules in the 3D lattice as a function of the magnetic-field detuning from the resonance ($B_0 = 546.78$ G), where varying the magnetic field changes the binding energy and the size of the Feshbach molecules. We start by forming a purified sample of the Feshbach molecules in a strong 3D lattice with an intensity of 50 E_{rec} per beam at a magnetic field $B = 545.8$ G. The magnetic field is then ramped to its final value in 1 ms. At the end of the hold time in the 3D lattice, B is ramped back to 545.8 G where we image the molecules.

The Feshbach molecule lifetime measurements are shown in figure 5.4. Above the Feshbach resonance, the lattice potential allows for the existence of confinement-induced molecules that do not exist in free space [70]. We find that confinement-induced molecules have a lifetime (25 s) that is comparable to that for K or Rb atoms in the same trap. Below the Feshbach resonance, the molecule lifetime decreases quickly when the magnetic field is ramped to lower values. Several Gauss away from the resonance, the Feshbach molecule lifetime is reduced to approximately 1 s, which is still significantly longer than in the ODT. Overall, these results represent a two-orders-of-magnitude improvement in the lifetime of Feshbach molecules compared to a previous measurement of KRb molecules in an optical lattice [71].

To understand the dependence of the lifetime on the magnetic field as shown in figure 5.4, we can assume that the lifetime is limited by off-resonant photon scattering from the lattice light and consider two limiting cases. For $B \gg B_0$, the photon scattering limit is simply that for free atoms Γ_{atom}; for $B \ll B_0$, we have a higher photon scattering rate $\Gamma_{molecule}$ due to a larger wavefunction

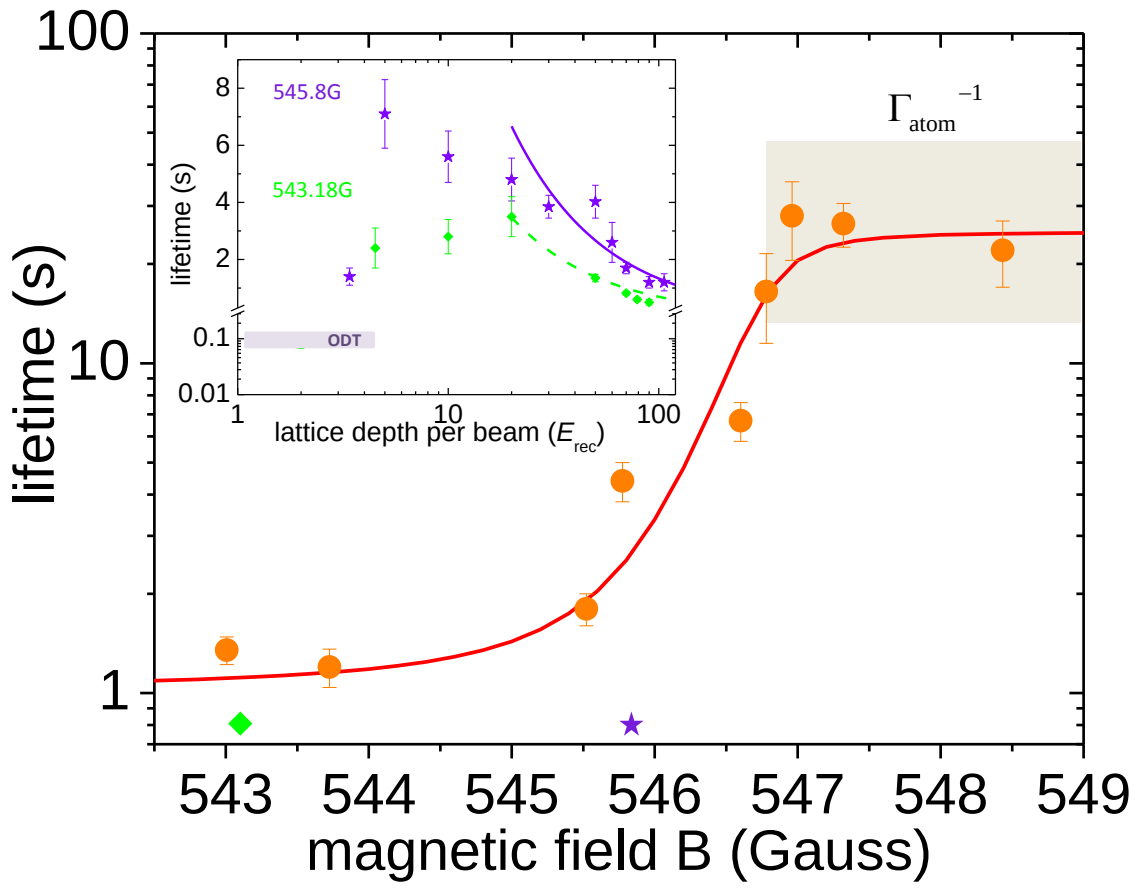

Figure 5.4: The lifetime of Feshbach molecules and confinement-induced molecules measured as a function of the B-field. A purified sample of Feshbach molecules is held in an isotropic 3D optical lattice (50 E_{rec} per beam, 20 kHz trap frequency). Near the Feshbach resonance, the loss rate due to photon scattering can be modeled (solid line) as a weighted sum of the free atom loss rate Γ_{atom} and a higher loss rate for tightly bound molecules $\Gamma_{molecule}$. The grey shaded area indicates the single atom lifetime, and its uncertainty, measured for the same experimental conditions. Inset: The lifetime of Feshbach molecules in a 3D lattice as a function of the trap intensity, at 545.8 G (blue stars) and 543.18 G (green diamonds). A small change in the intensity initially increases the lifetime from 150 ms in the ODT to 9 s in the 3D lattice at 5 E_{rec} per beam (blue stars). The lifetime then decreases as the intensity is further increased, consistent with a lifetime limited by photon scattering. For the more deeply bound Feshbach molecules (green diamonds), the lifetime is shorter. A fit to the data gives a scattering rate of 15.9±1.6 MHz/(W/cm^2) at 545.8 G and 30±3 MHz/(W/cm^2) at 543.18 G. Figure reproduced from reference [4].

overlap with electronically excited molecules and therefore an increased photon scattering rate [72]. In a two-channel model of the Feshbach resonance [73], the Feshbach molecule wavefunction can be written as an amplitude $Z^{1/2}$ times the bare "closed-channel" molecule wavefunction plus an amplitude $(1-Z)^{1/2}$ times the "open channel" wavefunction that describes the scattering state of two free atoms. We then take the total photon scattering rate to be given by $Z\Gamma_{molecule} + (1-Z)\Gamma_{atom}$. With pairs of atoms confined in an optical trap with a known depth, Z can be calculated straightforwardly with a coupled-channel theory [73, 46]. Using the measured loss rates for the limiting cases, Γ_{atom} and $\Gamma_{molecule}$, this simple theory (solid line in figure 5.4) without any additional adjustable parameters describes very well the experimental results (filled circles) across the entire range of B. We note that the rate of atom-molecule collisions properties has been analyzed in a similar way [71][74].

The assumption that the lifetime of the purified gas of Feshbach molecules in a 3D lattice is limited by only the photon scattering can be checked by varying the lattice beam intensity. This is shown in the inset of figure 5.4 for two values of B; these magnetic-field values are indicated in the main part of figure 5.4 with a blue star and a green diamond. In the inset, the lifetime is plotted as a function of the intensity per lattice beam in an isotropic lattice, expressed in units of E_{rec}. Similar to the case of ground-state molecules, we observe a rapid initial increase in the lifetime going from no lattice (only the ODT) to a weak lattice. Following this initial rise, we observe a decrease in the Feshbach molecule lifetime as the lattice intensity is increased, consistent with loss due to off-resonant scattering of the lattice light. The dashed and solid lines are fits to one over a constant times the total light intensity, and we extract an imaginary part of the Feshbach molecule's ac polarizability at 1064 nm of 15.9±1.6 MHz/(W/cm^2) for B = 545.8 G and 30±3 MHz/(W/cm^2) for B = 543.18 G.

5.5 100% conversion of atoms into Feshbach molecules

In a simple model of the conversion of atoms to Feshbach molecules in a 3D lattice, one could assume 100% conversion efficiency for individual lattice sites that are occupied by exactly one K

atom and one Rb atom, with the overall conversion efficiency then determined by the filling of the lattice and the number of such "pre-formed pairs" of atoms. The ability to prepare a purified sample of Feshbach molecules in the 3D lattice after a round-trip STIRAP sequence gives the opportunity to test the assumption of 100% conversion between pre-formed pairs of atoms and molecules. Starting with a purified sample of Feshbach molecules prepared with round-trip STIRAP and atom removal as discussed above, we dissociate the molecules in the lattice by ramping the magnetic field above the Feshbach resonance to 548.97 G. This should ideally produce only pre-formed pairs of atoms. We then ramp the magnetic field back down to 545.8 G and measure the molecular conversion efficiency. The result is $(87 \pm 13)\%$, where the uncertainty is dominated by fluctuations in STIRAP efficiency in successive runs of the experiment. This high efficiency is far above the maximum of 25% observed in an ODT [75]; this indicates that optimizing the loading procedure in order to have a larger number of sites with exactly one Rb and one K atom would optimize the efficiency of the conversion from atoms to Feshbach molecules. For heteronuclear Bose-Fermi mixtures, optimizing the number of pre-formed of atom pairs in a lattice remains a challenge. Recent progress in this direction includes the characterization of a dual Bose-Fermi Mott insulator with two isotopes of Yb [76], as well as proposals to use interaction effects to optimize the lattice loading [77, 78, 79].

Chapter 6

Anisotropic Polarizability of KRb

Molecules have complex internal structure with many more internal degrees of freedom than atoms. In particular, the rotational degree of freedom provides a set of long-lived excited states that are easily coupled to the ground state with microwaves. Because of the accessible frequency in the microwave domain and narrow intrinsic linewidth, the transition between rotational states could be ideal for use as a spectroscopic probe of the system. For example, such a narrow transition could be used to measure small energy shifts due to dipolar interactions [80]. In addition, dipole-dipole interactions can be realized without applying a DC electric field but instead by directly coupling the two lowest rotational states with a microwave field. Within the rotating frame of the microwave transition, there is a strong dipolar interaction effect, which can be used to model novel quantum many-body Hamiltonians [13]. Additionally, the microwave detuning and power can be varied to modify the collision dynamics [56]. This has been proposed as a way to achieve a topological superfluid of paired fermionic polar molecules [81].

A prerequisite for such experiments is long coherence times for the interaction between a microwave field and the rotational states. However, for molecules confined in an optical dipole trap, the difference in AC (or dynamic) polarizability between different rotational states must be considered [25]. A difference in polarizability leads to different trap frequencies and spatially dependent variations in the rotational transition frequency, which can lead to dephasing and decoherence [82]. For atoms, if the trapping light is far detuned compared to the energy splitting between two states, their AC polarizabilities will be nearly equal. In contrast, for molecules, the ground and the first

rotationally excited state with the same angular momentum projection onto the quantization axis have different parity and will therefore couple to different electronic excited states. This can result in AC polarizabilities that differ by more than 30%, even when the light is far detuned [83].

In atomic systems, it is possible to adjust the wavelength of the trapping light such that the polarizabilities of two states of interest (often clock states in alkaline earth atoms) are the same [82]. Although, in principle, one could find such a "magic" wavelength trap for molecules [84], the large number of additional states from rotation and vibration makes it difficult to find a suitable wavelength that is sufficiently detuned to avoid off-resonant light scattering. However, molecules provide a different way to adjust the polarizability; the AC polarizability of a molecule depends on the relative orientation of the molecule and the polarization of the trapping light [83].

In this Chapter, we explore the interaction between the trapping light and the molecules by examining the real part of the AC polarizability. In particular, we determine how the polarizability of the rotationally excited states depends on the relative orientation of the quantization axis, $\hat{z}$ (which in these experiments is given by a magnetic field of 545.9 G) and the polarization of the trapping light. There is a "magic" angle where the polarizability of the $|N = 0, m_N = 0\rangle$ (where N is the rotation quantum number, and m_N is its projection onto the quantization axis) and $|N = 1, m_N = 0\rangle$ states match, making the AC Stark shift the same for these two internal state of the molecule. This "magic" angle is expected at $\cos^2\theta = 1/3$, or $\theta \approx 54$ degrees [85]. We observe this magic angle both through measurements of the AC polarizability and through measurements of the coherence time for driving the $|0, 0\rangle$ to $|1, 0\rangle$ transition. We compare our experimental results to the analytic results of an approximate Hamiltonian, which mixes the three projections of the first rotationally excited state. Much of this chapter is reproduced from reference [5] of which I am an author.

6.1 Anisotropic polarizability

Molecules have a definite orientation that strongly affects their polarizability. In the frame of a diatomic molecule such as KRb, the polarizability along the internuclear axis is much stronger

than the polarizability perpendicular to the internuclear axis. This has been successfully exploited to align molecules with intense laser pulses in order to study the stereodynamics of chemical reactions [86, 87, 88]. The $N = 0$ rotational ground state is spherically symmetric and therefore its AC polarizability has no dependence on the relative orientation of the laser polarization and the quantization axis. However, the rotational wavefunction of the three projections (m_N) of the $N = 1$ rotationally excited state has a well-defined orientation relative to the quantization axis. For example, the $|1, 0\rangle$ state corresponds to a p_z orbital that is aligned along the $\hat{z}$-axis, and therefore the polarizability is the largest when the polarization of the AC field is along the $\hat{z}$-axis.

The degeneracy of the three projections of the N=1 state is broken by the hyperfine interaction, specifically, the interaction between the nuclear quadrupole moment and the rotation of the molecule [20, 89]. In the rotationally excited states, this coupling gives a specific nuclear spin state up to a 5% admixture of other hyperfine states; however, we will ignore these contributions and will work only with states whose dominant hyperfine character is $m_I^{\mathrm{K}} = -4, m_I^{\mathrm{Rb}} = 1/2$ unless otherwise noted, where m_I^{K} and m_I^{Rb} are the nuclear spin projections onto the $\hat{z}$ axis. At a field of 545.9 G and no light, we find that the $|1, 1\rangle$ state is 58 kHz above the $|1, -1\rangle$ state and the $|1, 0\rangle$ state is 268 kHz above the $|1, 1\rangle$ state (figure 6.1b). The splitting between the $m_N = \pm 1$ states is of the same order of magnitude as the AC Stark shifts induced by the trapping lasers. Consequently, we calculate the angle dependence of the dynamic polarizability of the three rotationally excited states with perturbation theory that includes the light-induced couplings between the bare states (no light).

Using the general formalism of Ref. [90], the complex dynamic polarizability for the $|0, 0\rangle$ state is given by

$$\alpha_{|0,0\rangle} = \frac{1}{3}(\alpha_{\parallel} + 2\alpha_{\perp}) \tag{6.1}$$

where the "reduced" polarizabilities $\alpha_{\parallel}$ and $\alpha_{\perp}$ are the parallel and perpendicular (with respect to the intermolecular axis) polarizabilities that describe the averaged contributions from ro-vibrational states of all electronically excited $^1\Sigma^+$ and $^1\Pi$ potentials. Because of its spherically symmetric

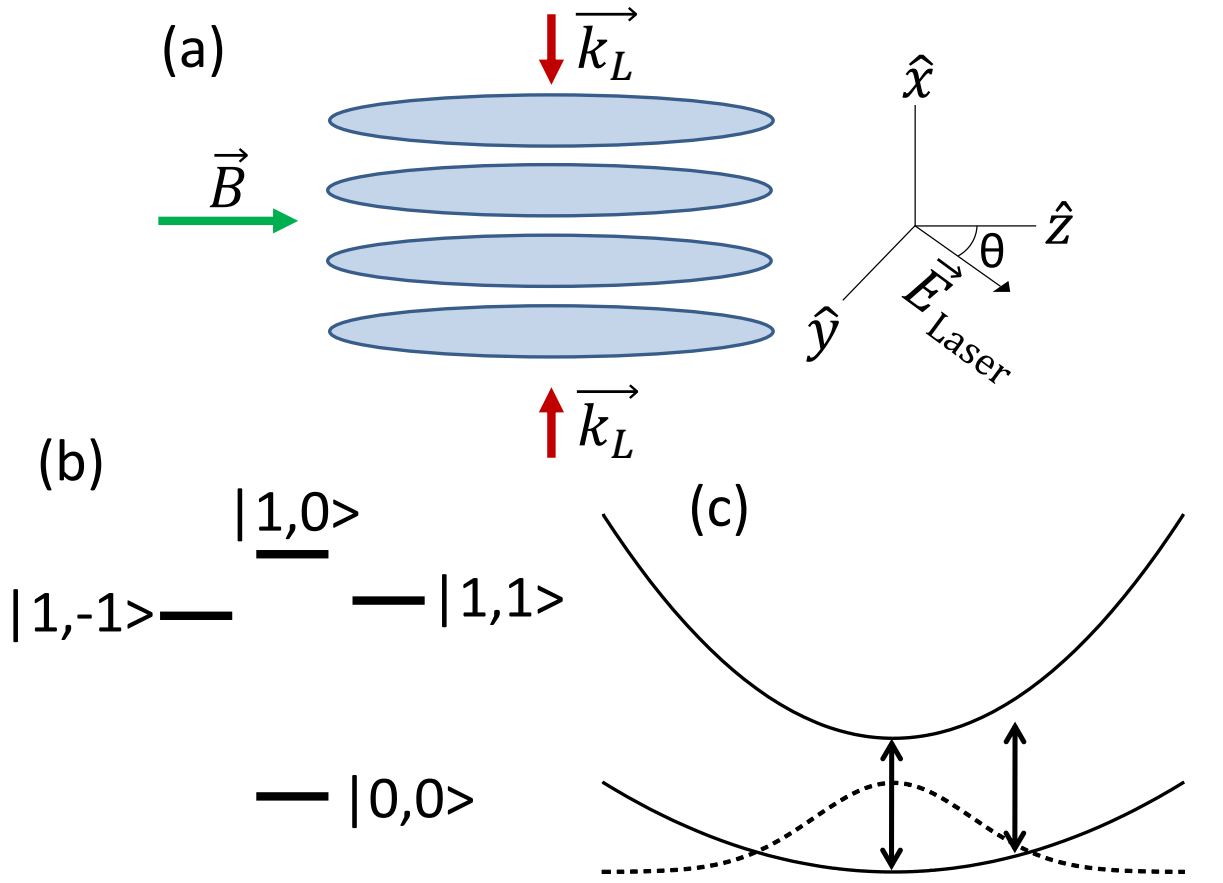

Figure 6.1: (a) Experimental schematic. The lattice beam propagates along $\hat{x}$, the magnetic field points in the $\hat{z}$ direction, and the polarization of the lattice light makes an angle θ with the magnetic field in the y-z plane. (b) Schematic of rotational energy states. The degeneracy of the $N = 1$ level is split in a magnetic field. (c) A sketch of the optical dipole potentials for the $|0, 0\rangle$ and $|1, 0\rangle$ states. A Gaussian is overlaid to show the distribution of the molecular cloud in the trap. When the two states are connected by a 2.22 GHz microwave drive, there is effectively a spatially varying detuning across the cloud due to the difference in the trap potentials. Figure reproduced from reference [5].

rotational wavefunction, the polarizability of the $|0,0\rangle$ state is independent of the angle θ between $\hat{z}$ and the polarization of the 1D optical lattice used to trap the molecules (see figure 6.1a).

For the $|1,0\rangle$ and $|1,\pm1\rangle$ states, the dressed or mixed polarizabilities at laser intensity I are given by the total Stark shift divided by the total intensity, $\alpha_j = -\frac{E_j(I)-E_j(0)}{I}$, where h is Planck's constant, and E_j, with $j = 1,2,3$, are the eigenvalues of the 3×3 Hamiltonian

$$H = \begin{array}{c} \begin{array}{ccc} |1,0\rangle & |1,-1\rangle & |1,1\rangle \end{array} \\ \begin{pmatrix} -\alpha_{11}I + \epsilon_1 & -\alpha_{12}I & -\alpha_{13}I \\ -\alpha_{12}I & -\alpha_{22}I + \epsilon_2 & -\alpha_{23}I \\ -\alpha_{13}I & -\alpha_{23}I & -\alpha_{33}I + \epsilon_3 \end{pmatrix} \end{array},$$

where

$$\begin{aligned} \alpha_{11} &= \frac{\alpha_\parallel + 4\alpha_\perp}{5}\sin^2\theta + \frac{3\alpha_\parallel + 2\alpha_\perp}{5}\cos^2\theta \\ \alpha_{22} &= \alpha_{33} = \frac{2\alpha_\parallel + 3\alpha_\perp}{5}\sin^2\theta + \frac{\alpha_\parallel + 4\alpha_\perp}{5}\cos^2\theta \\ \alpha_{12} &= -\alpha_{13} = \sqrt{2}\,\frac{\alpha_\parallel - \alpha_\perp}{5}\sin\theta\cos\theta \\ \alpha_{23} &= \frac{1}{5}(\alpha_\perp - \alpha_\parallel)\sin^2\theta\,, \end{aligned}$$

and ϵ_1, ϵ_2, and ϵ_3 are the energies for states $|1,0\rangle$, $|1,1\rangle$ and $|1,-1\rangle$, respectively, at $I = 0$.

We measure the AC polarizability of the molecules in a one-dimensional optical lattice with a peak intensity of 2.3 kW/cm^2 and a wavelength of $\lambda = 1064$ nm [3]. Using a single microwave pulse, we can selectively transfer population from the rotational ground state, $|0,0\rangle$, to any of the projections of the rotational excited states with near 100% efficiency [20]. We measure the trap depth, U_{KRb}, from which we can extract the AC polarizability, by measuring the parametric heating resonance (see figure 6.2). We modulate the intensity of the optical lattice for 4 ms with an amplitude of approximately 10% of the total depth. The modulation frequency is varied to find the resonant frequency where molecules are excited from the lowest band of the lattice to the second excited band. In the deep lattice limit, this resonant frequency is twice the trap frequency. However, we operate our lattice in an intermediate intensity regime where the relationship between

the trap depth and the resonant frequency must be extracted from a numerical solution to the lattice potential. We determine the polarizability without having to characterize the optical beam parameters such as power or beam waist by comparing the molecular result to a similar measurement of the trap depth for Rb. The polarizability of KRb is then given by $\alpha_{\mathrm{KRb}} = \alpha_{\mathrm{Rb}} U_{\mathrm{KRb}}/U_{\mathrm{Rb}}$, where $\alpha_{\mathrm{Rb}}/h = 3.242 \times 10^{-5}$ MHz/(W/cm^2) at 1064 nm [91].

In figure 6.3, we show the polarizabilities of the $N = 0$ ground state as well as the three projections of the $N = 1$ rotationally excited state as a function of θ, which is varied by adjusting a half-waveplate in the lattice beam. Although the rotation of the half-waveplate allows us to choose θ with a precision better than one degree, the absolute alignment relative to the magnetic field has an estimated systematic uncertainty of ± 3 degrees. We fit Eqn. 6.1 and the polarizabilities from the eigenenergies of H to the experimental data with three free parameters, θ_m, $\alpha_\parallel$ and $\alpha_\perp$. From the best fit, we determine that the "magic" angle $\theta_m = 48(4)$ degrees, $\alpha_\parallel/h = 10.0(3) \times 10^{-5}$ MHz/(W/cm^2), and $\alpha_\perp/h = 3.3(1) \times 10^{-5}$ MHz/(W/cm^2).

Hyperfine couplings between the $|1, 0\rangle$ and $|1, \pm 1\rangle$ states result in a small change of the magic angle from the expected value of 54 degrees. For the polarizabilities and intensity given above we would expect $\theta_m = 52$ degrees, which agrees with our fit to within the error. For comparison to the measurement, theoretical values of the polarizabilities $\alpha_\parallel$ and $\alpha_\perp$ are obtained using non-relativistic potentials and dipole moments described in Ref. [83], and are $h \times 12.2 \times 10^{-5}$ MHz/(W/cm^2) and $h \times 2.01 \times 10^{-5}$ MHz/(W/cm^2), respectively. In principle, $\alpha_\parallel$ and $\alpha_\perp$ depend on the ro-vibrational state of the molecule, however, we find in the calculation that for small N, the polarizabilities $\alpha_\parallel$ and $\alpha_\perp$ are independent of N to better than 0.01%.

Because the bare states are mixed by the lattice light, the dressed state polarizabilities depend on the intensity of the light. This effect is strongest for the $|1, \pm 1\rangle$ states, where the energy splitting of the bare states is relatively small. However, we experimentally verify that at the intensity used here this effect is small. For example, for a 50% increase in intensity with $\theta = 93$ degrees, we see only a 3.9(8)% decrease in the polarizability of the $|1, 1\rangle$ state.

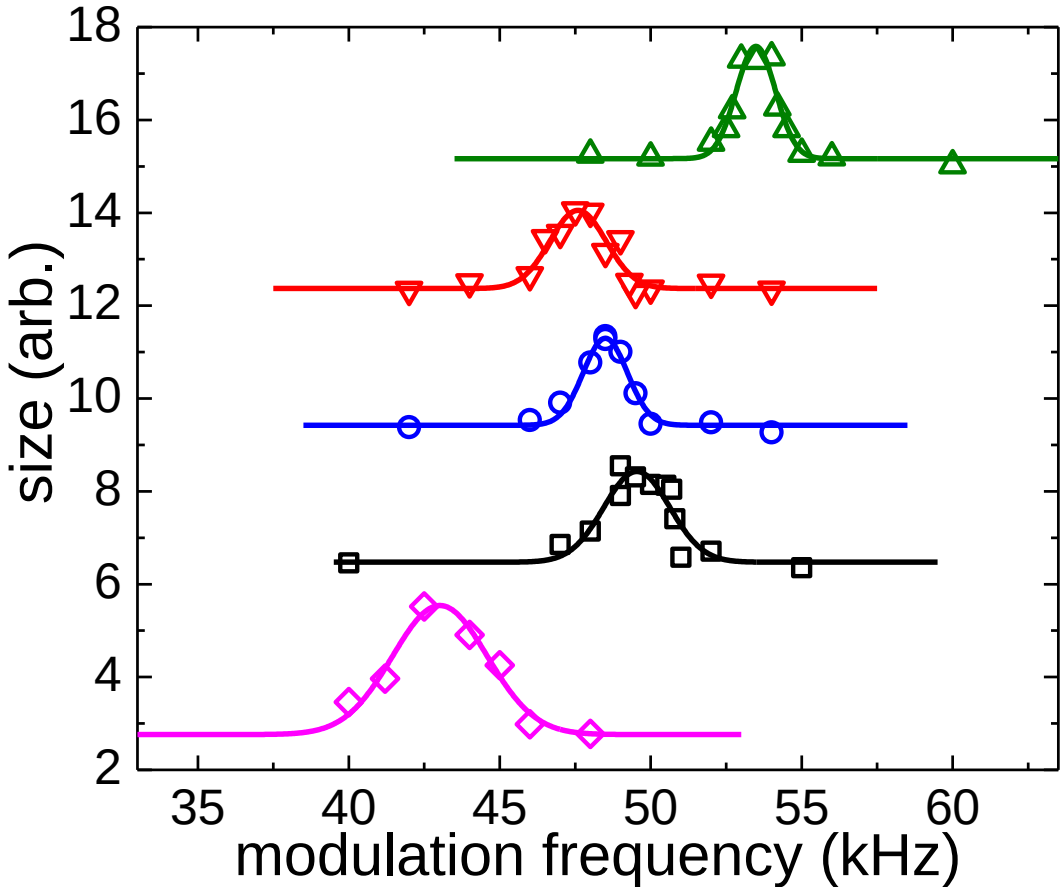

Figure 6.2: Parametric heating resonances for $\theta = 57$ degrees. The y-axis shows the rms size in $\hat{x}$ of an expanded gas of KRb (Rb) after 3 ms (21 ms) of time of flight. The curves have been offset vertically for clarity. Using Gaussian fits (lines) we determine the center of the parametric heating resonances for (from bottom to top) Rb (magenta diamonds), and KRb in the $|0,0\rangle$ (black squares), $|1,0\rangle$ (blue circles), $|1,1\rangle$ (red inverted triangles), and $|1,-1\rangle$ (green triangles) states. The resonant frequency allows us to extract the trap depth for each state. Figure reproduced from reference [5].

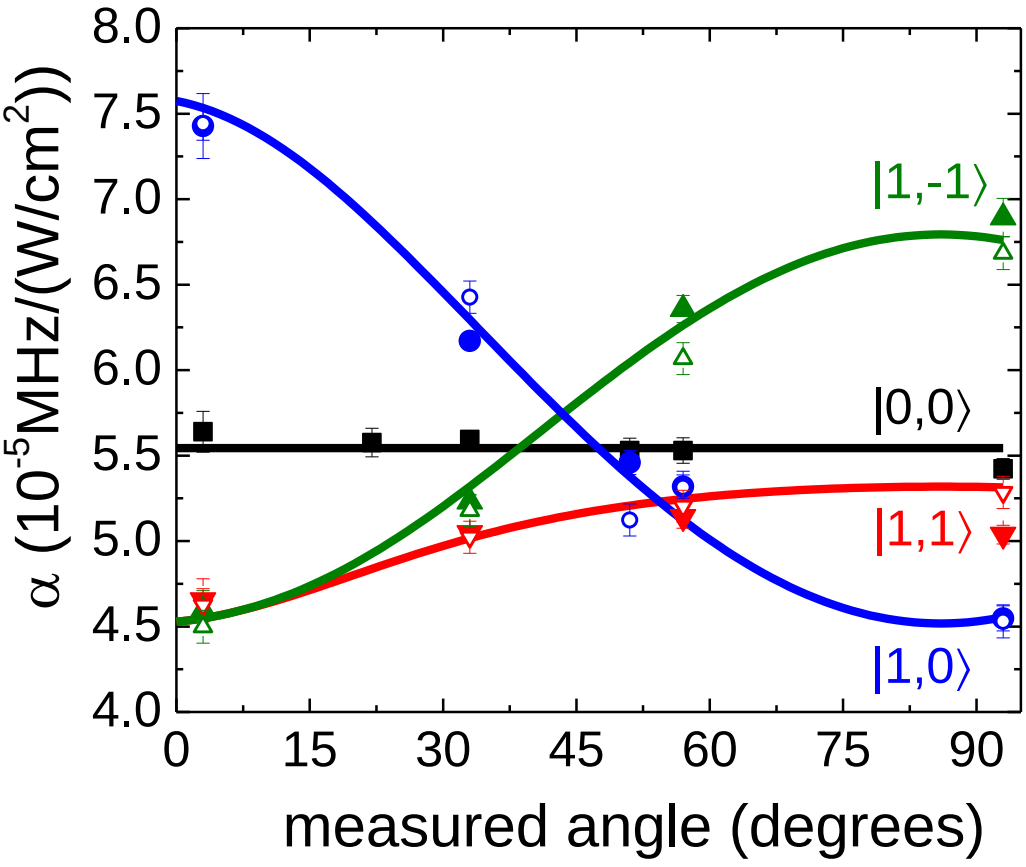

Figure 6.3: The AC polarizability of KRb at 1064 nm for the $|0,0\rangle$ (black squares), $|1,0\rangle$ (blue circles), $|1,1\rangle$ (red inverted triangles), and $|1,-1\rangle$ (green triangles) states. Error bars are from the Gaussian fit uncertainty in the center of the parametric heating resonances and correspond to ± 1 standard deviation. Theory lines are a simultaneous fit with Eqn. 6.1 and the polarizabilities from the solution of H with three free parameters θ_m, $\alpha_\perp$, and $\alpha_\parallel$. Open circles represent a separate measurement where the polarizability is extracted from the shift in the microwave transition frequency. Figure reproduced from reference [5].

6.2 A more complete model

As was shown in Ref. [20], the nuclear quadrupole moment couples to the rotation of the molecule and mixes rotationally excited states with different hyperfine character. It is precisely this coupling that breaks the degeneracy of the three projections of the $N = 1$ state. These energy shifts move the magic angle from its expected value of 54 degrees to 52 degrees. However in the previous section, other than to include this broken degeneracy, we completely ignored the couplings between different hyperfine states. To justify this assumption, we now compare the results from the approximate 3×3 Hamiltonian in the previous section to an "exact" model, which couples the nuclear spin to the rotation of the molecule.

We extend the ideas of mixing of rotational levels due a static external electric field of Ref. [83] to include mixing of rotational-hyperfine levels due to the intrinsic nuclear electric-quadrupole interactions introduced in Ref. [20]. First, we construct the full Hamiltonian for the rotational-hyperfine levels labeled by $|N, m_N, m_I^{\mathrm{K}}, m_I^{\mathrm{Rb}}\rangle$, where N is the rotation quantum number, m_N is its projection onto the quantization axis, m_I^{K} is the projection of the K nuclear spin onto the magnetic-field axis, and m_I^{Rb} is the projection of the Rb nuclear spin onto the magnetic-field axis. The Hamiltonian includes the nuclear Zeeman interaction, $-g_{\mathrm{a}}\mu_N \vec{I}_{\mathrm{a}}\vec{B}$ for atom a = K or Rb, where g_{a} is nuclear g-factor and μ_N is the nuclear magneton of atom a. It also includes the nuclear quadrupole interaction, proportional to $(eqQ)_a/(I_a(I_a-1))C_2(\theta\phi)\cdot T_2(I_a, I_a)$, with coupling constants $(eqQ)_a$ for each atom a that couples its nuclear spin to rotational states. Here, $C_{lm}(\theta\phi)$ is a spherical harmonic and $T_{2m}(I_a, I_a)$ is a rank-2 tensor created from the spin I_a. Finally, we include a polarizability interaction Hamiltonian, $-(\alpha_\parallel \mathcal{O}_\parallel + \alpha_\perp \mathcal{O}_\perp)I$, with strengths $\alpha_\parallel$ and $\alpha_\perp$, tensor operators $\mathcal{O}_\parallel$ and $\mathcal{O}_\perp$ that depend on light polarization and rotational angular momentum $\vec{N}$, and I is the peak laser intensity of the trapping light.

This Hamiltonian couples $(1 + 3) \times 9 \times 4 = 144$ channels $|N, m_N, m_I^{\mathrm{K}}, m_I^{\mathrm{Rb}}\rangle$ and has four parameters: the quadrupole interaction constants for each of the two atoms and the "reduced" polarizabilities $\alpha_\parallel$ and $\alpha_\perp$, which are the vibrationally-averaged $v = 0$ parallel and perpendicular

$\|j\rangle$	Frequency (kHz)
$\|1, 0, -4, 1/2\rangle$	2 228 110(1)
$\|1, 1, -4, 1/2\rangle$	2 227 842(1)
$\|1, -1, -4, 1/2\rangle$	2 227 784(1)

Table 6.1: The experimentally measured rotational-hyperfine transition frequencies of the lowest vibrational level of the $X^1\Sigma^+$ potential of KRb at zero laser intensity (i.e. without trapping light) and a bias magnetic field with strength $B = 545.9$ G. Transitions start at the $|N = 0, m_N = 0, m_I^{\mathrm{K}} = -4, m_I^{\mathrm{Rb}} = 1/2\rangle$ state and go to three hyperfine states $|j\rangle$ within the $N = 1$ manifold.

polarizabilities that include contributions from all excited $^1\Sigma^+$ and $^1\Pi$ potentials, respectively. We find transition energies by diagonalizing the Hamiltonian and analyzing its eigenfunctions to connect to the states that have been observed experimentally. Eigenstates are identified by the channel state with the largest contribution. Typically this contribution is more than 90% and we are justified in labeling eigenstates by one $|N, m_N, m_I^{\mathrm{K}}, m_I^{\mathrm{Rb}}\rangle$.

The two quadrupole parameters were estimated in Ref. [20] based on measurements of transition energies between sub-levels of the $N = 0$ and $N = 1$ states in the optical dipole trap. However when these measurements were made, the state-dependent polarizability and the effects of the trapping potential on the transition frequency were not yet understood, and the measurements for the different states were not taken at a constant intensity. Here we improve these constants using new measurements of the transition energies for three hyperfine levels of the $N = 1$ rotational state. We remove the effects of the trapping potential by measuring the transition energy directly after turning off the trapping light. The transition energies are given in Table 6.2.

We optimize the quadrupole constants to fit the experimental energies of Table 6.2. We find that B_e/h=1.1139514(5) GHz, $(eqQ)_{\mathrm{K}}/h$=0.452(9) MHz, and $(eqQ)_{\mathrm{Rb}}/h = -1.308(9)$ MHz. The first two values are in good agreement with the previous estimate of [20]. The $(eqQ)_{\mathrm{Rb}}$ coupling constant has changed by $\approx 7\%$.

The polarizability of eigenstate j with energy $E_j(I)$ is defined as the total Stark shift divided by the total intensity, $\alpha_j = -\frac{E_j(I)-E_j(0)}{I}$. For comparison to the approximate 3×3 Hamiltonian, we use the fitted values of $\alpha_{\|}$ and $\alpha_{\perp}$ in the "exact" model. Figure 6.4 shows the polarizability as a

function of θ based on the "exact" Hamiltonian (dashed lines), and the approximate Hamiltonian (solid lines) for the four states studied here and laser intensity I=2.35 kW/cm^2. From this figure we conclude that the agreement between the two models is good and use of the simplified approximate Hamiltonian is justified.

6.3 Shift in transition frequency

We can also use an independent measurement of the shift in the microwave transition frequency to determine the polarizability as a function of θ. The difference in polarizability between the $|0,0\rangle$ and $|1,0\rangle$ states results in different trap depths for the two states, resulting in a shift in the microwave transition frequency:

$$f = f_0 + (\alpha_{|0,0\rangle} - \alpha_{|1,0\rangle})I_0/h + \frac{\omega_{|1,0\rangle}}{4\pi} - \frac{\omega_{|0,0\rangle}}{4\pi} + \Delta f \tag{6.2}$$

where f is the measured transition frequency, f_0 is the transition frequency from $|0,0\rangle$ to $|1,0\rangle$ with $I = 0$ (measured after release from the lattice), $\omega/(4\pi) = \sqrt{\frac{\alpha I}{2\lambda^2 m}}$ is the zero point energy in the lattice divided by h, m is the mass, $\Delta f = \frac{\alpha_{|1,0\rangle} - \alpha_{|0,0\rangle}}{\alpha_{|0,0\rangle}} k_B T/h$ is the shift in the center of the transition frequency caused by the spatially dependent detuning, k_B is Boltzmann's constant, and $T = 400$ nK is the temperature. The transition frequency is only sensitive to the polarizability difference between the $|0,0\rangle$ and $|1,0\rangle$ states, but can be compared with the polarizability from the direct measurement of the trap depth by fixing $\alpha_{|0,0\rangle}$ and then solving Eqn. 6.2 for $\alpha_{|1,0\rangle}$. The resultant polarizabilities are shown in open symbols in figure 6.3. We see good agreement between the two methods.

6.4 Rotational dephasing

To study the effect of the magic angle, we measure the rotational excitation coherence time as a function of angle, and the results are shown in figure 6.5. We measure the coherence time between the $|N = 0, m_N = 0, m_I^{\mathrm{K}} = -4, m_I^{\mathrm{Rb}} = 1/2\rangle$ and $|N = 1, m_N = 0, m_I^{\mathrm{K}} = -3, m_I^{\mathrm{Rb}} = 1/2\rangle$ states with Ramsey spectroscopy. The probe pulse is 40 μs long, and the probe frequency is detuned from

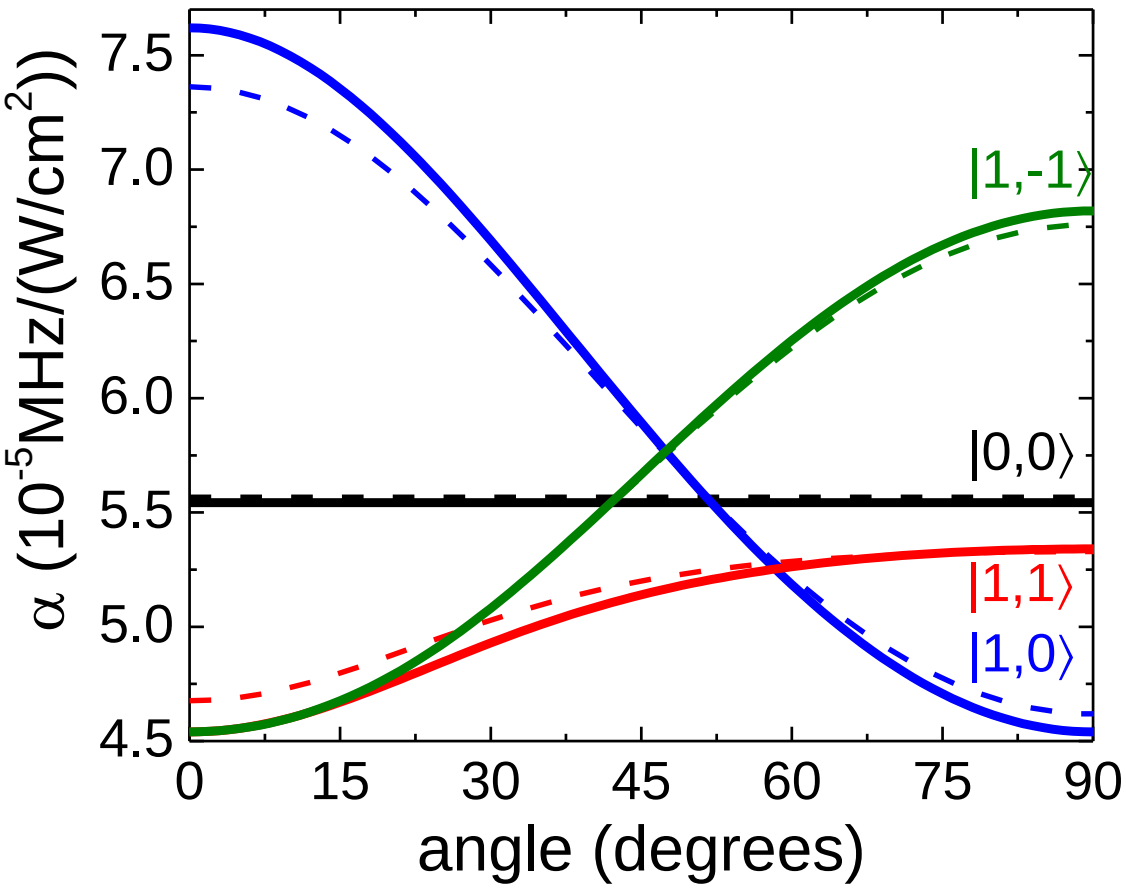

Figure 6.4: The angle-dependent polarizability for the "exact" model (dashed line) and the approximate 3×3 Hamiltonian. Figure reproduced from reference [5].

the resonance by 3 to 12 kHz. We fit the Ramsey oscillation as a function of time to a damped sine wave to extract the coherence time (see inset of figure 6.5).

The coherence time due to the mismatch in polarizability should scale as one over the difference in $\partial E/\partial I$, which because of the intensity dependence of the polarizability is not the same as the difference in polarizability. Technically, the Δf term in Eqn. 6.2 should also use the "local polarizability", $\partial E/\partial I$, instead of α because the trapped gas experiences only a small range of intensities. However, in Eqn.6.2 the difference between α and $\partial E/\partial I$ gives a small correction to a term that accounts for less than 10% of the total frequency shift, and is therefore negligible. On the other hand, because the coherence time depends critically on this polarizability difference, the "local polarizability" must be used.

We fit to the data with a simple model that includes the angular dependence:

$$\tau = 1/\sqrt{(1/T_2)^2 + \left(\frac{\partial E_{|1,0\rangle}/\partial I - \partial E_{|0,0\rangle}/\partial I}{\partial E_{|0,0\rangle}/\partial I}\Delta E/\hbar\right)^2} \tag{6.3}$$

where T_2 is the coherence time from all sources of decoherence other than the polarizability, ΔE is the spread of energy across the cloud in the $|0,0\rangle$ state, and $|\partial E_{|0,0\rangle}/\partial I - \partial E_{|1,0\rangle}/\partial I|$ depends upon θ, $\alpha_\parallel$, $\alpha_\perp$, I, ϵ_1, ϵ_2, and ϵ_3. Using the measured values of I, ϵ_1, ϵ_2, and ϵ_3 and the fitted values of $\alpha_\parallel$ and $\alpha_\perp$ from figure 6.3, we use Eqn. 6.3 and obtain $T_2 = 1.5(2)$ ms, $\Delta E/\hbar = 3.3(4) \times 10^4$ s^{-1}, and $\theta_m = 46.5(5)$ degrees. The expected value of θ_m for our values of I, $\alpha_\perp$, and $\alpha_\parallel$ is 48 degrees, which agrees with the fitted value to within the systematic error. Note that the expected value of θ is different when probing the difference in $\partial E/\partial I$ rather than α. Possible sources of T_2 range from technical noise to resonant dipole-dipole interactions [80], and further study is required to understand this limit to the coherence time.

6.5 Conclusion

In conclusion, we have measured the angle dependence of the AC polarizability of ultracold KRb and observed the "magic" angle where the polarizability of the $|0,0\rangle$ and $|1,0\rangle$ states match. Using this angle, we are able to increase the coherence time between the two rotation states by an

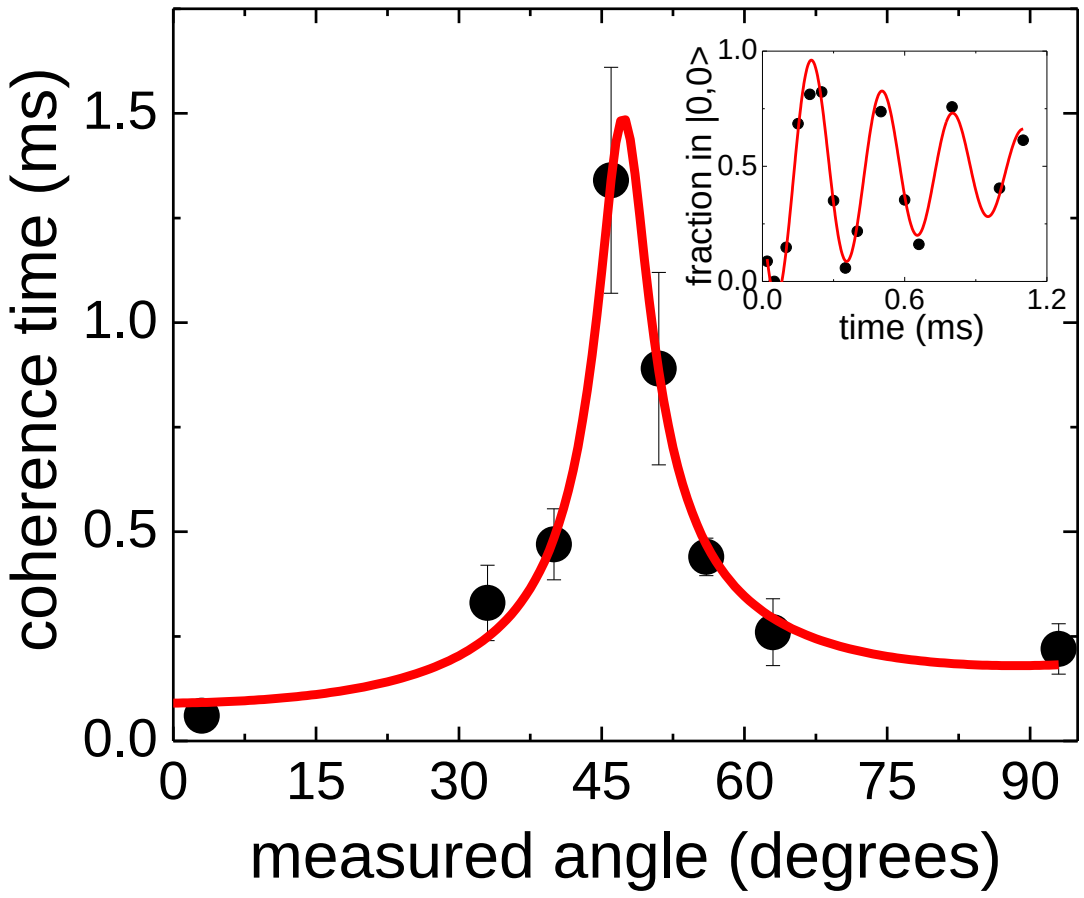

Figure 6.5: The Ramsey coherence time measured in the one-dimensional optical lattice as a function of angle. A sharp increase in coherence time is observed at the "magic" angle where the polarizabilities of the $|0,0\rangle$ and $|1,0\rangle$ states are matched. Inset: A Ramsey oscillation fit to a damped sine wave to extract the coherence time at $\theta = 51$ degrees. Figure reproduced from reference [5].

order of magnitude. This opens the way for the use of the rotational state for precision spectroscopy as well as the modification of the collision dynamics.

Chapter 7

Conclusions and Outlook

7.1 Conclusions

In this thesis I presented our studies of ultracold KRb molecules that have led to complete understanding of, and control over, both the single-particle physics as well as the two-body collisional physics of ultracold polar KRb molecules. The first step towards this goal was presented in the thesis of Josh Zirbel [40] with the creation of ultracold Feshbach molecules in a single quantum state. This was followed by the coherent transfer of the Feshbach molecules to the rovibronic ground state as described in the thesis of Kang-Kuen Ni [23]. Combined with the transfer between hyperfine states [20], this represents full control over all internal states of the molecule. We can populate the absolute rovibronic ground state and coherently transfer to other rotational or hyperfine states of our choosing with over 90% efficiency. With a single internal quantum state populated, we observed bimolecular chemical reactions at ultracold temperatures [1]. Not only is it striking that chemical reactions can still proceed at temperatures of a few hundred nK, but the chemical reaction rate is set entirely by the long-range physics, which makes it universal (in the sense that the rate does not depend on the specific short-range potential of KRb). Additionally we showed that the chemical reaction rate was strongly influenced by the long-range dipole-dipole interactions [2]. With the application of an external field to polarize the molecules, we could change the chemical reaction rate by almost two orders of magnitude.

Unfortunately, applying an electric field can only increase the chemical reaction when the molecules allowed to collide in three dimensions. By loading the molecules into a one-dimensional

optical lattice, we confine the molecules in 2D and gain full control over the chemical reaction rate. By changing the quantum states of the molecules, either in their internal states or their external motional state in the lattice, we are able to change the orientation of the collision, which changes the chemical reaction rate. We showed that we could exploit this quantum stereodynamics to suppress the chemical reaction rate in 2D if we put all the molecules in the lowest motional state of the lattice as well as a single internal quantum state [3]. This allows for the creation of a dipolar gas with a lifetime over a second.

The next step in demonstrating full control over the molecules was to further constrain their motion by creating molecules in a three dimensional optical lattice. Here, in the deep lattice limit we were able to show that the chemical reactions between molecules could be completely suppressed [4]. With each molecule isolated on its own lattice site and tunneling between sites turned off, the molecules can no longer collide and therefore can't chemically react. Although this may not seem like a very surprising result, it demonstrates an important step towards realizing many theoretical proposals to use polar molecules in a lattice to study exotic phenomena such as quantum magnetism [13] and fractional quantum hall effect [81]. We showed that the lifetime of the gas was limited only by the off-resonant light scattering from our lattice and lifetimes of up to 25 s are possible. We also demonstrated long-lived Feshbach molecules with a lifetime limited only by off-resonant light scattering. Additionally, we showed that a pair of atoms on a single site in the 3D lattice make a molecule with unit efficiency. This suggests a way forward to get a lattice with high filling of molecules.

Finally, we studied the AC polarizability of the molecule. We showed that the polarizabilities for the ground state and the three projections of the first rotationally excited state are different. Moreover, the polarizabilities of the rotationally excited states depend on the angle between the polarization of the trapping light and the quantization axis. By scanning this angle we showed that we could find a "magic" angle where the polarizabilities of the $|N = 0, m_N = 0\rangle$ and $|N = 1, m_N = 0\rangle$ states match. Here we showed an increase in the coherence time when the two polarizabilities match. This understanding of the polarizability, and the ability to get rid of the

dephasing from the spatially dependent detunings between rotational states allows us to prepare arbitrary superpositions of rotational states and preform precision spectroscopy on the rotational transition.

7.2 Future work and outlook

I see a very bright future for KRb, and many exciting things are going on in the lab as I write this thesis. With the chemical reactions suppressed and the single-particle physics understood, it is now just about time to turn our attention to studying many-body physics. This is extremely exciting because this is many-body physics arising from long-range and potentially strong interactions. But rather than give a review of the many theoretical proposals on what to do with polar molecules, I would like to focus this last section of my thesis on the shorter term goals in the lab, which focus on getting colder, denser, and more strongly interacting gases, along with suggesting some of the first places we plan to look for signals of interesting dipolar many-body physics.

7.2.1 Evaporation

One very exciting area is direct evaporation of dipolar fermions. Although we currently create the world's densest and coldest gas of ground-state polar molecules, we are still unable to produce a quantum degenerate gas. Currently there is a limit to how cold we can create our molecules because of the atoms from which we make the molecules [75]. Although there are many parameters to vary, and our optimization is by no means exhaustive, the best conditions we have ever achieved have $T/T_F = 1$. We would like to go much colder and into the quantum degenerate regime.

Because we are unable to create a degenerate gas of molecules directly from atoms, we must look to increase the phase space density of the molecules after their creation. One promising route to higher phase space density is evaporative cooling. Evaporation needs two things: rethermalization and a way to selectively remove the hottest particles. Additionally, this must happen on a timescale faster than the heating rate or loss rate. This makes KRb seem particularly challenging because it is chemically reactive, and the timescale for the loss due to chemical reactions will limit the

efficiency of evaporative cooling. We can suppress this loss by preparing our gas in a single quantum state, preventing s-wave collision that would otherwise lead to extremely fast loss due to chemical reactions.

With a spin polarized gas of fermions, we must rely on dipolar interactions to rethermalize the gas. As shown in chapter 4, we must go into a quasi-2D geometry to have both strong dipolar interactions and a long lifetime. Although this evaporation might sound difficult, we have some encouraging theoretical results from Goulven Quéméner that show the elastic to inelastic collision ratio is favorable for evaporation. The elastic and inelastic rate coefficients are shown as a function of collision energy in figure 7.1. At our starting temperature of 200 nK, we would have a good-to-bad collision ratio over 100. Furthermore, the ratio increases as the temperature goes down because the inelastic rate scales linearly with temperature.

To remove the hottest particles from the trap, we tilt the trap using an electric-field gradient similar to how a magnetic-field gradient was used in reference [92]. The gradient points along one of the radial directions of the 1D optical lattice and tilts the molecules out of the pancake-shaped traps. Although we are still in the process of designing the best way to get repeatable field gradients, we have seen some preliminary signs of evaporation, which are shown in figure 7.2. Here we held the molecules in a combined lattice plus optical dipole trap. We ramp on an electric field of 4 kV/cm in 100 ms. This induces a dipole moment of 0.158 D and we estimate the electric-field gradient at the molecules to be 125 V/cm^2. Once the field was ramped on, we ramped down the optical trap in 100 ms. This lowers the trap depth and allows the electric-field gradient to "tilt" the lattice and spill the most energetic molecules out the side. The trap was then ramped back to its original strength in 100 ms and the electric field was ramped off in another 100 ms. We plot the number of molecules remaining at the end of this sequence versus the final temperature (as measured in time of flight) on a log-log plot for various ramp depths (figure 7.2). We fit a line to the data and see a slope of 1.2(1), which for fermions in 2D corresponds to an increase in phase space density. This data must be repeated and optimized to verify that the gas is in equilibrium at the end of the evaporation ramp and evaporation is indeed taking place. But, both theoretically

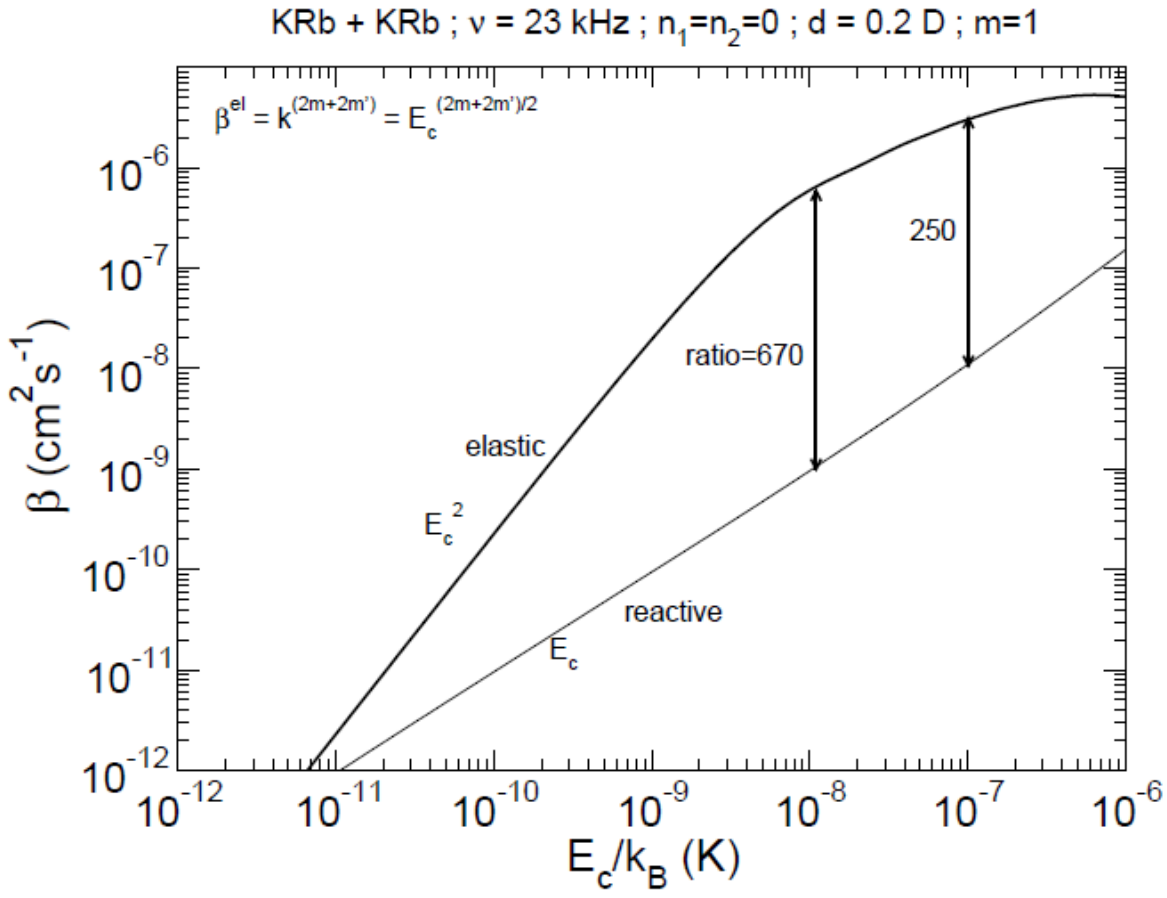

Figure 7.1: The loss rate coefficients for both reactive (inelastic) and elastic collisions as a function of the collision energy for an induced dipole moment of 0.2 Debye, a quasi 2D trap with a tight trapping frequency of 23 kHz, and indistinguishable molecules all in the lowest vibrational state of the lattice. The elastic to inelastic ratio (the ration of good to bad collisions) is over 100 in the entire region of interest. Figure courtesy of G. Quéméner.

and experimentally evaporation is looking promising.

7.2.2 Enhanced molecular formation in a 3D lattice

It was demonstrated in Chapter 5 that any lattice site with one K and one Rb atom will be converted into a Feshbach molecule with 100% efficiency. This suggests an appealing way to create a dense gas of molecules with low entropy. If we were able to start with a perfect Mott insulator of Rb with one Rb atom per lattice site, and have a band insulator of K with one K atom per lattice site, then after ramping through the Feshbach resonance we should create a gas of molecules with one molecule per lattice site, on every lattice site, all in the lowest band.

Many studies have been done exploring the interaction between K and Rb on a lattice [93, 94, 95]. These studies all treated the K atoms as an impurity, which because of the interspecies attraction, would localize the Rb and prevent a proper Mott insulator from forming. This suggests that an effective way to create a dual Mott/band insulator of K and Rb is to tune the interspecies scattering length to zero. This was demonstrated in the realization of a dual Mott insulator of bosonic and fermionic Yb [76].

We are currently working on simplifying the 3D lattice setup to minimize the heating during the load so a Mott insulator can be created.

7.2.3 Many-body physics with long-range interactions

There are a lot of theoretical proposals for all sorts of interesting things to do with ultracold polar molecules [96, 13, 97, 11, 98, 99, 100, 101, 102, 103, 81] . But really the bottom line is I'm not sure what the most interesting experiments are. So before we start engineering collisional potentials [11] or start looking for topological phases with anyonic excitations [81], we should start by looking for mean-field-like energy shifts due to the dipolar interactions. With the dephasing between rotational states understood, the transition to the rotationally excited state can serve as a good spectroscopic probe to measure energy shifts from dipole-dipole interactions [80].

I won't try to, and don't think I can, predict the physics that we will measure, but that is

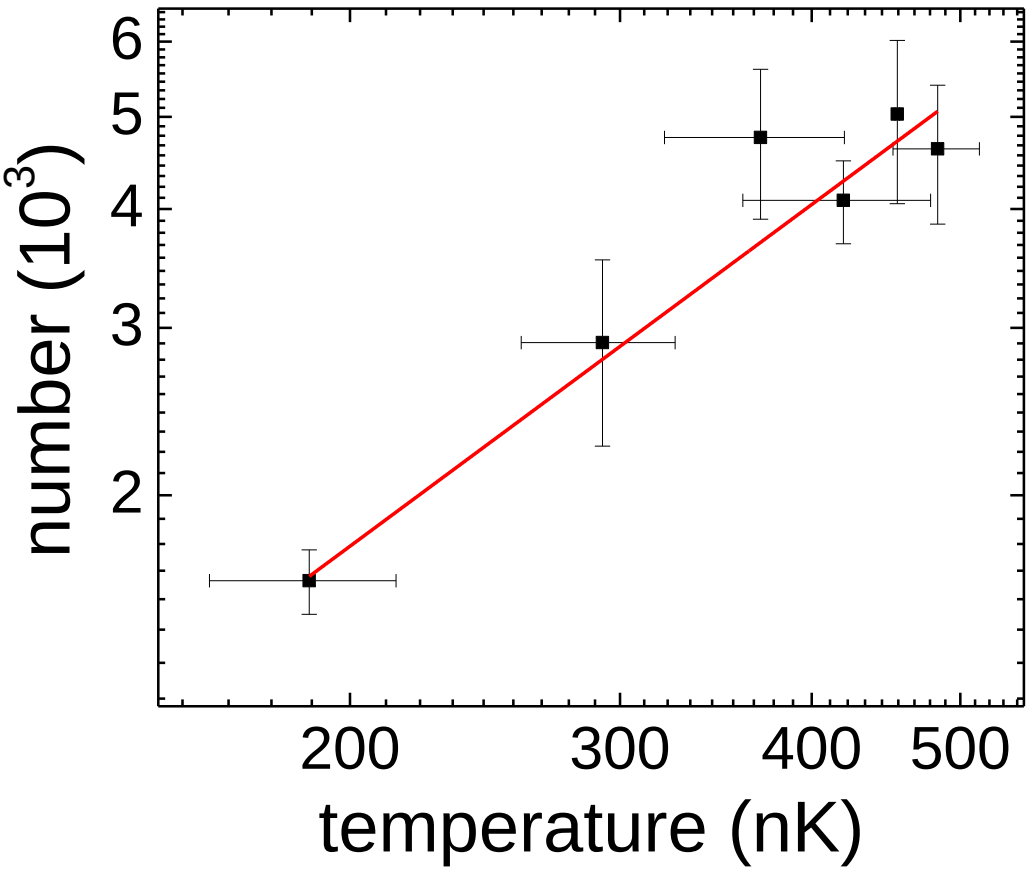

Figure 7.2: Preliminary data for direct evaporation of molecules. The number vs. temperature for different evaporation cuts is plotted on a log-log plot. The evaporation sequence is the same for all points, with only the final depth of the optical trap being varied. We see a slope of 1.2(1). Any slope less than 2 in 2D corresponds to an increase in phase space density.

partially what makes it so exciting.

Bibliography

[1] S. Ospelkaus, K.-K. Ni, D. Wang, M. H. G. de Miranda, B. Neyenhuis, G. Qumner, P. S. Julienne, J. L. Bohn, D. S. Jin, and J. Ye. Quantum-state controlled chemical reactions of ultracold potassium-rubidium molecules. Science, 327:853, 2010.

[2] K.-K. Ni, S. Ospelkaus, D. Wang, G. Quéméner, B. Neyenhuis, M. H. G. de Miranda, J. L. Bohn, J. Ye, and D. S. Jin. Dipolar collisions of polar molecules in the quantum regime. Nature, 464:1324, 2010.

[3] M. H. G. de Miranda, A. Chotia, B. Neyenhuis, D. Wang, G. Quéméner, S. Ospelkaus, J. L. Bohn, J. Ye, and D. S. Jin. Controlling the quantum stereodynamics of ultracold bimolecular reactions. Nature Phys., 7:502, 2011.

[4] A. Chotia, B. Neyenhuis, S. A. Moses, B. Yan, J. P. Covey, M. Foss-Feig, A. M. Rey, D. S. Jin, and J. Ye. Long-lived dipolar molecules and feshbach molecules in a 3D optical lattice. Phys. Rev. Lett., 108:080405, 2012.

[5] B. Neyenhuis, B. Yan, S. A. Moses, J. P. Covey, A. Chotia, A. Petrov, S. Kotochigova, J. Ye, and D. S. Jin. Anisotropic Polarizability of Ultracold Polar $^{40}K^{87}Rb$ Molecules. ArXiv e-prints, 2012.

[6] H. R. Sadeghpour, J. L. Bohn, M. J. Cavagnero, B. D. Esry, I. I. Fabrikant, J. H. Macek, and A. R. P. Rau. Collisions near threshold in atomic and molecular physics. J. Phys. B, 33:R93, 2000.

[7] G. Pupillo, A. Micheli, H. P. Buchler, and P. Zoller. CRC Press, Boca Raton, 2009.

[8] J. J. Hudson, B. E. Sauer, M. R. Tarbutt, and E. A. Hinds. Measurement of the electron electric dipole moment using YbF molecules. Phys. Rev. Lett., 89:023003, 2002.

[9] K. Beloy, A. Borschevsky, P. Schwerdtfeger, and V. V. Flambaum. Enhanced sensitivity to the time variation of the fine-structure constant and m_p/m_e in diatomic molecules: A closer examination of silicon monobromide. Phys. Rev. A, 82:022106, 2010.

[10] V. V. Flambaum and M. G. Kozlov. Enhanced sensitivity to the time variation of the fine-structure constant and m_p/m_e in diatomic molecules. Phys. Rev. Lett., 99:150801, 2007.

[11] A. V. Gorshkov, P. Rabl, G. Pupillo, A. Micheli, P. Zoller, M. D. Lukin, and H. P. Büchler. Suppression of inelastic collisions between polar molecules with a repulsive shield. Phys. Rev. Lett., 101:073201, 2008.

[12] P. A. Lee, N. Nagaosa, and X. Wen. Doping a mott insulator: Physics of high-temperature superconductivity. Rev. Mod. Phys., 78:17, 2006.

[13] A. V. Gorshkov, S. R. Manmana, G. Chen, J. Ye, E. Demler, M. D. Lukin, and A. M. Rey. Tunable superfluidity and quantum magnetism with ultracold polar molecules. Phys. Rev. Lett., 107:115301, 2011.

[14] A.P. Balachandran. Hubbard Model and Anyon Superconductivity. Lecture Notes in Physics. World Scientific, 1990.

[15] Silke Ospelkaus-Schwarzer. Quantum Degenerate Fermi-Bose Mixtures of ^{40}K and ^{87}Rb in 3D Optical Lattices. PhD thesis, University of Hamburg, 2006.

[16] C Amiot. The KRb $(2)^3\Sigma^+$ electronic state. J. Mol. Spectrosc., 203:126, 2000.

[17] U. Gaubatz, P. Rudecki, M. Becker, S. Schiemann, M. Klz, and K. Bergmann. Population switching between vibrational levels in molecular beams. Chem. Phys. Lett., 149:463, 1988.

[18] S. Ospelkaus, A. Pe'er, K. K. Ni, J. J. Zirbel, B. Neyenhuis, S. Kotochigova, P. S. Julienne, J. Ye, and D. S. Jin. Efficient state transfer in an ultracold dense gas of heteronuclear molecules. Nature Phys., 4:622, 2008.

[19] K.-K. Ni, S. Ospelkaus, M. H. G. de Miranda, A. Pe'er, B. Neyenhuis, J. J. Zirbel, S. Kotochigova, P. S. Julienne, D. S. Jin, and J. Ye. A high phase-space-density gas of polar molecules. Science, 322:231, 2008.

[20] S. Ospelkaus, K.-K. Ni, G. Quéméner, B. Neyenhuis, D. Wang, M. H. G. de Miranda, J. L. Bohn, J. Ye, and D. S. Jin. Controlling the hyperfine state of rovibronic ground-state polar molecules. Phys. Rev. Lett., 104:030402, 2010.

[21] Goulven Quéméner, John L. Bohn, Alexander Petrov, and Svetlana Kotochigova. Universalities in ultracold reactions of alkali-metal polar molecules. Phys. Rev. A, 84:062703, 2011.

[22] Eugene P. Wigner. On the behavior of cross sections near thresholds. Phys. Rev., 73:1002, 1948.

[23] Kang-Kuen Ni. A Quantum Gas of Polar Molecules. PhD thesis, University of Colorado at Boulder, 2009.

[24] Marcio H. G. de Miranda. Control of dipolar collisions in the quantum regime. PhD thesis, University of Colorado at Boulder, 2010.

[25] S. Ospelkaus, K.-K. Ni, M. H. G. de Miranda, B. Neyenhuis, D. Wang, S. Kotochigova, P. S. Julienne, D. S. Jin, and J. Ye. Faraday Discuss., 142:351, 2009.

[26] D. Wang, B. Neyenhuis, M. H. G. de Miranda, K.-K. Ni, S. Ospelkaus, D. S. Jin, and J. Ye. Direct absorption imaging of ultracold polar molecules. Phys. Rev. A, 81:061404, 2010.

[27] P. S. Jessen and I. H. Deutsch. Optical lattices. Advances in Atomic, Molecular, and Optical Physics, 37:95, 1996.

[28] D. Jaksch, C. Bruder, J. I. Cirac, C. W. Gardiner, and P. Zoller. Cold bosonic atoms in optical lattices. Phys. Rev. Lett., 81:3108, 1998.

[29] M. Greiner, O. Mandel, T. Esslinger, T. W. Hansch, and I. Bloch. Quantum phase transition from a superfluid to a Mott insulator in a gas of ultracold atoms. Nature, 415:39, 2002.

[30] M. Lewenstein, A. Sanpera, V. Ahufinger, B. Damski, A. Sen(De), and U. Sen. Ultracold atomic gases in optical lattices: mimicking condensed matter physics and beyond. Adv. Phys., 56:243, 2007.

[31] Ph. Courteille, R. S. Freeland, D. J. Heinzen, F. A. van Abeelen, and B. J. Verhaar. Observation of a feshbach resonance in cold atom scattering. Phys. Rev. Lett., 81:69, 1998.

[32] S. Inouye, M. R. Andrews, J. Stenger, H. J. Miesner, D. M. Stamper-Kurn, and W. Ketterle. Observation of Feshbach resonances in a Bose-Einstein condensate. Nature, 392:151, 1998.

[33] K. Dieckmann, C. A. Stan, S. Gupta, Z. Hadzibabic, C. H. Schunck, and W. Ketterle. Decay of an ultracold fermionic lithium gas near a feshbach resonance. Phys. Rev. Lett., 89:203201, 2002.

[34] R. Grimm, M. Weidemuller, and Y. B. Ovchinnikov. Optical dipole traps for neutral atoms. Advances in Atomic, Molecular, and Optical Physics, 42:95, 2000.

[35] S. Kotochigova, P. S. Julienne, and E. Tiesinga. Ab initio calculation of the KRb dipole moments. Phys. Rev. A, 68:022501, 2003.

[36] K. I. Petsas, A. B. Coates, and G. Grynberg. Crystallography of optical lattices. Phys. Rev. A, 50:5173, 1994.

[37] Neil W. Ashcroft and David N Mermin. Solid State Physics. Saunders College Publishing, 1976.

[38] Gregory H. Wannier. The structure of electronic excitation levels in insulating crystals. Phys. Rev., 52:191, 1937.

[39] Ana Maria Rey. Ultracold bosonic atoms in optical lattices. PhD thesis, University of Maryland at Colege Park, 2004.

[40] Joshua Zirbel. Ultracold Fermionic Feshbach Molecules. PhD thesis, University of Colorado at Boulder, 2008.

[41] J. H. Denschlag, J. E. Simsarian, H. Haffner, C. McKenzie, A. Browaeys, D. Cho, K. Helmerson, S. L. Rolston, and W. D. Phillips. A Bose-Einstein condensate in an optical lattice. J. Phys. B, 35:3095, 2002.

[42] R. Jáuregui, N. Poli, G. Roati, and G. Modugno. Anharmonic parametric excitation in optical lattices. Phys. Rev. A, 64:033403, 2001.

[43] A. Kastberg, W. D. Phillips, S. L. Rolston, R. J. C. Spreeuw, and P. S. Jessen. Adiabatic cooling of cesium to 700 nk in an optical lattice. Phys. Rev. Lett., 74:1542, 1995.

[44] M. Greiner, I. Bloch, O. Mandel, T. W. Hänsch, and T. Esslinger. Exploring phase coherence in a 2D lattice of Bose-Einstein condensates. Phys. Rev. Lett., 87:160405, 2001.

[45] H. A. Bethe. Theory of disintegration of nuclei by neutrons. Phys. Rev., 47:747, 1935.

[46] Paul S. Julienne. Ultracold molecules from ultracold atoms: a case study with the KRb molecule. Faraday Discuss., 142:361, 2009.

[47] C. Amiot. Laser-induced fluorescence of Rb_2: The $(1)^1\Sigma_g^+$(X), $(2)^1\Sigma_g^+$, $(1)^1\Pi_u$(B), $(1)^1\Pi_g$, and $(2)^1\Pi_u$(C) electronic states. J. Chem. Phys., 93:8591, 1990.

[48] St. Falke, I. Sherstov, E. Tiemann, and Ch. Lisdat. The $A^1\Sigma_u^+$ state of K_2 up to the dissociation limit. J. Chem. Phys., 125:224303, 2006.

[49] P. S. Żuchowski and J. M. Hutson. Reactions of ultracold alkali-metal dimers. Phys. Rev. A, 81:060703, 2010.

[50] P. Langevin. Ann. Chim. Phys., 5:245, 1905.

[51] Svetlana Kotochigova. Dispersion interactions and reactive collisions of ultracold polar molecules. New J. Phys., 12:073041, 2010.

[52] Zbigniew Idziaszek and Paul S. Julienne. Universal rate constants for reactive collisions of ultracold molecules. Phys. Rev. Lett., 104:113202, 2010.

[53] Goulven Quéméner and John L. Bohn. Strong dependence of ultracold chemical rates on electric dipole moments. Phys. Rev. A, 81:022702, 2010.

[54] B. DeMarco, J. L. Bohn, J. P. Burke, M. Holland, and D. S. Jin. Measurement of p-wave threshold law using evaporatively cooled fermionic atoms. Phys. Rev. Lett., 82:4208, 1999.

[55] H. P. Büchler, E. Demler, M. Lukin, A. Micheli, N. Prokof'ev, G. Pupillo, and P. Zoller. Strongly correlated 2D quantum phases with cold polar molecules: Controlling the shape of the interaction potential. Phys. Rev. Lett., 98:060404, 2007.

[56] A. Micheli, G. Pupillo, H. P. Büchler, and P. Zoller. Cold polar molecules in two-dimensional traps: Tailoring interactions with external fields for novel quantum phases. Phys. Rev. A, 76:043604, 2007.

[57] J. Stuhler, A. Griesmaier, T. Koch, M. Fattori, T. Pfau, S. Giovanazzi, P. Pedri, and L. Santos. Observation of dipole-dipole interaction in a degenerate quantum gas. Phys. Rev. Lett., 95:150406, 2005.

[58] A. Micheli, Z. Idziaszek, G. Pupillo, M. A. Baranov, P. Zoller, and P. S. Julienne. Universal rates for reactive ultracold polar molecules in reduced dimensions. Phys. Rev. Lett., 105:073202, 2010.

[59] Goulven Quéméner and John L. Bohn. Dynamics of ultracold molecules in confined geometry and electric field. Phys. Rev. A, 83:012705, 2011.

[60] D. S. Petrov and G. V. Shlyapnikov. Interatomic collisions in a tightly confined Bose gas. Phys. Rev. A, 64:012706, 2001.

[61] Z. Li and R. V. Krems. Inelastic collisions in an ultracold quasi-two-dimensional gas. Phys. Rev. A, 79:050701, 2009.

[62] M.A. Baranov. Theoretical progress in many-body physics with ultracold dipolar gases. Physics Reports, 464:71, 2008.

[63] T. Lahaye, C. Menotti, L. Santos, M. Lewenstein, and T. Pfau. The physics of dipolar bosonic quantum gases. Rep. Prog. Phys., 72, 2009.

[64] Lincoln D Carr, David DeMille, Roman V Krems, and Jun Ye. Cold and ultracold molecules: science, technology and applications. New J. Phys., 11:055049, 2009.

[65] Immanuel Bloch, Jean Dalibard, and Wilhelm Zwerger. Many-body physics with ultracold gases. Rev. Mod. Phys., 80:885, 2008.

[66] J. G. Danzl, M. J. Mark, E. Haller, M. Gustavsson, R. Hart, J. Aldegunde, J. M. Hutson, and H. Naegerl. An ultracold high-density sample of rovibronic ground-state molecules in an optical lattice. Nature Phys., 6:265, 2010.

[67] N. Syassen, D. M. Bauer, M. Lettner, T. Volz, D. Dietze, J. J. Garca-Ripoll, J. I. Cirac, G. Rempe, and S. Drr. Strong dissipation inhibits losses and induces correlations in cold molecular gases. Science, 320:1329, 2008.

[68] Svetlana Kotochigova, Eite Tiesinga, and Paul S Julienne. Multi-channel modelling of the formation of vibrationally cold polar KRb molecules. New J. Phys., 11:055043, 2009.

[69] J. J. Zirbel, K.-K. Ni, S. Ospelkaus, J. P. D'Incao, C. E. Wieman, J. Ye, and D. S. Jin. Collisional stability of fermionic feshbach molecules. Phys. Rev. Lett., 100:143201, 2008.

[70] T. Stöferle, H. Moritz, K. Günter, M. Köhl, and T. Esslinger. Molecules of fermionic atoms in an optical lattice. Phys. Rev. Lett., 96:030401, 2006.

[71] C. Ospelkaus, S. Ospelkaus, L. Humbert, P. Ernst, K. Sengstock, and K. Bongs. Ultracold heteronuclear molecules in a 3D optical lattice. Phys. Rev. Lett., 97:120402, 2006.

[72] J. G. Danzl, M. J. Mark, E. H., M. Gustavsson, R. Hart, A. Liem, H. Zellmer, and H. Ngerl. Deeply bound ultracold molecules in an optical lattice. New J. Phys., 11:055036, 2009.

[73] C. Chin, R. Grimm, P. Julienne, and E. Tiesinga. Feshbach resonances in ultracold gases. Rev. Mod. Phys., 82:1225, 2010.

[74] F. Deuretzbacher, K. Plassmeier, D. Pfannkuche, F. Werner, C. Ospelkaus, S. Ospelkaus, K. Sengstock, and K. Bongs. Heteronuclear molecules in an optical lattice: Theory and experiment. Phys. Rev. A, 77:032726, 2008.

[75] J. J. Zirbel, K.-K. Ni, S. Ospelkaus, T. L. Nicholson, M. L. Olsen, P. S. Julienne, C. E. Wieman, J. Ye, and D. S. Jin. Heteronuclear molecules in an optical dipole trap. Phys. Rev. A, 78:013416, 2008.

[76] S. Sugawa, K. Inaba, S. Taie, R. Yamazaki, M. Yamashita, and Y. Takahashi. Interaction and filling-induced quantum phases of dual Mott insulators of bosons and fermions. Nature Phys., 7:642, 2011.

[77] D. Jaksch, V. Venturi, J. I. Cirac, C. J. Williams, and P. Zoller. Creation of a molecular condensate by dynamically melting a mott insulator. Phys. Rev. Lett., 89:040402, 2002.

[78] B. Damski, L. Santos, E. Tiemann, M. Lewenstein, S. Kotochigova, P. Julienne, and P. Zoller. Creation of a dipolar superfluid in optical lattices. Phys. Rev. Lett., 90:110401, 2003.

[79] J. K. Freericks, M. M. Maśka, A. Hu, T. M. Hanna, C. J. Williams, P. S. Julienne, and R. Lemański. Improving the efficiency of ultracold dipolar molecule formation by first loading onto an optical lattice. Phys. Rev. A, 81:011605, 2010.

[80] Kaden R. A. Hazzard, Alexey V. Gorshkov, and Ana Maria Rey. Spectroscopy of dipolar fermions in layered two-dimensional and three-dimensional lattices. Phys. Rev. A, 84:033608, 2011.

[81] J. Levinsen, N. R. Cooper, and G. V. Shlyapnikov. Topological $px + ipy$ superfluid phase of fermionic polar molecules. Phys. Rev. A, 84:013603, 2011.

[82] J. Ye, H. J. Kimble, and H. Katori. Quantum state engineering and precision metrology using state-insensitive light traps. Science, 320:1734, 2008.

[83] S. Kotochigova and D. DeMille. Electric-field-dependent dynamic polarizability and state-insensitive conditions for optical trapping of diatomic polar molecules. Phys. Rev. A, 82:063421, 2010.

[84] T. Zelevinsky, S. Kotochigova, and Jun Ye. Precision test of mass-ratio variations with lattice-confined ultracold molecules. Phys. Rev. Lett., 100:043201, 2008.

[85] Dmitry Budker, Derek F. Kimball, and David P. DeMille. Atomic Physics: An Exploration through Problems and Solutions. Oxford University Press, Oxford, 2nd edition, 2008.

[86] Bretislav Friedrich and Dudley Herschbach. Alignment and trapping of molecules in intense laser fields. Phys. Rev. Lett., 74:4623, 1995.

[87] Tamar Seideman. Rotational excitation and molecular alignment in intense laser fields. J. Chem. Phys., 103:7887, 1995.

[88] Hirofumi Sakai, C. P. Safvan, Jakob Juul Larsen, Karen Marie Hilligsoe, Kasper Hald, and Henrik Stapelfeldt. Controlling the alignment of neutral molecules by a strong laser field. J. Chem. Phys., 110:10235, 1999.

[89] J. Aldegunde, Hong Ran, and Jeremy M. Hutson. Manipulating ultracold polar molecules with microwave radiation: The influence of hyperfine structure. Phys. Rev. A, 80:043410, 2009.

[90] K. D. Bonin and V. V. Kresin. Electric-Dipole Polarizabilities of Atoms, Molecules, and Clusters. World Scientific, Singapore, 1997.

[91] M. S. Safronova, Carl J. Williams, and Charles W. Clark. Relativistic many-body calculations of electric-dipole matrix elements, lifetimes, and polarizabilities in rubidium. Phys. Rev. A, 69:022509, 2004.

[92] Chen-Lung Hung, Xibo Zhang, Nathan Gemelke, and Cheng Chin. Accelerating evaporative cooling of atoms into Bose-Einstein condensation in optical traps. Phys. Rev. A, 78:011604, 2008.

[93] S. Ospelkaus, C. Ospelkaus, O. Wille, M. Succo, P. Ernst, K. Sengstock, and K. Bongs. Localization of bosonic atoms by fermionic impurities in a three-dimensional optical lattice. Phys. Rev. Lett., 96:180403, 2006.

[94] K. Günter, T. Stöferle, H. Moritz, M. Köhl, and T. Esslinger. Bose-Fermi mixtures in a three-dimensional optical lattice. Phys. Rev. Lett., 96:180402, 2006.

[95] Th. Best, S. Will, U. Schneider, L. Hackermüller, D. van Oosten, I. Bloch, and D.-S. Lühmann. Role of interactions in ^{87}Rb$-^{40}$K Bose-Fermi mixtures in a 3D optical lattice. Phys. Rev. Lett., 102:030408, 2009.

[96] Kevin A. Kuns, Ana Maria Rey, and Alexey V. Gorshkov. *d*-wave superfluidity in optical lattices of ultracold polar molecules. Phys. Rev. A, 84:063639, 2011.

[97] M. A. Baranov, A. Micheli, S. Ronen, and P. Zoller. Bilayer superfluidity of fermionic polar molecules: Many-body effects. Phys. Rev. A, 83:043602, 2011.

[98] M. Lemeshko, R. V. Krems, and H. Weimer. Nonadiabatic preparation of spin crystals with ultracold polar molecules. Phys. Rev. Lett., 109:035301, 2012.

[99] N. T. Zinner, B. Wunsch, D. Pekker, and D.-W. Wang. Bcs-bec crossover in bilayers of cold fermionic polar molecules. Phys. Rev. A, 85:013603, 2012.

[100] A. C. Potter, E. Berg, D. Wang, B. I. Halperin, and E. Demler. Superfluidity and dimerization in a multilayered system of fermionic polar molecules. Phys. Rev. Lett., 105:220406, 2010.

[101] M. Klawunn, J. Duhme, and L. Santos. Bose-Fermi mixtures of self-assembled filaments of fermionic polar molecules. Phys. Rev. A, 81:013604, 2010.

[102] A. Pikovski, M. Klawunn, G. V. Shlyapnikov, and L. Santos. Interlayer superfluidity in bilayer systems of fermionic polar molecules. Phys. Rev. Lett., 105:215302, 2010.

[103] S. G. Bhongale, L. Mathey, S. Tsai, C. W. Clark, and E. Zhao. Bond order solid of two-dimensional dipolar fermions. Phys. Rev. Lett., 108:145301, 2012.